

# **Investigation of optically grey electron cyclotron harmonics in Wendelstein 7-X**

vorgelegt von  
M.Sc.  
Neha Chaudhary  
ORCID:0000-0001-5075-2487

an der Fakultät II - Mathematik und Naturwissenschaften  
der Technischen Universität Berlin  
zur Erlangung des akademischen Grades

Doktor der Naturwissenschaften  
-Dr. rer. nat.-

genehmigte Dissertation

Promotionsausschuss:

Vorsitzender: Prof. Dr. Holger Stark

Gutachter: Prof. Dr. Dieter Breitschwerdt

Gutachter: Prof. Dr. Robert Wolf

Gutachter: Prof. Dr. Hans-Jürgen Hartfuß

Gutachter: Prof. Dr. Wolf-Christian Müller

Tag der wissenschaftlichen Aussprache: 11. Oktober 2021

Berlin 2021



# Abstract

In Wendelstein 7-X (W7-X), the electron cyclotron emission (ECE) from the optically thick second harmonic extraordinary mode (X2-mode) at 140 GHz is used for the continuous electron temperature,  $T_e$ , measurement. This X2-mode emission is shielded by cutoff for the plasma densities above  $1.2 \times 10^{20} \text{ m}^{-3}$  and thus, it cannot be used to provide  $T_e$  for higher plasma densities. These higher densities have been demonstrated at W7-X with neutral-beam injection (NBI) heating and second harmonic ordinary mode (O2-mode) electron cyclotron resonance heating (ECRH). The absorption of radiation from O2-mode ECRH is directly proportional to  $T_e^2$ . Therefore, continuous measurement of  $T_e$  is essential to keep track of incident power absorption and a possible loss of heating efficiency. In this work, the third harmonic extraordinary mode (X3-mode) is investigated for this continuous measurement of  $T_e$ . This is facilitated by the fact that W7-X has a high aspect ratio which leads to a flat magnetic field gradient. This flat gradient results in spectrally well-separated X2-mode and X3-mode emission along the selected line of sight, and that makes the interpretation of harmonics easier. A Martin-Puplett Interferometer was used to probe the broadband ECE harmonics. The strong stray radiation from the non-absorbed ECRH power dominates the broadband measurement and is difficult to suppress as it lies in the middle of the X2-mode. A multi-mode stray radiation notch filter based on multiple dielectric disk structures was designed and constructed to get unpolluted ECE spectra. The experimental measurements show that the radiation temperature of X3-mode emission approaches  $T_e$  for higher plasma densities and sufficiently high  $T_e$ . Under most conditions, the X3-mode emission is optically grey in contrast to the X2-mode emission. The extraction of the  $T_e$  from the X3-mode is less straightforward. Hence, a Bayesian data analysis approach is adopted. A forward modeling of the Martin-Puplett interferometer has been implemen-

---

ted, which predicts the X3-mode emission from the radiation transport calculations. These predictions are used for the Bayesian inference of the  $T_e$  profile from the X3-mode emission. These results show that within specific limits on the plasma parameter regime, the X3-mode measurements are sufficient to provide the  $T_e$  profile for plasma densities above the X2-mode cutoff. For a direct diagnostic application, a correction factor for the radiation temperature of optically grey X3-mode emission is also provided to estimate the central  $T_e$  values for the plasma control purposes.

# Zusammenfassung

In Wendelstein 7-X wird zur Bestimmung der Elektronentemperatur die optisch dichte zweite Harmonische der Elektronen Zyklotron Emission (ECE) X2 verwendet, die für das Magnetfeld von 2.5 T bei Frequenzen um 140 GHz liegt. Da diese Emission aber bei Elektronendichten oberhalb  $1,2 \times 10^{20} \text{ m}^{-3}$  durch den cut-off abgeschirmt wird, steht diese standard ECE Diagnostik bei höheren Dichten nicht mehr zur Bestimmung der Elektronentemperatur zur Verfügung. Eine Heizung solcher Hoch-Dichte Plasmen im Langpuls Betrieb mit den 140 GHz Gyrotrons der Elektronen Zyklotron Resonanz Heizung (ECRH) gelingt durch sukzessives Umschalten der Polarisation der Gyrotrons von senkrecht auf parallel zum Magnetfeld, X2 auf O2 wodurch der X-mode cut-off vermieden wird. In dieser O2 Polarisation ist die benötigte Absorption der Mikrowellen proportional zum Quadrat der Elektronentemperatur und eine kontinuierliche Messung der Elektronentemperatur daher essentiell um die Absorption der einfallenden Heizstrahlen zu mit zu verfolgen um einen eventuelle Verlust der Heizeffizienz rechtzeitig zu erkennen. In diese Arbeit wird daher die dritte Harmonische der ECE X3 als Option für eine kontinuierlichen Messung der Elektronentemperatur in Hoch-Dichte Plasmen untersucht. Dies wird in W7-X dadurch erleichtert, daß das relativ große Aspektverhältnis zu vergleichsweise flachen Gradienten des Magnetfeldes entlang der Sichtlinie der ECE führt und damit zu spektral gut separierten Frequenzbanden der X2 und X3 Emissionen. Um die Harmonischen der ECE breitbandig zu untersuchen wurde ein Martin Puplett Interferometer verwendet. Die Streustrahlung nicht-absorbierter ECRH Leistung behindert hier die Breitbandige Messung und liegt spektral in der Mitte der X2 ECE des Plasmas. Um ungestörte ECE Spektren zu erhalten, wurde daher ein Multi-mode Notch Filter auf Basis eines Stapels dielektrischen Scheiben als Streustrahlungs Filter konstruiert. Die X3 Emission ist im Gegensatz zur X2 Emission

---

bei den meisten Plasmabedingungen optisch grau. Die Ableitung einer Elektronentemperatur aus der gemessenen Strahlungstemperatur der X3 Spektren ist damit weniger direkt und es wurde als Ansatz für diese Arbeit eine Bayessche Analyse gewählt. Dabei wurde mit einer Vorwärts Modellierung der Diagnostik das gemessene Spektrum der X3 Emission mit der dahinter stehenden Information über das Elektronen Temperatur Profils quantitativ verglichen. Die Bayessche Herleitung des Elektronen Temperatur Profils aus den Vorwärtsrechnungen zeigte, daß innerhalb definierter Grenzen des Plasma Parameter Regimes die X3-Messungen ausreichen um Elektronen Temperaturprofile bei Dichten oberhalb des X2 cut-offs zu bestimmen. Zur direkten experimentellen Anwendung auch in Fällen wo die X3 Emission optisch nur grau ist, wurde darüber hinaus ein Skalierungsfaktor bestimmt, mit dem die gemessene Strahlungstemperatur der tatsächlichen Elektronentemperatur angepaßt werden kann.

# Contents

<b>Abstract</b>	<b>iii</b>
<b>Zusammenfassung</b>	<b>v</b>
<b>1 Introduction</b>	<b>1</b>
<b>2 Electron cyclotron emission</b>	<b>13</b>
<b>3 Radiation transport studies</b>	<b>17</b>
3.1 Electron cyclotron emission spectra . . . . .	18
3.2 X3-mode emission . . . . .	21
3.2.1 Flat plasma profiles . . . . .	22
3.2.2 Profile shape dependence . . . . .	24
3.2.3 Plasma parameter scan . . . . .	28
<b>4 Fourier transform spectroscopy</b>	<b>31</b>
4.1 Diagnostic description . . . . .	31
4.1.1 Line of sight . . . . .	33
4.1.2 Mode separation . . . . .	34
4.1.3 Notch filter . . . . .	35
4.1.4 Martin-Puplett interferometer . . . . .	39
4.1.5 Spectral and temporal resolution . . . . .	41
4.2 Calibration . . . . .	42
4.2.1 Interferograms . . . . .	44
4.2.2 Difference spectra . . . . .	45

4.2.3	Calibration factors . . . . .	47
<b>5</b>	<b>Experimental results</b>	<b>49</b>
5.1	Broadband X-mode . . . . .	50
5.2	X2-mode emission . . . . .	53
5.3	X3-mode emission . . . . .	54
<b>6</b>	<b>Bayesian data analysis</b>	<b>57</b>
6.1	Principles of Bayesian data analysis . . . . .	58
6.2	Tools for forward modeling . . . . .	61
6.2.1	Bayesian Minerva modeling framework . . . . .	61
6.2.2	Diagnostic data-source . . . . .	62
6.2.3	Prior for free parameters . . . . .	62
6.3	Forward model . . . . .	66
6.3.1	Model with parametric prior . . . . .	66
6.3.2	Model with non-parametric prior . . . . .	68
<b>7</b>	<b>Bayesian inference results</b>	<b>71</b>
7.1	Prediction of electron cyclotron emission . . . . .	72
7.2	Electron temperature inference . . . . .	74
7.3	Plasma density inference . . . . .	76
7.4	Optical depth and origin of emission . . . . .	77
7.5	Optimized X3 emission frequencies for inference . . . . .	81
<b>8</b>	<b>Conclusions</b>	<b>83</b>
	<b>Acknowledgments</b>	<b>89</b>
	<b>Statutory declaration</b>	<b>91</b>
	<b>List of Figures</b>	<b>91</b>
	<b>Publications as first author</b>	<b>95</b>
	<b>Publications as coauthor</b>	<b>97</b>

*Contents*

---

**Acronyms** **99**

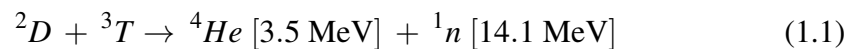
**Bibliography** **100**



# Chapter 1

## Introduction

Fusion research aims at developing the basic principles for constructing a power plant based on the fusion of light nuclei. There are different approaches towards fusion, but this work focuses on thermonuclear fusion using magnetic confinement. Nuclear fusion is the process in which two atomic nuclei fuse to create one or more atomic nuclei, and energy is released during this process. It is the process that provides the fuel for burning stars. For example, the Sun generates its power from the fusion of hydrogen nuclei into helium, using the proton-proton chain reaction. The fusion power density depends on the densities of the reactants, the energy released per reaction, and the rate coefficient. The proton-proton chain reaction has a very low rate coefficient. Hence, the enormous power released in the Sun is due to its size and not because of its fusion reaction rate. Therefore, hydrogen fusion is not used on the Earth. However, the Deuterium-Tritium (D-T) fusion has high reaction rate coefficients, and it is easier to realize for the controlled fusion on Earth.



D-T fusion results in the creation of an alpha particle and a neutron with a total energy release of 17.59 MeV (see eq. 1.1). The reaction rate of D-T fusion is approximately 25 orders of magnitude larger than the fusion reaction rate in the Sun. The fuel for fusion reactor based on D-T fusion is deuterium from water and tritium. Tritium has a short half-life of 12.3 years, and hence, lithium from the Earth's crust is used to generate tritium. At high temperatures, the hydrogen isotopes, deuterium,

and tritium are in a fully ionized state. They must be confined without contacting the confining device for a long time so that fusion reactions can occur at a sufficient rate. The essential condition for the ignition of a fusion reactor is to fulfill the power balance. Power can be lost due to various plasma processes such as diffusion, convection, or radiative losses. These processes are characterized by the energy confinement time,  $\tau_E$ , which is a measure of the thermal energy insulation [1]. Controlled thermonuclear fusion is achieved by increasing the reactant particle's temperature, which increases the particle's kinetic energy and leads to crossing the Coulomb repulsion barrier. This is achieved at temperatures higher than required from Lawson's criterion quantified by the triple product. Lawson's criterion is derived from the comparison of the power generated from a fusion reaction and the power lost from the confined plasma [2]. The triple product is used in nuclear fusion research as a figure of merit, and it is the product of plasma density  $n$ ,  $\tau_E$ , and plasma temperature,  $T$ . Fusion energy gain factor,  $Q$ , is the ratio of fusion power generated in a reactor to the power required to maintain the plasma in a steady state [3]. For example, to have a minimum  $Q$  value for net energy production from the D-T fusion, the triple product is given by eq. 1.2 at  $T = 14$  keV using the reaction rate and its temperature dependence [4].

$$nT\tau_E \geq 3 \times 10^{21} \text{ keV s/m}^3 \quad (1.2)$$

$\tau_E$  depends on many parameters such as the geometry of the confinement device, the plasma density, the toroidal magnetic field, and the heating power. For a varying parameter space, the empirical scaling laws for  $\tau_E$  have been established from the experimental results of many plasma confinement devices [5]. These scaling laws can be extrapolated to arrive at reactor-like conditions.

The plasma confinement using a vacuum chamber enclosed by a magnetic configuration with a torus shape is the most promising concept for realizing fusion energy. The Lorentz force acts on the charged particles of the plasma in the presence of a magnetic field. It forces particles to gyrate around the magnetic field lines and binding them to the magnetic field lines. However, the particle drifts are present because of the gradient and curvature of the magnetic field lines [6]. The typical toroidal magnetic field in a confinement device is of the order of a few Tesla. This leads

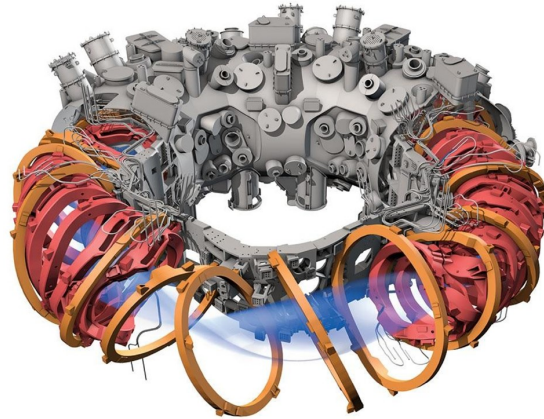


Figure 1.1: Wendelstein 7-X stellarator

to the gyro-radii of a few millimeters for the ions and a tenth of a millimeter for the electrons in the plasma at a temperature of few keV. The two toroidal magnetic confinement device designs are stellarator [7], and tokamak [8]. A tokamak has the toroidal field from coils and the poloidal field generated by a strong current induced in the plasma. The primary coils of a tokamak are in a transformer-like arrangement and in which the plasma acts as the secondary winding. These fields result in twisted magnetic field lines creating the nested magnetic surfaces for the plasma confinement. A stellarator uses external currents to generate a magnetic field that confines the plasma [9]. Hence, plasma currents are not required for confinement. However, the pressure-driven plasma currents remain present in a stellarator.

Wendelstein 7-X (W7-X) [10–15] is a superconducting stellarator with a major radius of 5.5 m and a minor radius of 0.5 m, corresponding to a plasma volume of  $30 \text{ m}^3$  (see figure 1.1). It has low magnetic shear, a rotational transform near 1 and an optimized magnetic field. It is planned to achieve 30 min of plasma operation at 10 MW of heating power after the implementation of actively cooled in-vessel components. A magnetic field of 2.5 T is generated in the center of plasma axis. Steady state electron cyclotron resonance heating (ECRH) is used for generating and heating the plasma [16, 17]. Moreover, the neutral-beam injection (NBI) is used for heating the plasma as well as to investigate the fast ion physics [18, 19]. The fast ions act as a proxy for fusion alpha particles. This permits the investigation of their plasma vessel wall loads and slowing-down time, which is the heating in a burning

fusion plasma.

Plasma parameters such as density and temperature must be known simultaneously to understand and operate plasmas in a magnetic confinement device. It is achieved by using a large set of plasma diagnostics [20, 21]. Many of these diagnostics are based on analyzing the waves or particles emitted by plasma, or by passing externally generated waves or particles through plasma, and subsequently analyzing the plasma-particle or plasma-wave interaction. This work focuses on the microwave diagnostic using electron cyclotron emission (ECE) from the plasma [22]. It is a passive diagnostic and hence does not interfere with the plasma at all. In the presence of an applied magnetic field, Lorentz force acts on the electrons in the plasma, and these electrons gyrate around the magnetic field lines. Hence, the magnetically confined plasma emits and absorbs electromagnetic radiation at the gyration frequency,  $\omega_c$ , of the electrons, which is known as ECE.

$$\omega_c = \frac{eB_0}{m_{e0}} \quad (1.3)$$

The gyration frequency is given by eq. 1.3, where,  $e$ , is the elementary charge, and  $m_{e0}$ , is the rest mass of electron. The gyration frequency is directly proportional to the applied magnetic field,  $B_0$ . ECE can be characterized by differently polarized modes, depending on the observation direction with respect to the magnetic field. For parallel observation, the emission is right-hand circularly polarized.

For perpendicular observation, ECE has two linearly polarized modes. These are characterized as follows: the ordinary mode (O-mode), which has an electric field parallel to the magnetic field, and the extraordinary mode (X-mode), which has an electric field perpendicular to the magnetic field. The presence of periodic time retardation introduces the harmonic generation for the emission from a single gyrating electron. For perpendicular observation, the ECE has different harmonics of X-mode and O-mode.

$$\omega_m = m\omega_c, \text{ for } m = 1, 2, 3, \dots \quad (1.4)$$

The gyration frequency of  $m^{th}$  harmonic is given by equation 1.4. Each harmonic frequency will be Doppler shifted except for perpendicular observation. Hence at

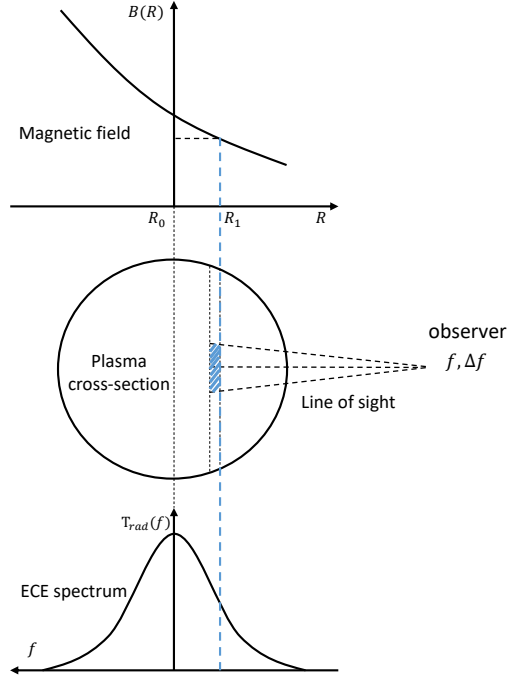


Figure 1.2: Schematic showing the increasing magnetic field,  $B(R)$ , in a direction away from the observer along the plasma radius,  $R$ , for a circular plasma cross-section. A magnetic field is mapped (in blue color) to plasma radius and the corresponding radiation temperature of ECE. A monotonically varying magnetic field results in frequencies of ECE which can be mapped to different plasma radii, and the ECE spectrum has underlying spatial  $T_e$  profile information.

W7-X, the line of sight is chosen to be approximately perpendicular to the magnetic field to minimize this Doppler shift. As the electrons are gyrating, the relativistic mass increase has to be taken into account for plasma at fusion relevant temperatures.

$$\omega_{cr} = \omega_c \sqrt{1 - \frac{v_e^2}{c^2}} \quad (1.5)$$

The gyration frequency,  $\omega_{cr}$ , including the relativistic mass increase is given by equation 1.5, where,  $v_e$ , is the velocity of electrons and,  $c$ , is the speed of light. As the electrons are always gyrating, there will be no emission at  $\omega_c$ , and this is known as the cold resonance frequency. Instead, it is relativistically downshifted to  $\omega_{cr}$ . This downshift in the emission line depends on the kinetic energies of the electrons

in plasma and hence, on the electron velocity distribution. Consequently, measuring the intensity or radiation temperature of ECE provides information about the electron velocity distribution function. A magnetic field surface can be associated with a spatial location in plasma or the plasma radius,  $R$ .

$$\omega_{cr} = \frac{eB(R)}{m_{e0}} \sqrt{1 - \frac{v_e^2}{c^2}} \quad (1.6)$$

For the particular case, the magnetic field is increasing away from the observer along the line of sight (see figure 1.2). Each magnetic field surface is associated with gyration frequency of electron (see equation 1.6). The low field side (LFS) has the lower magnetic field values in W7-X, which corresponds to the lower gyration frequencies and the high field side (HFS) has the higher magnetic field values leading to higher gyration frequencies. Thus, the gyration frequency of electrons is mapped to a spatial location in the plasma. The ECE diagnostic is used to provide the radiation temperature of the emission. This radiation temperature spectrum,  $T_{rad}(f)$ , of ECE combined with the spatial location of origin of the ECE provides the information on the electron temperature profile,  $T_e(\rho)$ , in the plasma. Here,  $f$  is the frequency of the ECE, and  $\rho$  is the normalized plasma radius.

Optical depth or thickness is the parameter used for quantifying the absorption and emission in the plasma. The knowledge of optical depth is essential to characterize the ECE with respect to the capabilities as a local electron temperature measurement [21, 23].

For highly absorbing or optically thick plasma, for a frequency of ECE, the radiation transport happens from all the optically thick plasma layers to the finally emitting layer, which is known as the emission layer. This emitting layer is behind the cold resonance position, and the width of this emission layer in optically thick plasma is narrow, which means that emission at this frequency is spatially localized in plasma. This localized ECE from optically thick plasma behaves nearly like a black-body emission. For this case, the radiation temperature of ECE can be directly taken as the black-body electron temperature of the narrow emission layer, which is spatially localized in plasma. Hence, the information on local electron temperature in the plasma can be accessed from ECE.

For fusion-relevant plasma parameters, the ECE from first harmonic ordinary mode

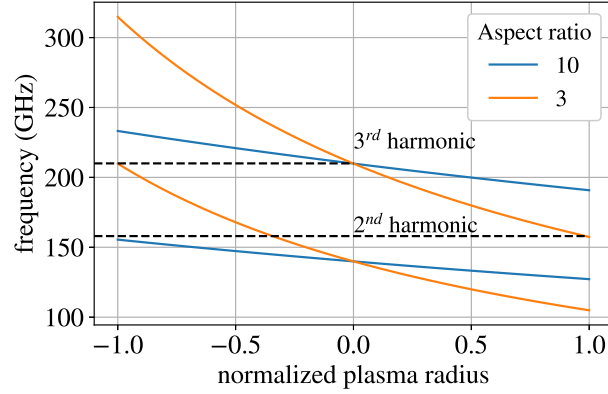


Figure 1.3: The 2<sup>nd</sup> and 3<sup>rd</sup> harmonic emission frequencies are shown along the plasma radius for two aspect ratios 3 and 10 of the magnetic confinement device.

(O1-mode), and second harmonic extraordinary mode (X2-mode) have high re-absorption in plasma, which results in a high optical depth [22, 24]. Generally, these modes are used for the diagnostic purposes of  $T_e$  profile at magnetic confinement devices. A heterodyne radiometer [25–29] is used at W7-X to measure the optically thick X2-mode emission, for providing the  $T_e$  profile information.

For transparent plasma, which is optically thin (or grey), for a frequency of ECE, the radiation transport from all the optically thin plasma layers results in a wider emission layer in the plasma, which means that emission is not spatially localized in plasma. The higher ECE harmonics ( $m = 3, 4, \dots$ ) are generally optically grey. To provide any kind of local  $T_e$  information from these optically grey harmonics, the precise knowledge on the spatial origin of ECE in plasma has to be known, and this requires the understanding of radiation transport in the plasma. The theoretical details of the radiation transport of ECE are provided in the chapter 2.

TRAcing VISualized (TRAVIS) [30] is a ray-tracing and radiation transport code which calculates the beam propagation towards the ECE receiver optics in W7-X. The radiation transport calculations, from TRAVIS, can determine the radiation temperature and optical depth of ECE. These calculations are done for the optically grey third harmonic extraordinary mode (X3-mode) including W7-X geometry, and are discussed in details in the chapter 3.

The motivation for investigating the ECE harmonics are listed below. W7-X has a high aspect ratio of  $\approx 10$  which results in a moderate magnetic field gradient

along the ECE line of sight [31]. Magnetic confinement devices with a low aspect ratio, for example, the Joint European Torus (JET) tokamak has a steep magnetic field gradient toward the inboard side of the device [32]. The ECE frequency (see eq. (1.3)) is directly proportional to the magnetic field. The 2<sup>nd</sup> and 3<sup>rd</sup> harmonic frequencies are shown in figure 1.3 for two aspect ratios, 3 and 10, of a magnetic confinement device. It can be seen that the high aspect ratio results in the spectrally well-resolved ECE harmonics, and the low aspect ratio results in the overlapping of the ECE harmonics, which complicates the interpretation of the spectrum for these devices. Hence, the geometry of W7-X stellarator facilitates the study of the ECE harmonics.

For stellarators, the triple product with  $\tau_E$  from ISS04 scaling depends linearly on plasma density,  $n_e$  [33, 34]. Hence, high  $n_e$  is required to improve the plasma confinement by increasing the triple product. ECE is also a power loss mechanism for a fusion reactor, for International Thermonuclear Experimental Reactor (ITER) at  $T_e > 30$  keV and moderate densities, the estimated ECE power loss is a significant fraction of heating power [35]. Hence, high  $n_e$  is required to achieve high pressures at reduced  $T_e$  to avoid power losses. Moreover, high  $n_e$  allows easier access to divertor detachment [36, 37]. In a burning fusion plasma, high  $n_e$  is advantageous, as it keeps the fast ion population at a low level by reducing the fast ion slowing-down time [38]. Tokamaks have a limit on increasing  $n_e$  because of the presence of plasma current, which is known as Greenwald density limit [39]. The density increase beyond the Greenwald limit typically leads to plasma disruptions terminating the plasma confinement [40]. This is not the case for stellarators because of the absence of toroidal currents [41]. Therefore, it is easier to achieve these high plasma densities in a stellarator compared to a tokamak. Specially, for W7-X, the neoclassical transport optimization favors high  $n_e$ . However, there is an upper  $n_e$  limit present in stellarators because of the radiation limit set by impurities [5]. To summarize, stellarators can use the high-density parameter space for improved plasma confinement.

The plasma frequency,  $\omega_p = (n_e e^2 / m_e \epsilon_0)^{1/2}$ , increases with plasma density,  $n_e$  and the group velocity is decreasing with increased plasma density until there is no more wave propagation, and this phenomenon is known as cutoff. The plasma density above which there is no propagation of an electromagnetic wave with a

cutoff frequency  $\omega_{p_{cutoff}}$  is known as cutoff density,  $n_{e_{cutoff}}$ . Hence, no ECE radiation leaves the plasma if the plasma density along the line of sight exceeds a value where the cutoff conditions are reached. For a magnetic field of 2.5 T at the plasma center in W7-X, the X2-mode has a cutoff at  $n_{e_{cutoff}} \approx 1.2 \times 10^{20} \text{ m}^{-3}$ . Hence, this radiometer ECE diagnostic, measuring the optically thick X2-mode for  $T_e$  information, cannot be used for plasma densities above  $n_{e_{cutoff}}$ . This is another motivation to investigate the X3-mode of ECE, with respect to  $T_e$  measurement for higher densities beyond X2 emission cutoff.

The plasma is heated with the X2-mode of electron cyclotron resonance at 140 GHz using gyrotrons at W7-X. At plasma densities above  $n_{e_{cutoff}}$ , this X2-mode ECRH cannot be used to heat the plasma, as there is no wave mode propagation. For reactor-relevant conditions, W7-X must operate at a  $n_e$  above  $n_{e_{cutoff}}$ . Other heating mechanisms are required to achieve these high densities beyond  $n_{e_{cutoff}}$ . The second harmonic ordinary mode (O2-mode) of electron cyclotron resonance has a cutoff at  $n_{e_{cutoff}} \approx 2.4 \times 10^{20} \text{ m}^{-3}$ . Hence, it is used to achieve these high-density regimes beyond the X2-mode cutoff. The O2-ECRH is specific to the magnetic field available in W7-X stellarator [42], and this O2 heating has a relatively poor single pass power absorption in the plasma compared to X2-ECRH. Thus, the O2 heating is achieved at W7-X with multiple plasma passes of gyrotron beams to have sufficient absorption of power in the plasma. Plasmas with high  $n_e$  fully sustained with O2 heating have been already demonstrated at W7-X with less than 5% non-absorbed power. However,  $n_e$  is further limited as O2 heating only works until the beam refraction inhibits meeting the mirror tiles on the back wall of the plasma vessel. Moreover, the O2 heating is only successful up to  $n_e \approx 1.8 \times 10^{20} \text{ m}^{-3}$  due to the decreased absorption for higher densities. Ordinary-eXtraordinary-Bernstein (O-X-B) mode or X3-mode heating can be used to further increase  $n_e$  but this is not yet demonstrated at W7-X [43, 44]. As the absorption of O2 heating depends on  $T_e^2$ , it must be controlled to avoid the collapse of plasma despite high densities. For the O2 heated plasma with high  $n_e$ , a  $T_e$  measurement is essential to control the plasma operation. Hence, it is a motivation for this work, and the X3-mode of ECE is investigated for the applicability towards the  $T_e$  measurement in high  $n_e$  plasmas exceeding X2-mode cutoff.

W7-X is also planned to operate at a lower magnetic field of 1.7 T to study  $\beta$ -limits

[44, 45]. For these plasma operations, the X3-mode ECE would become necessary to measure  $T_e$  instead of X2-mode. Hence, the lower magnetic field operations of W7-X also benefit from the exploration of the X3-mode.

At W7-X, a Martin-Puplett interferometer as the Fourier transform spectrometer (FTS) was used to study broadband ECE in the spectral range of 100-300 GHz [46–48]. This interferometer instrument was used at the Axially Symmetric Divertor Experiment (ASDEX) Upgrade tokamak [49, 50] and it is refurbished for the use at W7-X. Because of the strong impact of stray radiation and the overlapped harmonics due to a higher magnetic field gradient, the operation at ASDEX upgrade was limited. The FTS as an ECE diagnostic have been previously used at other magnetic confinement devices [32, 51–54] to measure  $T_e$  and it will also be used at ITER [55, 56]. With this diagnostic, the higher harmonics of ECE are investigated towards their diagnostic potential for  $T_e$  measurement in high-density plasmas. Both X-mode and O-mode are accessible, and hence different parts of the phase space of the electron's motion in plasma can be studied.

Plasmas were heated by ECRH at a frequency of 140 GHz with a maximum input power of 7 MW or with NBI with a maximum input power of 3.5 MW. ECE measurements from the FTS, and the radiometer are affected by the stray radiation from non-absorbed ECRH power which lies in the middle of the spectral range of 2<sup>nd</sup> harmonic at 140 GHz [57]. It is necessary to filter this stray radiation frequency for a clean measurement of the broadband ECE spectral features. Commercial notch filters are generally based on waveguide technologies and are only available for one or a few waveguide modes. The transmission ranges of these commercial filters are generally the moderate frequency bands around the notch. Hence, for this specific application, a multi-mode notch filter [58] based on a multiple dielectric disk structure was designed. The development of this notch filter is described in chapter 4.

An Indium antimonide (InSb) bolometer type detector, cooled to liquid helium temperatures, was used to measure the interferograms. The FTS was calibrated with a black-body source through the hot-cold calibration technique in the spectral range of 100-300 GHz. The fast Fourier transform (FFT) of the interferogram provides the radiation temperature spectrum,  $T_{rad}(f)$ . Experimental characterization and calibration details are discussed in the chapter 4. The calibrated radiation temperature spectra of ECE from different plasma experiments are shown in the chapter 5.

The classical analysis techniques of ECE using direct inversion from the measured  $T_{rad}(f)$  to a  $T_e(\rho)$  profile is challenging. Because this inversion depends on the precise knowledge of magnetic field equilibrium, beam refraction, and the finite optical depth, which itself implicitly depends on  $T_e$  and  $n_e$ . Consequently, a Bayesian data analysis using forward modeling of the diagnostic is the method of choice to interpret the experimentally measured  $T_{rad}(f)$ . Forward modeling of the ECE diagnostic have been done before at different magnetic confinement devices [59–62]. For this work, the forward modeling of the diagnostic is done using the Bayesian Minerva modeling framework [63]. This framework uses graphical models consisting of different probability nodes [64, 65].

The workflow of the Bayesian data analysis using forward modeling of measurements is elaborated with an example of inference of  $T_e(\rho)$  profile using the experimental observation of  $T_{rad}(f)$ . The forward model usually has some input parameters, which for this example is the  $T_e(\rho)$  profile, where  $\rho$  is the normalized plasma radius. The prediction of the forward model is  $T_{rad}(f)$  from radiation transport calculations done with TRAVIS. The observation of the forward model is the experimentally measured  $T_{rad}(f)$  with FTS. Forward calculations are done with varying input parameters until the prediction matches the observation within model uncertainties.

In Bayesian data analysis, this variation of the input parameter is not done manually or randomly. Instead, a distribution function based on some *prior* knowledge of the input parameter is allocated. The starting point of forward calculation is an initial guess from this distribution. From Bayes theorem [66], the conditional probability of a specific value of  $T_e(\rho)$ , given that observation of  $T_{rad}(f)$  is true, is known as *posterior* probability. Bayesian data analysis for this work is to determine this *posterior* probability. The next iteration of forward calculation is a step towards finding the input parameter for which the *posterior* probability is maximum, known as maximum a *posteriori* probability (MAP) [67]. The iterations of forwards calculations are done until it reaches MAP. This MAP result corresponds to input parameter ( $T_e$ ) value for which the model prediction ( $T_{rad}(f)$  from TRAVIS) agrees with the model observation ( $T_{rad}(f)$  from experiments) within the model uncertainties. This value of  $T_e$  is the inference from the Bayesian data analysis of the experimental observation of  $T_{rad}(f)$ .

The forward calculations are required with a wider sample space from the *prior* distribution of input parameter to have better knowledge on *posterior* distribution. The sampling of the *posterior* distribution is done with Markov chain Monte Carlo (MCMC) simulations [68]. The standard deviation of the  $T_e$  for different samples from MCMC simulations is the uncertainty on the inferred  $T_e$ . This forward modeling using Bayesian principles is outlined in detail in the chapter 6.

For this work, besides the  $T_e(\rho)$  profile, there are additional input parameters in the forward model such as the  $n_e(\rho)$  profiles, the X-mode contribution in predicted  $T_{rad}$ , the central magnetic field scaling, and the observational variance scaling. The *prior* knowledge on the  $T_e(\rho)$  and  $n_e(\rho)$  profiles are incorporated by a parametric *prior* and by a non-parametric Gaussian process *prior*. The parametric *prior* uses a definition of the profile shape using parameterization. Whereas, Gaussian processes [69] are defined directly over the functions, and they are characterized by a mean and covariance function. Gaussian processes have universal approximation qualities and have the advantage of allowing even non-monotonic profile shapes with multiple peaks, which cannot be produced by the parameterization for this work. Forward predictions of  $T_{rad}(f)$  using TRAVIS are done with these two *priors* of the  $T_e(\rho)$  and  $n_e(\rho)$  profiles.

The prediction corresponding to MAP provides the inferred  $T_e(\rho)$  and  $n_e(\rho)$  profiles, and the other input (or free) parameters of the model. Additionally, the inferred  $T_e$  and  $n_e$  profiles, where the prediction  $T_{rad}(f)$  agrees with observation, were used as an input to radiation transport calculation in TRAVIS to extract the information on the optical depth, the velocities of electrons contributing to emission, and the origin of emission in the plasma. A detailed discussion on the Bayesian inference results is done in the chapter 7.

## Chapter 2

# Electron cyclotron emission

For early fusion experiments, electron cyclotron emission (ECE) was investigated as a power loss mechanism [22]. Eventually, it was discovered that the emission from the lower harmonics, first harmonic ordinary mode (O1-mode) and second harmonic extraordinary mode (X2-mode), is sufficiently reabsorbed in the plasma, and these harmonics are optically thick. Therefore, the emission is used as a diagnostic to provide a local electron temperature,  $T_e$ , measurement in the plasma. ECE diagnostic have the advantage over the other  $T_e$  measurements, that it can measure core  $T_e$  continuously with a high sampling rate. In magnetic confinement devices, this continuous core  $T_e$  measurement is also used for plasma control. The ECE measurement also provides the spatial  $T_e(\rho)$  profile in the plasma. This spatial  $T_e(\rho)$  profile can be further used for various physics studies such as electron heat transport, heat-pulse propagation, and power balance studies. Additionally, a high temporal resolution (typically  $\mu\text{s}$ ) of ECE measurement supports the investigations of temperature fluctuations. These studies mainly include the identification of the magnetohydrodynamic (MHD) activity by analyzing temperature fluctuations. These fluctuations combined with their spatial correlation length give information on the specific MHD modes, including both coherent and turbulent modes. In modern fusion experiments, ECE measurements are used as a standard diagnostic for the purpose of plasma control and to investigate different physics phenomena related to electron transport.

The interpretation of ECE is more straightforward when the different harmonics

are spectrally well separable. The harmonic overlap can originate from two causes, first the magnetic field gradient along the line of sight and second, the emission line broadening. The magnetic field gradient depends on the aspect ratio of the magnetic confinement device. Wendelstein 7-X (W7-X) has a large aspect ratio of 10, and a line of sight is available with a particularly low magnetic field gradient. For the perpendicular observation to the magnetic field, the relativistic line broadening of emission line is dominant (see equation 1.5). This relativistic line width is proportional to the harmonic number and the velocity of the electrons. For fusion plasmas with  $T_e$  above 20 keV, where electrons approach strong relativistic conditions, the line width of different harmonics overlap and ECE spectrum becomes continuous. However, for fusion plasma with  $T_e$  below 10 keV, the line width of different harmonic is separable and ECE spectrum can be measured to provide spatial electron temperature profile. W7-X plasma fall in the latter category with  $T_e$  below 10 keV. This results in spectrally well-separated harmonics in W7-X.

A gyrating electron emits the cyclotron radiation at a frequency  $\omega_c$  (see equation 1.3) and including the relativistic mass increase at  $\omega_{cr}$  (see equation 1.5). The spiral trajectory of gyrating electron has a radius,  $r_L$ , Larmor or gyroradius.

$$r_L = \frac{v_{e\perp}}{\omega_c} = \frac{m_e v_{e\perp}}{eB_0} \quad (2.1)$$

The gyroradius is of the order of tenth of millimeters for the magnetic field and electron temperatures of W7-X plasmas. The perpendicular observation of ECE is the most important for the diagnostic applications. Both extraordinary mode (X-mode) and ordinary mode (O-mode) emission can be used. The power,  $P$ , radiated through ECE from a single electron in a solid angle,  $\Omega$ , for perpendicular observation is given by the following equation [21].

$$\frac{d^2P}{d\Omega d\omega} = \frac{e^2 \omega^2}{8\pi^2 \epsilon_0 c} \sum_{m=1}^{\infty} \left\{ \beta_{\parallel}^2 J_m^2 \left( \beta_{\perp} \frac{\omega}{\omega_{cr}} \right) + \beta_{\perp}^2 J_m^2 \left( \beta_{\perp} \frac{\omega}{\omega_{cr}} \right) \right\} \delta[\omega - m\omega_{cr}] \quad (2.2)$$

Where,  $\omega$  is the emission frequency,  $\epsilon_0$  is the vacuum permittivity,  $c$  is the speed of light,  $\beta = v_e/c$ ,  $v_e$  is the electron velocity,  $\omega_{cr} = \omega_c(\sqrt{1-\beta^2})$ , and,  $m$ , is the harmonic number. The first term in the brackets of equation 2.2 is the contribution from the O-mode emission, coming from the parallel electron velocity to magnetic

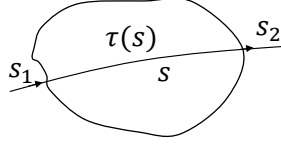


Figure 2.1: A ray entering the plasma volume at position  $s_1$  and leaving at  $s_2$ . The optical depth  $\tau_s$  at any position  $s$  is obtained by integrating absorption from the plasma exit position  $s_2$  to  $s$ .

field,  $\beta_{\parallel}$ . The second term is the contribution from the X-mode coming from the perpendicular electron velocity to the magnetic field,  $\beta_{\perp}$ . Different harmonics with  $\omega_m$  arise from both X-mode and O-mode.

The absorption in the plasma is discussed for an example of a plasma column of constant density and temperature in the presence of a constant magnetic field. The ECE is observed along the path  $s$  through the plasma (see fig. 2.1). In plasma, the medium of emission and absorption are connected, and hence the re-absorption of the emitted radiation by the electrons needs to be taken into account. The intensity of each harmonic of ECE can be determined by solving the radiation transport equation along the path  $s$ . The radiation transport equation for a ray with path element  $ds$  through the absorbing and emitting plasma is given by the following equation.

$$\frac{dI_{\omega}}{ds} - \frac{\partial I_{\omega}}{\partial s} = N^2 \frac{d}{ds} \left( \frac{I_{\omega}}{N^2} \right) = j_{\omega} - \alpha_{\omega} I_{\omega} \quad (2.3)$$

Where,  $I_{\omega}$ , is the intensity of the emission,  $N$  is the refractive index of plasma,  $j_{\omega}$  is the emission coefficient, and  $\alpha_{\omega}$  is the absorption coefficient. The radiation transport happens from position  $s_1$  to  $s_2$  and the intensity of emission at position  $s_2$  is given by the following equation.

$$I_{\omega} = \int_0^{\tau_{21}} B_{\omega}(\tau) e^{-\tau} d\tau \quad (2.4)$$

$B_{\omega} = j_{\omega}/\alpha_{\omega}$  is the source function represented by the ratio of emission and absorption coefficients.  $d\tau = \alpha_{\omega} ds$  is the differential optical depth. The total optical depth

along the path  $s$  is given by the following equation.

$$\tau_{21} = \int_{s_1}^{s_2} \alpha_{\omega} ds \quad (2.5)$$

The absorption has to be known to calculate the emission intensity from equation 2.4.

For optically thick plasma, the source function can be calculated by applying the Kirchhoff's law. From this law, if a medium is in the thermodynamic equilibrium, the ratio of emission and absorption is constant and it is given by the black-body intensity. The physical temperature of the black-body is the electron temperature of plasma. Then, the source function can be given by the Rayleigh Jeans law which depends on the electron temperature.

$$\frac{j_{\omega}}{\alpha_{\omega}} \approx \omega^2 \frac{k_B T_e}{8\pi^3 c^2} \quad (2.6)$$

From the Rayleigh jeans approximation, the radiation temperature for a homogeneous plasma with refractive index,  $N$ , is given by the following equation.

$$T_{rad} = \frac{8\pi^3 c^2 I_{\omega}}{k_B \omega^2 N^2} \quad (2.7)$$

The refractive index of plasma depends on the plasma density. For fusion related parameter, O1-mode and X2-mode of ECE are optically thick representing the black-body emission. For these modes, the  $T_{rad}$  is the  $T_e$  of plasma.

Generally, the third harmonic extraordinary mode (X3-mode) is optically grey and cannot provide  $T_e$  directly from Rayleigh jeans law. The solutions of the radiation transport equation and optical depth equation are needed to provide information on the re-absorption of the emission. For the geometry and plasma parameters of W7-X, these equations are solved using the ray-tracing and radiation transport code TRAcing VISualized (TRAVIS). The detailed simulation results, showing the emission and optical depth of the X3-mode, are presented in the next chapter.

## Chapter 3

# Radiation transport studies

The intensities of the electron cyclotron emission (ECE) harmonics can be determined by solving the radiation transport for the magnetically confined plasma. This requires knowledge of the magnetic field equilibrium, the spatial plasma density profile, the spatial electron temperature profile, and the line of sight of the observer. The typical ECE frequencies are in the range of microwaves for the magnetic field of the confinement device. Microwaves in inhomogeneous plasmas can be described by independent rays with their own trajectories. For the concerned plasma parameter, this ray trajectory can be described by the cold dispersion relation of magnetized plasma taken as a Hamiltonian. For the fusion devices, generally, the ray-tracing codes are used to estimate ECE.

TRAcing VISualized (TRAVIS) is a ray tracing and radiation transport code used to simulate electron cyclotron resonance heating (ECRH) and ECE for the plasma parameters and the 3D geometry of Wendelstein 7-X (W7-X) [30]. In the ECE mode of TRAVIS, the radiation temperature spectrum,  $T_{rad}(f)$ , of ECE is determined by solving the radiative transfer equations [70]. For each ray, the ray-tracing and the optical depth equations are solved. The ray-tracing equations are solved in the weakly relativistic regime with the thermal effects taken into account [71]. The optical depth equations are solved to determine the power absorption and deposition with a fully relativistic approach [21]. The input parameters to initialize TRAVIS simulations can be categorized into two sections: The state of the plasma and the state of ECE diagnostic. The state of plasma is represented by the  $T_e(\rho)$  and

$n_e(\rho)$  profiles as functions of the normalized plasma radius  $\rho$  and the 3D magnetic field equilibrium to map the ECE frequencies to the microwave beam coordinates. The magnetic field equilibrium is provided by the Variational Moments Equilibrium Code (VMEC) [72]. The state of the ECE diagnostic is described by the line of sight into the plasma, the Gaussian optics, the antenna position, wall reflection coefficients, wave polarization modes, spectral and temporal resolution. In addition to the predicted  $T_{rad}(f)$ , TRAVIS provides the following information to characterize the emission for each frequency: the optical depth, the velocities of electrons which contribute to emission, and the location of the spatial origin of the emission in the plasma. The simulations for ECE from TRAVIS are shown in the next sections to discuss different aspects and dependencies of the emission on the plasma parameters.

### 3.1 Electron cyclotron emission spectra

Figure 3.1b shows broadband ECE spectra for both X-mode and O-mode calculated with TRAVIS for the line of sight and geometry of the W7-X. The  $n_e$  profile (see fig. 3.1a) is chosen where core density ( $\approx 5 \times 10^{19} \text{ m}^{-3}$ ) is significantly below the second harmonic extraordinary mode (X2-mode) cutoff. The  $T_e$  profile is chosen where the core temperature ( $\approx 4 \text{ keV}$ ) corresponds to the available ECRH power ( $\approx 3 \text{ MW}$ ) for the chosen  $n_e$  at W7-X. In the calculated X-mode and O-mode spectra, ECE up to 4<sup>th</sup> harmonic can be seen at the cold resonance frequencies of 70, 140, 210, 280 GHz for a central magnetic field of 2.5 T. A clear spectral separation between the harmonics can be seen, which is the result of the high aspect ratio of W7-X corresponding to the low magnetic field gradient along the line of sight, avoiding harmonic overlap. It can be seen that most of the emission is contained in the following harmonics, first harmonic ordinary mode (O1-mode), X2-mode, and third harmonic extraordinary mode (X3-mode). Generally, the O1 and X2 emissions are optically thick and behave as a black-body emissions. This is reflected in the calculated spectra, as the maximum radiation temperatures of the O1 and the X2 emission represent the core  $T_e$  of 4 keV. For the black-body emission over a wider radial range, often a strong spectral feature is observed for low field side (LFS) frequencies. This emission feature originates from the electrons belonging to the

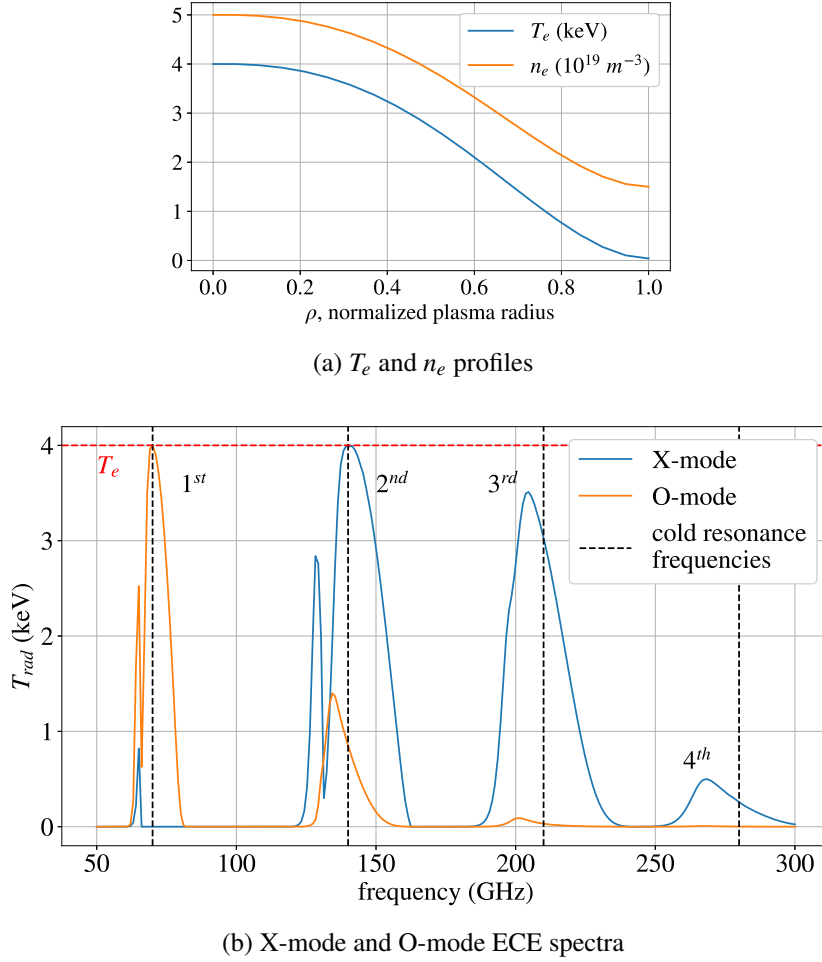


Figure 3.1: (a) The input electron temperature,  $T_e$ , and plasma density,  $n_e$  profiles to the radiation transport code TRAVIS for simulating the ECE. (b) ECE spectra, from radiation transport calculations using TRAVIS, showing both extraordinary mode (X-mode) and ordinary mode (O-mode) emission in a spectral range of 50–300 GHz. At a magnetic field of 2.5 T at the plasma axis, the ECE harmonics for the cold resonance lie at multiples of 70 GHz.

outermost Maxwell–Boltzmann distribution tail of the hot plasma core electrons, from which the emission is so strongly downshifted that it cannot be reabsorbed in the plasma. This downshifted emission for O1-mode (around 60 GHz), and X2-mode (around 125 GHz) can be seen in the spectra. For the desired high-density plasma operation of W7-X, both optically thick O1-mode and X2 mode emission are in the cutoff, and the investigation of higher harmonics is crucial. As seen in

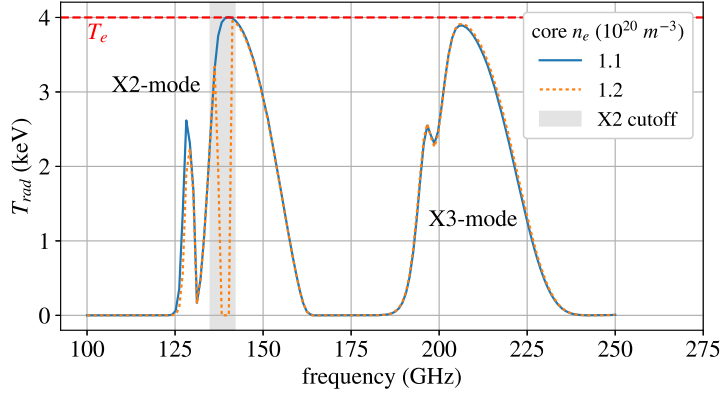


Figure 3.2: ECE spectra showing X2-mode and X3-mode emission for a fixed electron temperature profile (as given in figure 3.1a), the plasma density is varied with the profile shape given in figure 3.1a. For a central magnetic field of 2.5 T, the X2-mode emission goes into cutoff at a plasma density of  $1.2 \times 10^{20} \text{ m}^{-3}$  and cannot be used for diagnostic purposes. The X3 emission does not change with increasing plasma density for these specific values of electron temperature ( $\approx 4 \text{ keV}$ ).

the calculated spectra, the emission from higher O-mode harmonics is relatively weaker compared to the higher harmonics of X-mode. Hence, the focus of the work in the later chapters is on higher harmonics of the X-mode emission, specifically X3-mode emission. For the chosen plasma parameters in fig. 3.1a, the X3 emission is optically grey, as the maximum  $T_{rad}$  is lower than the core  $T_e$ . The emission from optically grey plasma is less localized, and consequentially the emission contains information about both electron temperature and plasma density. This X3 emission is explored in this work as high-density access to plasma  $T_e$  measurement, in case the X2 emission is in the cutoff.

As a motivation for the further investigations of the X3 emission, example spectra are shown in figure 3.2. The X2-mode and X3-mode are calculated for the electron temperature and density profile shapes shown in 3.1a. The core plasma density is varied in two steps while the plasma core electron temperature is kept constant. It can be seen in the spectra that with increase in core  $n_e$  from  $\approx 1.1 \times 10^{20} \text{ m}^{-3}$  to  $\approx 1.2 \times 10^{20} \text{ m}^{-3}$ , the X2 emission at central frequencies (around 140 GHz) went into cutoff (zero radiation temperature). However, the X3 emission did not change for the increased  $n_e$ , and  $T_{rad}$  is nearly equal to  $T_e(0) \approx 4 \text{ keV}$ . For an optically grey

plasma, the absorption and emission coefficient depends on  $n_e T_e^2$ , and the fact that increasing density did not change the X3 spectrum indicates that the emission is not optically grey anymore, and became optically thick. For these plasma parameters with high  $n_e$  and moderate  $T_e$ , the X3 emission is showing black-body conditions.

The motivation to explore the X3 emission is supported by the fact that in the concerned high-density regime beyond the X2-mode cutoff, the X3 emission starts to become optically thick. However, for a quantitative understanding, it is essential to characterize the X3 emission using radiation transport calculations. The dependence of the X3 emission on different plasma parameters is explored in the next section.

## 3.2 X3-mode emission

For a magnetic field of 2.5 T, the X3 emission has a cutoff at a plasma density  $\approx 3.65 \times 10^{20} \text{ m}^{-3}$ , which is sufficiently high compared to the X2 emission cutoff. The X3 emission will not be subject to a cutoff for the expected W7-X operation scenarios. The re-absorption in the plasma or optical depth of the X3 emission depends on  $T_e$  and  $n_e$  profiles of the plasma. Only if the re-absorption of the X3 emission is high enough in the plasma so that it is optically thick, then  $T_{rad}$  of the emission directly represents  $T_e$ . Hence, the primary question is for which plasma parameters  $T_e$  can be extracted directly from the X3 emission. This question is answered in this section by calculation of the radiation temperature and optical depth of the X3 emission for different  $T_e$  and  $n_e$  profiles. As a starting point, the  $T_e$  and  $n_e$  profile shapes are kept flat and constant over the plasma radius, and only the  $T_e$ ,  $n_e$  values are varied to study the X3 emission. As a second step, the  $T_e$  and  $n_e$  profile shapes are also varied to investigate the X3 emission. Finally, an X3 emission radiation temperature scan was done for the relevant  $T_e$  and  $n_e$  values covering the high density plasma parameter regime of W7-X. As for plasma parameters where the X3 emission is optically grey, the  $T_{rad}$  would be lower than  $T_e$  values. Hence, this scan provides an estimate of a correction factor to correct the measured  $T_{rad}$  so that  $T_e$  can be derived for the direct diagnostic applicability of optically grey X3 emission. These studies of X3 emission are discussed in the next sections.

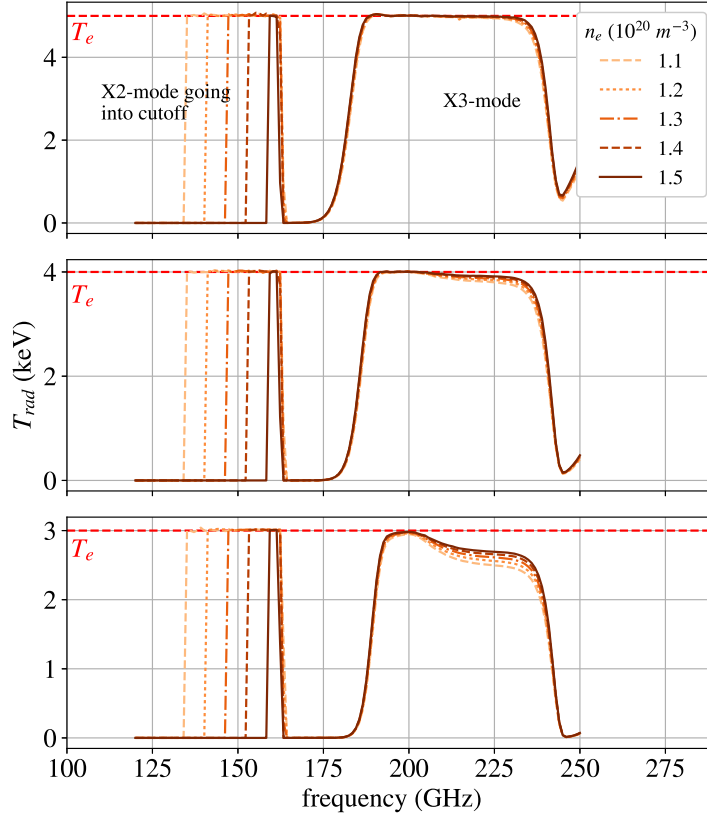


Figure 3.3: Radiation temperature of X-mode emission covering  $2^{nd}$  and  $3^{rd}$  harmonic calculated from radiation transport calculations done with TRAVIS for three different  $T_e$  values of 3 keV (bottom), 4 keV (middle), 5 keV (top). For each  $T_e$ , the  $n_e$  is varied from  $1.1 \times 10^{20} \text{ m}^{-3}$  to  $1.5 \times 10^{20} \text{ m}^{-3}$  such that X2-mode goes into cutoff from LFS. The plasma density and electron temperature profiles are chosen to be flat over the whole plasma radius,  $\rho$ .

### 3.2.1 Flat plasma profiles

The basic dependencies are investigated by assuming flat  $n_e(\rho)$  and  $T_e(\rho)$  profiles, a fixed plasma equilibrium, and neglecting reflections at the back wall of the plasma vessel.  $T_e$  is varied in three steps from 3 keV to 5 keV. For each flat  $T_e$ , the  $n_e$  is varied from  $1.1 \times 10^{20} \text{ m}^{-3}$  to  $1.5 \times 10^{20} \text{ m}^{-3}$ . These plasma parameters reflect the region of interest for an application of X3-ECE as a  $T_e$  diagnostic. For numerical reasons, the ray tracing is stopped after reaching  $e^{-\tau} < 10^{-4}$ , and hence, the upper limit of  $\tau$  is set to  $\approx 10$ .

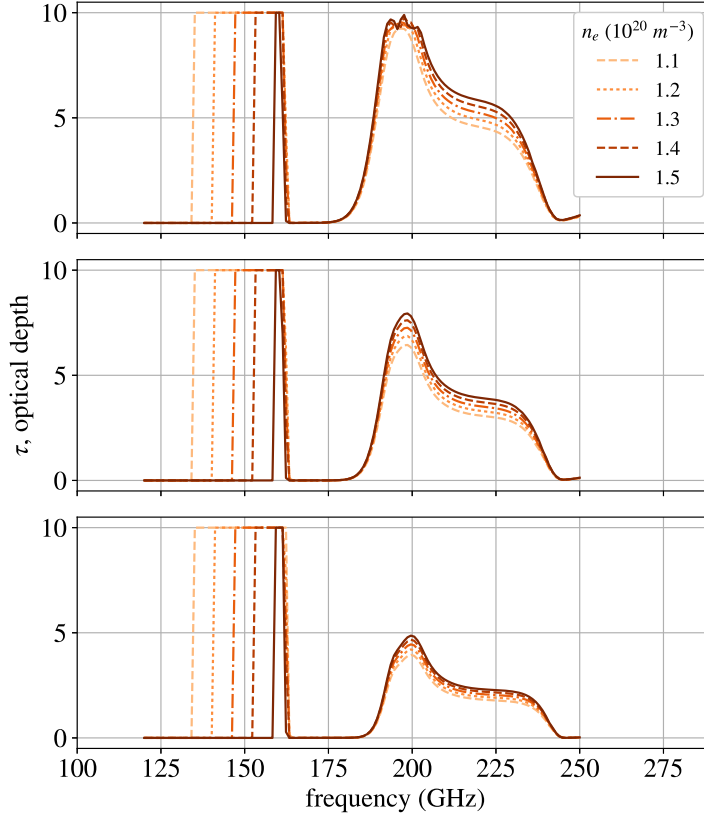


Figure 3.4: The optical depth corresponding to the X-mode emission shown in figure 3.3 (same order for the  $T_e$  values). The high values of  $\tau > 10$  are numerical set to  $\tau \approx 10$  in TRAVIS.

Figures 3.3 and 3.4 show  $T_{rad}$  and optical depth of the X2 and X3 emission for the flat plasma profiles. For all cases, the X2 emission has a high  $\tau$  above 10 (see fig. 3.4), and hence, the  $T_{rad}$  is equal to  $T_e$  (see fig. 3.3). At all  $T_e$  values, the X2 emission is fully present (approximately 135 – 165 GHz) only at  $n_e$  of  $1.1 \times 10^{20} \text{ m}^{-3}$ . For higher  $n_e$  above  $1.2 \times 10^{20} \text{ m}^{-3}$ , the X2 emission starts to gradually go into cutoff ( $T_{rad}$  in the spectra goes to zero) starting from the LFS frequencies. In contrast, the full X3 emission is present for the same densities.

For a  $T_e = 3 \text{ keV}$  (see bottom fig. 3.4), most of the X3 emission has a low  $\tau$  around 2.5, except few frequencies near 200 GHz, which have  $\tau$  approximately equal to 5. Hence, for these frequencies near 200 GHz,  $T_{rad}$  becomes nearly equal to  $T_e$  (see bottom fig. 3.3), which suggests that the emission is optically thick representing

black body conditions. At higher  $T_e$  value of 5 keV (see top fig. 3.4), it can be seen that most of the X3 emission is optically thick ( $\tau > 5$ ), and  $T_{rad}$  is nearly equal to  $T_e$  (see top fig. 3.3).

For the density range of interest, it can be seen from these calculations of optical depth (fig. 3.4) that the influence of  $n_e$  on  $\tau$  is only moderate, and the decisive quantity is  $T_e$ . Additionally, the optical depth is asymmetric with respect to the X3 emission frequencies for these flat profiles. The possible reason is that the line of sight (which is included in the radiation transport calculations from TRAVIS) for ECE collects radiation from the LFS, and the optical thickness is higher at LFS.

The simulation results show that X3 emission has a tendency to become optically thick at high plasma densities of interest, which can further be explored for diagnostic purposes. However, for high densities and low  $T_e$ , the direct application of X3 emission as  $T_e$  diagnostic can only use the central frequencies around 200 GHz. This optically thick X3 emission frequency would vary with a change in the magnetic field at the plasma axis. The X3 emission at the surrounding frequencies only becomes optically thick at high  $T_e$  values throughout the plasma radius.

In W7-X, the  $T_e$  and  $n_e$  profiles are generally not flat and depend on the plasma heating, fueling, and transport. Hence, the plasma profile shape plays a crucial role in investigating the optical depth of the X3 emission. This is explored in the next section by varying the profile shapes for radiation transport calculations of the X3 emission.

## 3.2.2 Profile shape dependence

### 3.2.2.1 Variation of $T_e$ profile

For the investigations of the X3 emission for different  $T_e$  profile shapes, the plasma core  $T_e(0)$  value is kept constant, and only the profile shape is varied. The  $n_e$  profile is also kept constant and flat with a value of  $1.3 \times 10^{20} \text{ m}^{-3}$ . The  $T_e$  profile shape is varied in two steps, changing the profile gradient in the first half of plasma radius near plasma core (fig. top 3.5a), and then in the second half of plasma radius near the edge of plasma (fig. bottom 3.5a).

In the previous section with a flat  $T_e$  profile and  $T_e(0) = 3 \text{ keV}$ , it has been shown already that only a few frequencies near the center of the X3 emission remain optic-

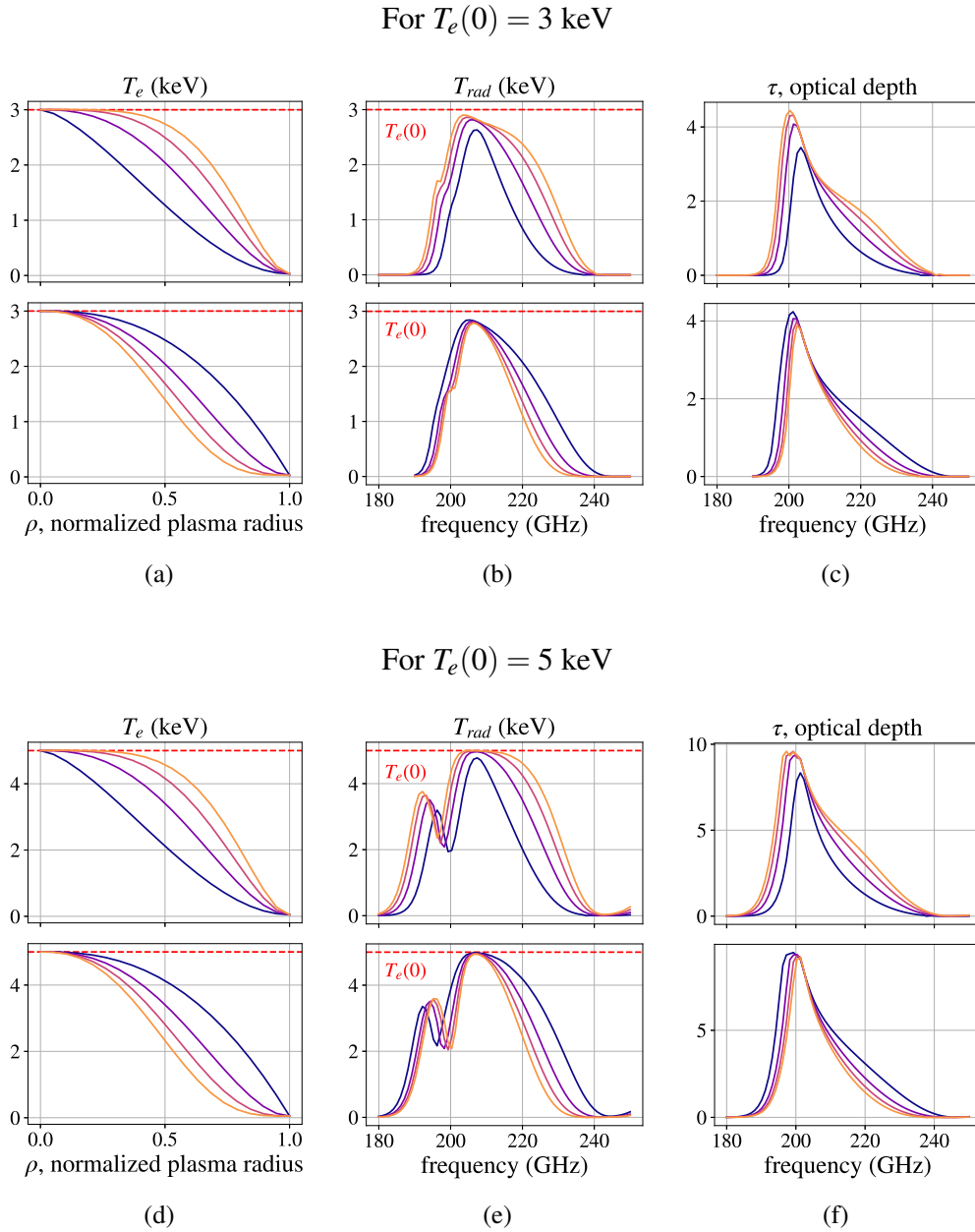


Figure 3.5: (a) The  $T_e(\rho)$  profile shape is varied with a fixed plasma core  $T_e(0) = 3$  keV to investigate (b) the radiation temperature and (c) optical depth of X3 emission. The  $n_e(\rho)$  profile is kept constant and flat with a value of  $1.3 \times 10^{20} \text{ m}^{-3}$  over plasma radius for all these case studies. (d) These studies are also done at a plasma core  $T_e(0) = 5$  keV and the corresponding (e) radiation temperature and (f) optical depth of X3 emission are shown.

ally thick (see bottom fig. 3.4). If at the same  $T_e(0) = 3$  keV, the  $T_e$  profile is made narrower (see top fig. 3.5b), then not only the  $T_{rad}$  at the edge decreases, but also the central  $T_{rad}$  decreases, indicating that the plasma is optically grey.

It can be seen that the variation of the profile near the plasma core influences  $\tau$  (see top fig. 3.5c) more in comparison to the variation in profile near the edge (see bottom fig. 3.5c). Moreover, for a really peaked  $T_e$  profile,  $\tau$  decreases drastically (see fig. 3.5c top). Hence, for a direct applicability of the X3 emission as a  $T_e$  diagnostic, a flatter  $T_e$  profile near the plasma core is optimal at a high density and  $T_e \leq 3$  keV.

The re-absorption of the X3 emission in the plasma depends more strongly on the  $T_e$  than on  $n_e$ . Hence, these studies are repeated at a higher  $T_e(0)$  of 5 keV but for the same plasma density (see fig 3.5e and 3.5f). In the simulation of the flat profile, the X3 emission at these plasma parameters has a high  $\tau$  (see fig. 3.4 top). The high value of  $\tau$  remains, if the  $T_e$  profile is made narrower as indicated in figure 3.5f. The exception is the peaked  $T_e$  profile, where  $\tau$  decreases enough so that  $T_{rad}$  is lower than  $T_e$  (see top fig. 3.5e). Additionally, the spectra at 5 keV are more symmetrical around the central X3 emission in comparison to those at 3 keV. The second peak in the spectra is caused by the relativistically downshifted emission from the hot plasma core electrons. As expected, this downshifted peak is more influenced by the variation of the  $T_e$  profile near the plasma core (see fig 3.5e top) than the variation at the edge (see fig 3.5e bottom).

To summarize these results, the effect of the  $T_e$  profile shape on the X3 emission is stronger when the majority of the X3 emission is optically grey (as for  $T_e = 3$  keV). For these parameters,  $\tau$  also decreases with increasing degree of  $T_e$  profile peaking. At W7-X, typical  $T_e$  profiles are close to these peaked profiles. Hence, this finding is important when considering the X3 emission for diagnostic purposes.

### 3.2.2.2 Variation of $n_e$ profile

The re-absorption and hence the optical depth of the X3 emission is also investigated for different profiles shapes of  $n_e(\rho)$ , indicated in figure 3.6. The  $n_e$  profiles are varied with the same plasma core  $n_e(0)$  of  $1.3 \times 10^{20} \text{ m}^{-3}$ . The re-absorption is strongly dependent on  $T_e$  and hence the profile is kept flat with two values, 3 keV and 5 keV. It can be seen from figure that, at both  $T_e(0)$  values,  $\tau$  of the X3 emission

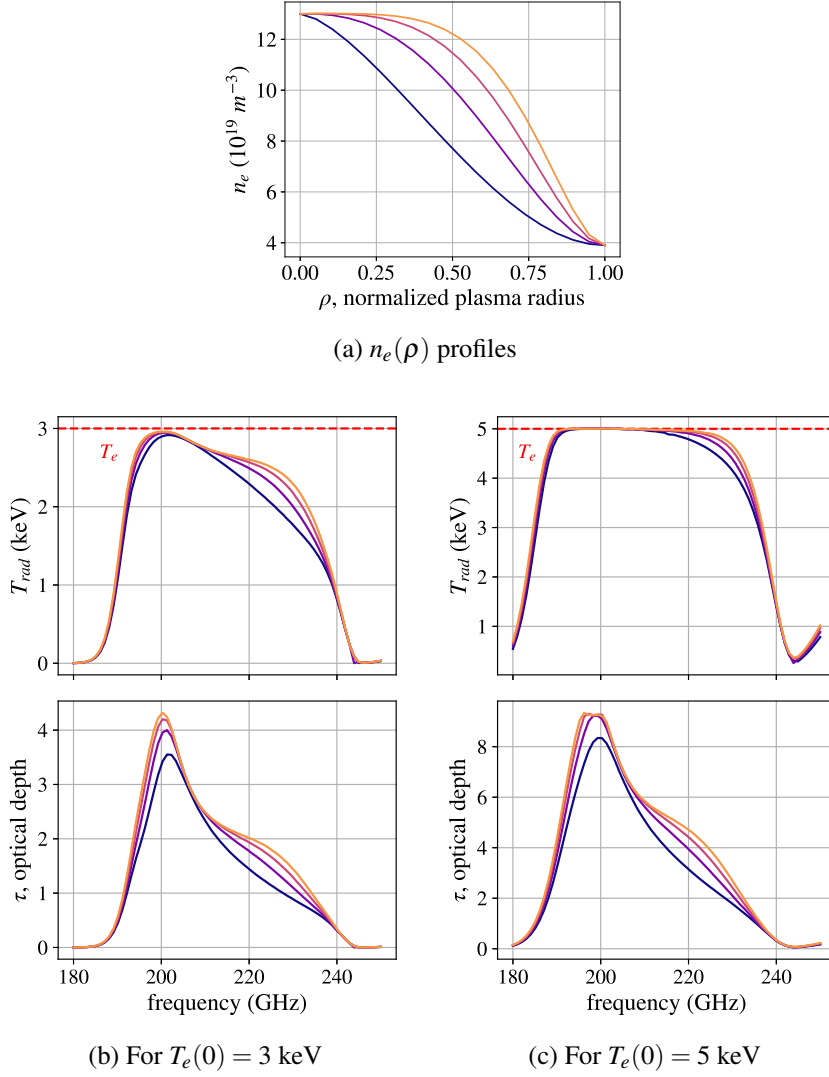


Figure 3.6: (a) The  $n_e(\rho)$  profile shape is varied with fixed plasma core  $n_e(0) = 1.3 \times 10^{20} \text{ m}^{-3}$  to investigate radiation temperature and optical depth of X3 emission (b) at  $T_e(0) = 3$  keV and (c) at  $T_e(0) = 5$  keV. The  $T_e(\rho)$  profile shape is constant and kept flat over plasma radius for all these studies.

decreases as the  $n_e(\rho)$  profile shape becomes peaked. However, this decrease in  $\tau$  is not significant as the  $T_{rad}$  is still equal to the  $T_e$  value over a wide radial range for  $T_e(0) = 5$  keV, and it remains close to  $T_e$  at least in a significant frequency range for  $T_e(0) = 3$  keV. Hence, for both scenarios it can be concluded that, first, where the X3 emission is partially optically grey (at  $T_e(0) \leq 3$  keV) and, second, where it

is mostly optically thick (at  $T_e(0) \leq 5$  keV), the  $n_e$  profile shape is not crucial for the application of the X3 emission as a plasma diagnostic.

As a rule of thumb  $\tau \geq 3$  is sufficient for  $T_{rad}$  becoming equal to  $T_e$ . In the next section, the optical depth of the X3 emission, covering the different plasma parameters of interest, is studied to find the regimes where the X3 emission can be used as plasma core  $T_e(0)$  diagnostic.

### 3.2.3 Plasma parameter scan

The radiation temperature of the X3 emission is calculated for a wider range of plasma parameters with  $n_e(0)$  varying from  $1.1 \times 10^{20} \text{ m}^{-3}$  to  $1.5 \times 10^{20} \text{ m}^{-3}$  and  $T_e(0)$  varying from 2 keV to 5 keV. This specific range of parameters is chosen because the W7-X plans to achieve high densities with O2-ECRH, and the O2 absorption is only efficient above an electron temperature of 2 keV. The  $n_e$  profile shape is kept constant and flat because previous simulations show that it doesn't influence the optical depth of the X3 emission much for the concerned parameter range. Three different  $T_e$  profile shapes, ranging from peaked to broad profiles, are chosen for these investigations. This is motivated by the fact that for peaked  $T_e(\rho)$  profiles, the X3 emission is optically grey, and hence a correction factor is required to estimate the true  $T_e$ . For the direct usability of the radiation temperature of X3 emission as a  $T_e$  measurement, specially for the optically grey plasma, the correction factor is defined in the following way.

$$correctionfactor = \left( \frac{T_e(0)}{T_{rad}} - 1 \right) \times 100 \quad (3.1)$$

This definition is chosen to provide the direct percentage increase of the measured  $T_{rad}$  value to estimate the plasma core  $T_e(0)$ . Figure 3.7 shows this correction factor for  $T_{rad}$  of X3 emission to reach plasma core  $T_e(0)$  values for different plasma parameters. The  $T_{rad}$  is shown for the central frequency ( $\approx 207$  GHz) of X3 emission, which depends on the magnetic field at the plasma axis.

This correction factor depends on the  $T_e(\rho)$  and  $n_e(\rho)$  profiles, and it decreases with increased  $T_e(0)$  and  $n_e(0)$  as the re-absorption of X3 emission increases in the plasma and eventually, the emission becomes optically thick representing the

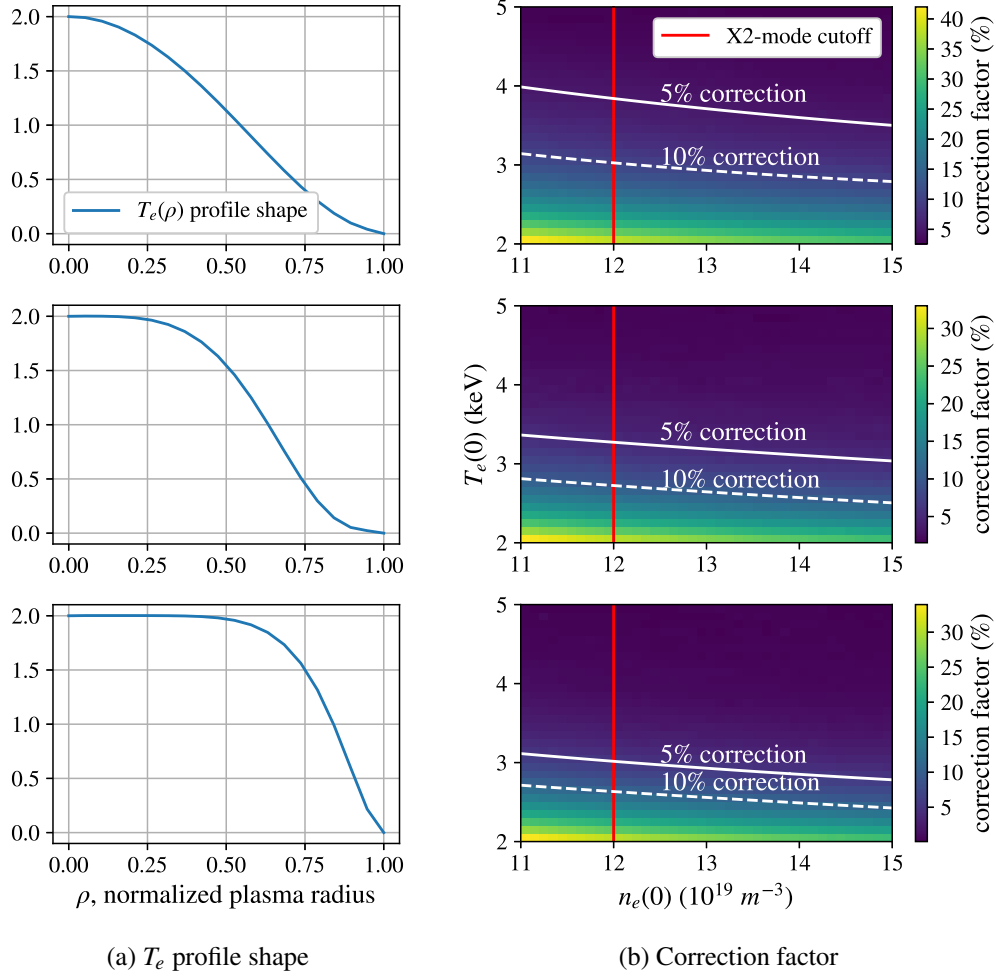


Figure 3.7: (a) Three  $T_e(\rho)$  profile shapes are chosen, peaked (top), broad near the plasma core (middle) and broad until the half plasma radius (bottom), to perform a plasma parameter scan of the X3 emission. The  $n_e(\rho)$  profile shape is kept constant and flat for all these investigations and only the core  $n_e(0)$  and  $T_e(0)$  are varied. (b) The correction factor (see eq. (3.1)), for  $T_{rad}$  of X3 emission to reach plasma core  $T_e(0)$ , is shown for three  $T_e(\rho)$  profiles shapes and for different  $n_e(0)$ ,  $T_e(0)$ . The correction factor is shown for  $T_{rad}$  of X3 emission at 207 GHz. The  $n_e$  for X2-mode emission cutoff is marked in figure.

black-body conditions for which the radiation temperature matches the  $T_e(0)$  value. In general, for concerned plasma densities, the X3 emission is optically thick for core  $T_e(0) \geq 3$  keV, and the correction factor is less than 5% for all profile shapes

of  $T_e(\rho)$  except peaked profile, for which its less than 10%. However, for core  $T_e(0) \leq 3$  keV, the X3 emission is optically grey and the correction factor is approximately 10 – 30% for all  $T_e(\rho)$  profile shapes except peaked profile, for which its approximately 20 – 40% (see fig. 3.7 top).

These radiation transport studies for high plasma density beyond X2 cutoff can be summed up as follows. For broader  $T_e(\rho)$  profiles, the X3 emission is nearly optically thick ( $\tau \geq 3$ ). However, only for very peaked profiles, which are not likely to be expected with neutral-beam injection (NBI) and O2-ECRH plasma, the X3 emission is optically grey ( $\tau < 3$ ).

For this work, the X3 emission is also measured experimentally for different plasma parameters of W7-X with a Fourier transform spectrometer (FTS) and the details of the measurements are elaborated in the next chapter.

# Chapter 4

## Fourier transform spectroscopy

The details discussed in this chapter were already published [47, 58]<sup>1</sup> electron cyclotron emission (ECE) radiation from fusion plasmas is in the microwave range. An ECE diagnostic measures this microwave radiation from the plasma in a magnetically confinement device. Absolute calibration of the intensities of this microwave radiation in terms of black-body radiation provides the radiation temperature. Depending on the radiation transport in the plasma, this radiation temperature is used to provide the electron temperature of the plasma. The physics principles of ECE diagnostic to probe electron temperature profile were already elaborated in chapters 1 and 2. The diagnostic setup of the Martin-Puplett interferometer (or Fourier transform spectrometer (FTS)) to measure the broadband ECE is described in detail, and also the absolute calibration factors are provided in the next sections.

### 4.1 Diagnostic description

The schematic of the diagnostic setup is shown in figure 4.1. The diagnostic is looking at the bean-shaped magnetic flux surfaces from the low field side (LFS) in the plasma vessel of Wendelstein 7-X (W7-X). The selection of this line of sight is elaborated in the next section. The ECE beam focusing is essential for the precise collection of the emission from the core of the plasma and for avoiding the unwanted radiation from neighboring magnetic flux surfaces from entering the trans-

---

<sup>1</sup>Passages of this chapter are directly taken from these publications.

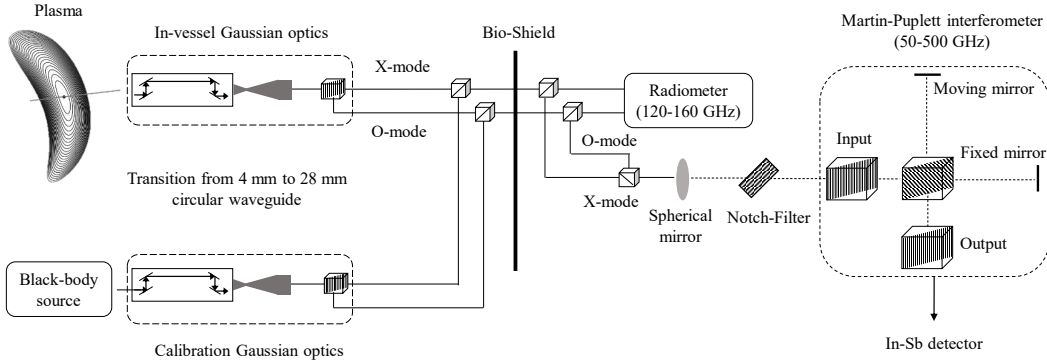


Figure 4.1: The overall diagnostic setup of Martin-Puplett Interferometer at W7-X is shown starting from left hand side with the bean shaped magnetic configuration of plasma indicating the ECE line of sight. A Gaussian optics consisting of four mirrors is used to focus the radiation from the plasma to broadband horn antenna and a wire-gird beam splitter separates the extraordinary mode (X-mode) and ordinary mode (O-mode) polarization of the ECE. These modes then propagate through the transmission line again after a broadband horn antenna and are finally focused on the stray radiation multi-mode notch filter by a spherical mirror before entering the interferometer. An In-Sb bolometer type detector is used to detect the interferograms from the ECE.

mission line of the diagnostic. Hence, the ECE beam from the plasma is focused with Gaussian optics consisting of four mirrors. This radiation is collected with a horn antenna that is optimized for broadband collection of microwave radiation. The focused beam is relayed by two transmission lines, and the transmission lines include many microwave components, such as miter bends and polarization tuners to adapt to the input of the Martin-Puplett interferometer and the radiometer. The torus hall of W7-X is closed during the operational phase, and hence, the plasma vessel cannot be accessed. This led to the development of a separate calibration unit which is a replica of the original Gaussian optics, antenna, and transmission lines. This calibration unit is successfully used to calibrate the radiometer [29]. Hence, the Martin-Puplett interferometer is also calibrated using this unit. The experimental setup is explained in the next sections.

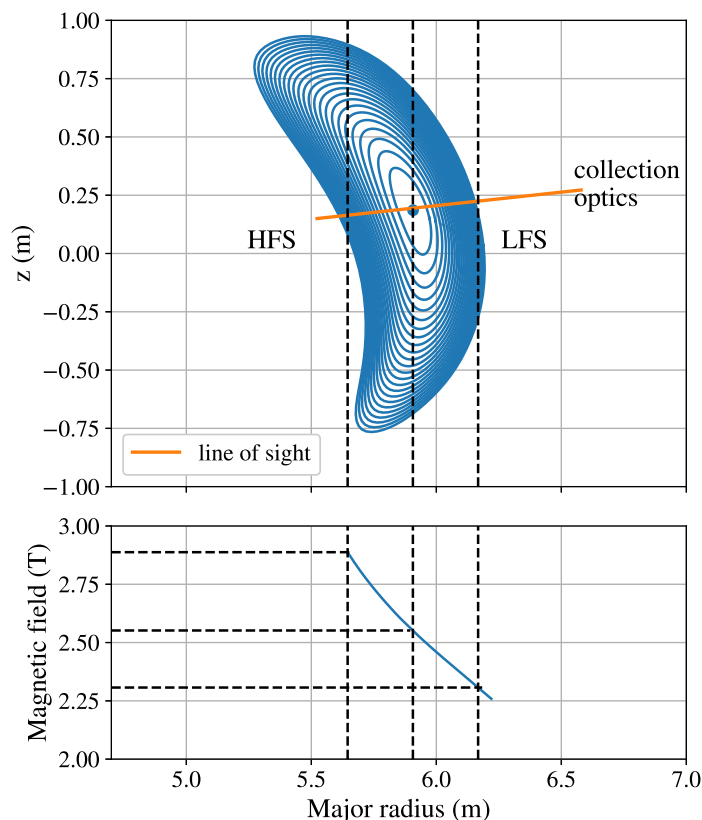


Figure 4.2: ECE line of sight in the plasma.

### 4.1.1 Line of sight

There are a few things that have to be considered when selecting the line of sight so that it is easier to interpret the ECE signals. For gathering a spatial  $T_e$  profile, ECE at different magnetic field surfaces is required, covering all plasma radii. Hence, the magnetic field should vary monotonically along the line of sight to gain localized information from ECE. In a stellarator, the magnetic field can also vary non-monotonically along a line of sight. However, similar to tokamaks, lines of sight are available, which have a monotonically varying magnetic field. The vertically elongated bean-shaped plane and its surroundings are used for this purpose in W7-X [31]. The ECE line of sight through the magnetic flux surfaces is shown in figure 4.2. The magnetic field is monotonically decreasing from the inside to the outside of the plasma vessel. In other words, the ECE antenna is collecting LFS emission.

The  $T_e$  profile needs the electron temperature information from the edge to the core of the plasma. Hence, the ECE line of sight should pass through the magnetic axis. However, the non-absorbed radiation from the electron cyclotron resonance heating (ECRH) gives rise to stray radiation [57] at 140 GHz. This requires the line of sight to be sufficiently away from the ECRH ports to reduce the stray radiation. Due to the helical axis in W7-X, the magnetic field in the center varies toroidally, and hence it is possible to select a sight-line where the ECE from the plasma center is not at 140 GHz. Thus, the plasma center can be observed at a different frequency despite the necessity to block the 140 GHz in the ECE measurement.

Doppler and relativistic effects are the main mechanisms responsible for the line broadening of ECE. The Doppler broadening can be reduced significantly by selecting a line of sight perpendicular to the applied magnetic field and ideally also to magnetic flux surfaces. For the chosen line of sight, the applied magnetic field is almost perpendicular with an angle of  $\sim 84^\circ$ . Since this angle varies over the line of sight, it is impossible to fulfill the condition of  $90^\circ$  along this sightline. Additionally, the use of the Gaussian optics narrows down the beam waist, which minimizes the Doppler broadening. Hence, this provides an enhanced spatial localization of the ECE. Since, ECE consists of both X-mode and O-mode emission, it is essential to separate the polarization to access pure X-mode or O-mode. This mode separation is discussed in the next section.

### 4.1.2 Mode separation

The ECE beam, exiting the plasma vessel through Gaussian optics, enters a 4 mm circular wave-guide via a horn antenna (see fig. 4.1). This antenna limits the number of modes propagating before transitioning to a broader 28 mm circular wave-guide. The beam exits the plasma vessel through a 100  $\mu\text{m}$  thick mica vacuum window with a broad transmission characteristic in the microwave range. The port window was optimized for the radiometer, which measures only the 2<sup>nd</sup> harmonic emission (120 – 160 GHz) and not for the interferometer, which covers a spectral range of 50 – 500 GHz. The horn antenna acts as a mode converter from a Gaussian to a TE11 mode, defined by the 4 mm circular input. Both polarization components, X-mode and O-mode, are present in the ECE beam. W7-X has a low magnetic

shear resulting in well-defined separation of X-mode and O-mode when radiation leaves the plasma towards the Gaussian optics. The plane of polarization of the applied magnetic field  $\vec{B}$  has a small deviation of  $\sim 6^\circ$  from perpendicular direction with respect to the ECE sight-line. This deviation was taken into account when aligning the wire-grid that was used as a polarization splitter to match the direction of the magnetic field. The X-mode polarization is transmitted through the wire-grid with maximum intensity and the O-mode polarization is reflected. Two identical circular waveguides with a diameter of 28 mm were used with several miter bends for the propagation of X-mode and O-mode to the input of the interferometer. The separation of modes is done close to the plasma vessel to reduce the risk of spurious mode conversion along the transmission line. The total length of the transmission line from the plasma vessel to the diagnostic input is approximately 23.7 m. The plasma is heated with electro-magnetic wave at a frequency of 140 GHz, which lies in the middle of  $2^{nd}$  harmonic ECE. As the non-absorbed incident electron cyclotron power at 140 GHz is very large compared to the ECE, it will saturate the detector signal or at least drive the detector to a non-linear voltage-current regime, which results in the obstruction of the measurement of the ECE harmonics. Even at much low stray radiation power, the interferogram will be dominated by only 140 GHz and the ECE spectrum will not be visible. Therefore, the attenuation of this non-absorbed stray radiation is a prerequisite to detect the broadband ECE from ECRH plasmas. Commercial notch filters are not available with the required broad transmission characteristics for a range from 50 to 500 GHz. Therefore, a multi-mode notch filter was designed for this specific application with a notch at 140 GHz.

### 4.1.3 Notch filter

Strong stray radiation from the non-absorbed ECRH power enters the X2 emission, and it overshadows the ECE spectrum, which hinders the measurements with the interferometer and the radiometer diagnostics. For this specific application, a notch filter is required for a narrow band stop at 140 GHz to attenuate this stray radiation. For the radiometer, a Bragg's notch filter [27] with a notch bandwidth of several 100 MHz is being used to attenuate the stray radiation by approximately 40 dB.

However, a mono-mode Bragg notch filter integrated into a waveguide can be used only for a limited frequency range, as it introduces notches at extra frequencies as well and, therefore, will not work for the broad spectral range of the interferometer. Therefore, a multi-mode notch filter [58] was designed, based on a multiple-layer dielectric structure with dielectric layers of high and low refractive indices [73, 74]. The theoretical transmission, reflection, and absorption of a multi-layer structure were determined by solving the Fresnel's equations [75], using the transmission-matrix-method, and determining the Poynting vector for each dielectric plate. The resonance condition for the transmission characteristics of such a structure can be optimized by the variation of the refractive indices and the width of the layers. Here, for the basic concept of the filter, a dielectric structure made up of multiple stacks of  $\lambda/2$  thickness with each  $\lambda/2$  stack consisting of two  $\lambda/4$  layers was considered. The transmission of this structure vanishes at odd multiples of frequency,  $f$ , corresponding to the design wavelength,  $\lambda$ . For practical reasons, the filter was constructed with  $3\lambda/2$  stacks instead of  $\lambda/2$  because of manufacturing tolerance limitations of the width of each dielectric layer, corresponding to wavelengths in the microwave range ( $\approx$  mm). The transmission of multi-layer  $3\lambda/2$  stack structure vanishes at odd multiples of the frequency of  $f/3$  such as  $f/3$ ,  $f$ ,  $5f/3$ ,  $7f/3$ . For this specific application  $f = 140$  GHz. The spectral width and attenuation depth of the notch at a frequency of  $f/3$  is a function of refractive indices of the dielectric layers and the number of stacks assembled. As a result of theoretical studies of the filter design, the spectral width of the notch is directly proportional to the difference of refractive indices of two dielectric layers in the stack, as shown in the following equation [73].

$$\frac{\Delta f}{f} = \frac{1}{45} \left[ \sin^{-1} \left( \frac{n_1 - n_2}{n_1 + n_2} \right) \right] \quad (4.1)$$

Where  $f$  and  $\Delta f$  are the notch frequency and spectral width,  $n_1$  and  $n_2$  are the refractive indices of the dielectric layers in the stack. The optical path difference between two reflecting beams from a single dielectric plate is a multiple of the cosine of the angle of refraction inside the plate. Consequently, the increase in the angle of incidence (AOI) would lead to a decreased optical path difference and hence a higher notch frequency. This advantage of the filter design can be used to fine-tune the filter near the design frequency. The AOI affects the transverse elec-

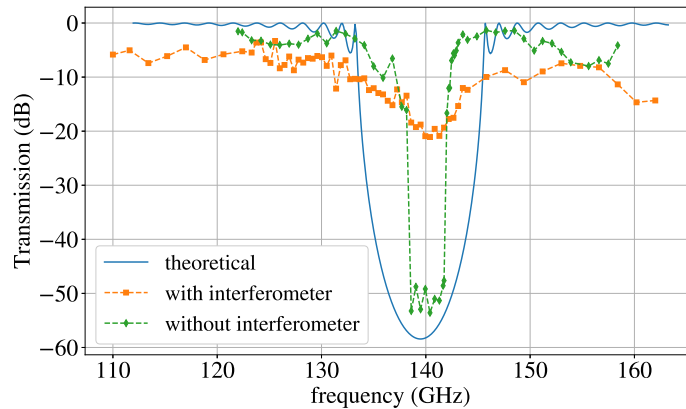


Figure 4.3: Experimental and theoretical transmission characteristics of the multi-mode notch filter are shown in the spectral range from 110 to 170 GHz.

tric and magnetic polarization of the incident radiation differently. However, the incident radiation at the input of the diagnostic was only transverse electric.

The finally chosen  $3\lambda/2$  dielectric stack is made up of two  $3\lambda/4$  layers of polytetrafluoroethylene (PTFE) and air with refractive indices 1.466 and 1, respectively [76]. The equation (4.1) shows that a small difference in refractive indices of the layers in a stack leads to a narrow notch width. In total, 19 such dielectric stacks of  $3\lambda/2$  thickness were used to assemble the final filter. The transmission characteristic of the filter was tested with a tunable microwave source in a range of 110-170 GHz, as shown in figure 4.3. The experimental observation shows a notch at 140 GHz. The notch width and attenuation vary with the experimental setup. The characterization done with the filter in between two 28 mm waveguides to couple and detect the power resulted in a notch width of 3 GHz and notch depth of 50 dB. It was observed that the experimental notch width is significantly less compared to theoretical predictions with this experimental setup. The possible reason could be that each PTFE layer in the filter was constructed by compiling three layers of PTFE to achieve a thickness of  $3\lambda/4$ . Because of this construction effect, one introduces more air-gap surfaces for multiple reflections than intended, hence affecting the resonance condition for transmission of the filter. However, when the filter was tested by placing it in front of the interferometer and a bolometer detector, a notch of approximately 10 GHz width and an attenuation depth of 20 dB was observed. The input beam to the filter was focused [77] with a spherical mirror as shown in

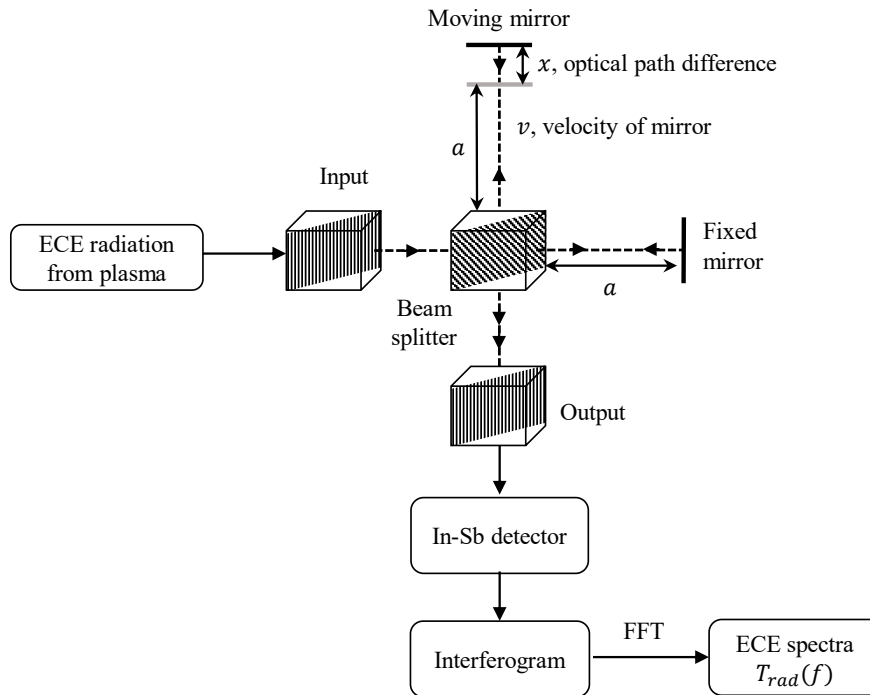


Figure 4.4: Schematic of the Martin-Puplett interferometer.

figure 4.1 and the output beam was not focused before entering the interferometer. As a result, the notch is wider and less deep. The experimentally measured insertion loss of the notch filter is of the order of approximately 6 dB. In conclusion, for the use of the filter in the diagnostic setup, it is essential to have well-defined optics at both the input and output of such a multiple-layer dielectric structure.

The interferometer is used for a broad spectral range of 50-500 GHz. For these frequencies, the filter produces four notches at 140, 234, 327 and 420 GHz in the spectrum. The filter was used at an AOI of approximately  $20^\circ$  with respect to normal incidence during the experimental campaign of W7-X to attenuate stray radiation from both X2-and O2-ECRH experiments at a frequency of 140 GHz. It was found that a 20 dB notch depth is sufficient to suppress the stray radiation. However, the notch width at 140 GHz is more than 10 GHz wide and which makes a large fraction of the  $2^{nd}$  harmonic ECE inaccessible for measurements of the X2 emission in ECRH plasmas.

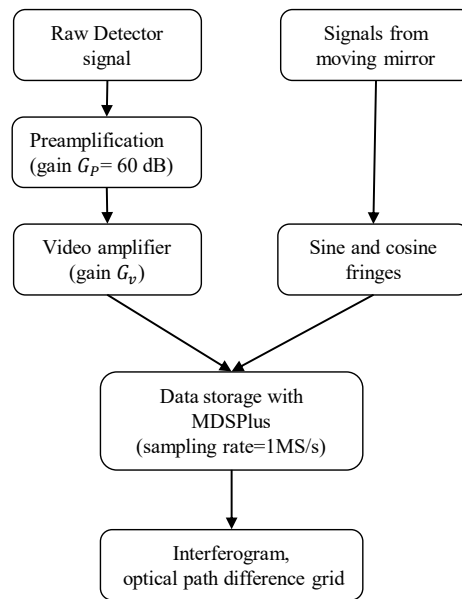


Figure 4.5: Block diagram showing the flow of the signal to extract interferogram and hence the ECE spectra.

#### 4.1.4 Martin-Puplett interferometer

Martin-Puplett interferometer (or Fourier transform spectrometer) [46, 48, 78] is a four-port device with two input and two output ports that are used to analyze the spectrum of the input radiation. The schematic of the interferometer is shown in figure 4.4. A wire-grid splits the input radiation beam into two arms of the interferometer, with one arm ending at a fixed mirror and the second arm consisting of a mirror moving at an average speed of approximately  $1 \text{ ms}^{-1}$ . The reflected beams from the mirrors are combined at the beam splitter, and the interference takes place at the detector surface. The moving mirror creates the optical path difference,  $x$ , between the two beams, which gives an interferogram signal with maxima and minima at the detector surface. The whole setup is mounted on an optical bench to reduce the effect of vibrations. Input and output ports are equipped with a wire grid to select a specific polarization that enters and exits the system. The interferometer limited to both X-mode and O-mode transmission lines.

An In-Sb detector, cooled to liquid helium temperatures, is used for the detection of the interferogram. The current-voltage characteristic curve of the In-Sb detector

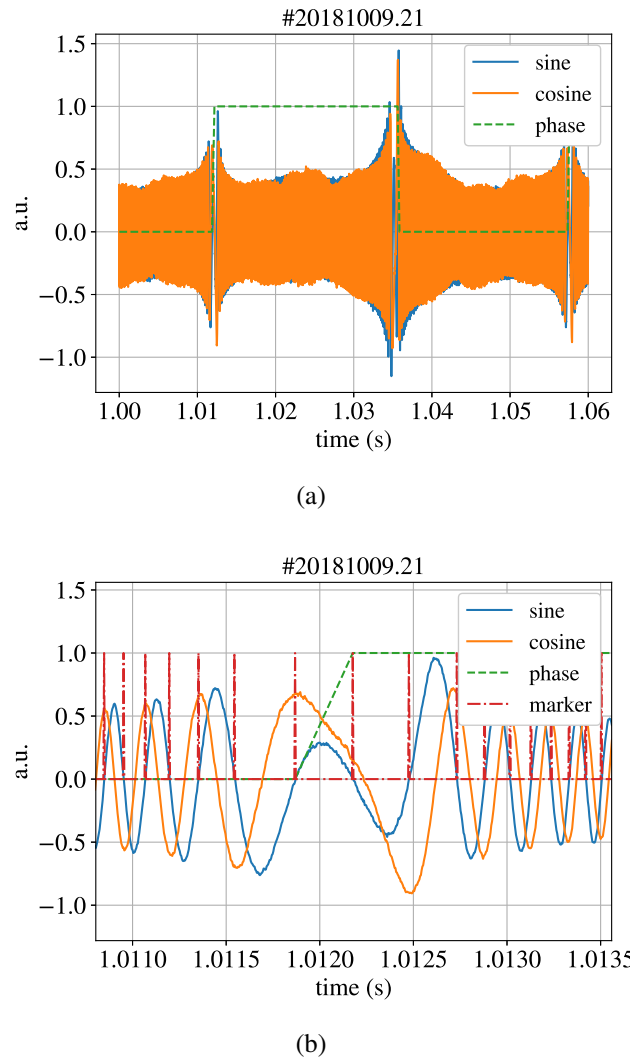


Figure 4.6: (a) Sinusoidal and phase signals corresponding to a full mirror sweep of 44 ms, combining both directions of scanning the maximum optical path difference of 30 mm. (b) A zoomed in view of (a) showing the sinusoidal, phase and marker signals at the location of mirror turning point.

was measured at room and liquid helium temperatures. It was verified that the detector operating point was set in the linear regime of the current-voltage curve response.

The signal processing after detection is shown using a block diagram in figure 4.5. A preamplification stage with a voltage gain of 60 dB (a factor of 1000) was applied to the detection signal. Additionally, a video amplifier was used at a gain

setting varying with plasma heating power. The stray radiation at the start of plasma may lead to the damage of the In-Sb detector or at least can cause the saturation of the signal. Thus, as the ECRH remains non-absorbed for the first 100 ms of a plasma, an automatic shutter was used for shielding the diagnostic. During the experimental campaign of W7-X, data were acquired with an FPGA at a sampling rate of  $2 \text{ MSs}^{-1}$ . The experimental data measured during the plasma experiments in W7-X consisted of interferograms and three signals providing optical path difference. These signals are sine and cosine fringes keeping track of the mirror movement and a phase signal to provide the time-point of mirror turnaround (see fig. 4.6a). The half period of the phase signal is also the temporal resolution of the diagnostic. The marker signal (see fig. 4.6b) gives the time-point when the mirror passes the  $20 \mu\text{m}$  steps. The maximum optical path difference between the two arms is twice the maximum mirror excursion in one direction. An optical path difference is required for providing the spectral resolution, and the frequency grid is required to overlay the fast Fourier transform (FFT) of the measured intensity of interferograms.

#### 4.1.5 Spectral and temporal resolution

The spectral resolution is the key quantity that determines the degree up to which the spectral characteristics of the input radiation can be recovered. The moving mirror of interferometer covers an excursion of  $15 \text{ mm}$  with steps of  $20 \mu\text{m}$ . This results in a minimum optical path difference between two beams of  $x_{min} = 40 \mu\text{m}$  and a maximum optical path difference of  $x_{max} = 30 \text{ mm}$ . The spectral resolution is directly proportional to the maximum optical path difference created between beams propagating in the two arms of the interferometer. The spectral resolution,  $\Delta f$ , is given by the following equation.

$$\begin{aligned} \Delta f &= \frac{c}{2 x_{max}} \\ &= \frac{c}{2 N x_{min}}, \end{aligned} \tag{4.2}$$

The maximum optical path difference,  $x_{max}$ , is achieved with  $N$  steps of a minimum optical path difference,  $x_{min}$ . This value of  $N$  is the total number of data points in the interferogram. The total number of data points required for FFT have to be equal

to a power of 2. However, as  $N \neq 2^n$ , the total number of data points are increased from  $N$  to  $N_1 = N + N_0$ .  $N_0$  are the zero padded to  $N$ . This results in a spectral resolution of  $\Delta f = 3.66$  GHz, corresponding to  $N_1 = 2^n = 1024$  data indices. The final frequency grid, which is required to evaluate the spectra, starts at 3.66 GHz and ends at  $2^n \times 3.66$  GHz.

The temporal resolution is a result of how fast the mirror can complete one optical path from zero to the maximum optical path difference. Hence, to have a high spectral resolution, one has to pay by reducing the temporal resolution and vice versa. Acceptable spectral and temporal resolutions can be achieved by optimizing the maximum mirror excursion and speed per excursion. At W7-X, the interferometer was commissioned with a maximum mirror excursion of 15 mm (mechanically limited) with a maximum speed of  $1 \text{ ms}^{-1}$ . The mirror frequency for a full sweep, covering both scanning directions, is approximately 22 Hz. This sweeping frequency cannot be increased further as this would over-strain the mechanical coupling between motor and mirror. The temporal resolution corresponding to this frequency is approximately 22 ms. For understanding the ECE harmonics and analyzing the X3 emission, 22 ms temporal resolution is fast enough as it is still smaller than energy confinement time which is in the range of 100 – 200 ms.

The calibration of the diagnostic is required to provide the radiation temperature of measured ECE intensities. The diagnostic was calibrated with a black-body source emitting broadband radiation at different temperatures. The interferograms and the FFT necessary to obtain frequency-dependent calibration factors are explained in the following sections.

## 4.2 Calibration

ECE has been used for many decades to provide electron temperatures for magnetically confined plasmas. Despite this, the calibration of the diagnostic is still a complex process. Absolute calibration is necessary to provide the sensitivity of the diagnostic to a change in the temperature of the input radiation. This is achieved with the hot-cold calibration technique. Two broadband sources with known emission characteristics are essentials for the implementation of this calibration technique. A black-body emitter made up of a ceramic material with a surface area of

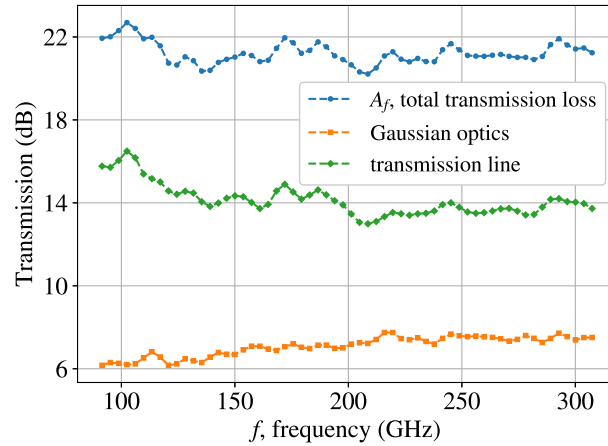
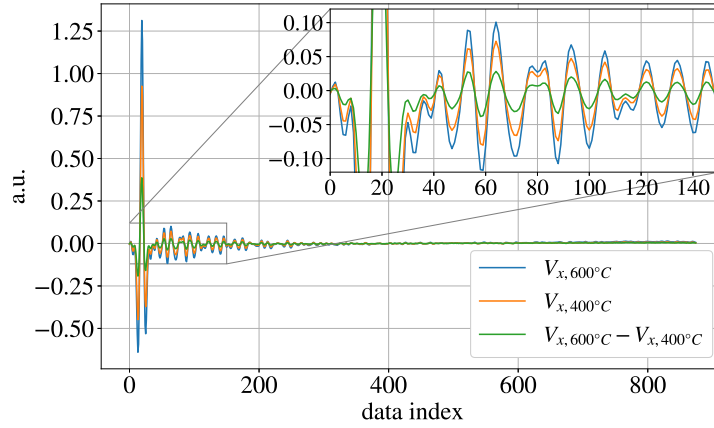
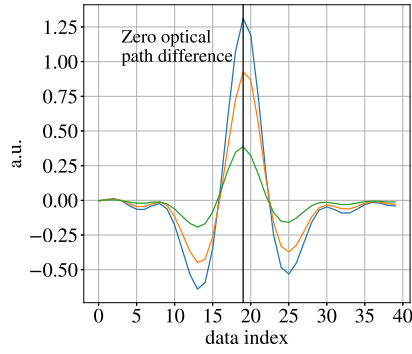


Figure 4.7: The total transmission line loss,  $A_f$ , for the propagation of ECE from the plasma to the input of the diagnostic is shown. Additionally, the individual transmission loss for the Gaussian optics, including the 4 mm waveguide and vacuum window, is shown.

approximately  $12 \times 12$  cm is used for the calibration. The black-body emitter can be tuned to temperatures between room temperature and  $600^\circ\text{C}$ , which is measured with a thermocouple. For the black-body emission in the microwave range, the signal-to-noise ratio is too low for measuring an interferogram corresponding to a single mirror sweep. The transmission line of the diagnostic setup is shown in figure 4.1. This transmission line has a transmission loss,  $A_f$ , of approximately 20 dB, which is shown in figure 4.7. The 4 mm waveguide used to focus the fundamental mode limits the number of modes propagating in the system and hence reduces the propagating power, which makes the calibration process difficult in the microwave range. Even with an increased integration time, the input power from the calibration source was not enough to gather enough signal. As a consequence, a different strategy was applied, calibrating the interferometer individually and later combining these calibration factors with the separately measured attenuation,  $A_f$ , of the transmission line. The data integration time had to be increased to four hours per calibration measurement of interferograms, and the averaging of the interferograms was performed over that full-time interval. The measured interferograms for the calibration are shown in the next section.



(a)



(b) Zoom of (a) showing Maximum intensity at zero optical path difference

Figure 4.8: Interferograms,  $V_x$ , from radiation emitted by the black-body source at two temperatures of 600°C and 400°C. The corresponding difference interferogram for a temperature change of 200 K is also shown.

### 4.2.1 Interferograms

The measured voltage,  $V_x$ , of an interferogram can be related to the intensity at a given frequency,  $I_f$ , of the emission, is given by the following equation.

$$V_x = G \text{FFT}^{-1} (C_i I_f), \quad (4.3)$$

Here,  $G$  is the amplification gain, and  $C_i$  is the calibration factor to get the emission intensity. For a black-body emission at a temperature,  $T$ , the spectral intensity

of emission,  $I_f$ , is given by the Rayleigh-Jeans law. Hence, this intensity of emission is directly proportional to the physical temperature of the black-body. For the black-body emission at two temperatures with a difference of  $dT$ , the corresponding difference of the interferograms,  $dV_x$ , is given by the following equation.

$$dV_x = G \text{FFT}^{-1}(C_t dT), \quad (4.4)$$

Here,  $C_t = C_i I_f / dT$  are the calibration factors to get radiation temperature of the emission. The hot-cold calibration of the interferometer was done with the black-body emission at two different temperatures of 400°C and 600°C. The interferograms at these two temperatures and the difference interferogram corresponding to the response of diagnostic to a change in the radiation temperature of 200 K are shown in figure 4.8. It can be clearly seen that diagnostic is sensitive to this temperature change. This change is described in the next section from the FFTs of these interferograms. To perform the FFT, it is advantageous to assign more weight to data points around zero optical path difference as these are the points containing more information. This is achieved by multiplying interferograms by a window function,  $w_x$  before performing the FFT. The window function used for this analysis is given by the following equation.

$$w_x = \cos\left(i \frac{\pi x_{min}}{2 x_{max}}\right); 0 \leq i \leq \frac{x_{max}}{x_{min}}, \quad (4.5)$$

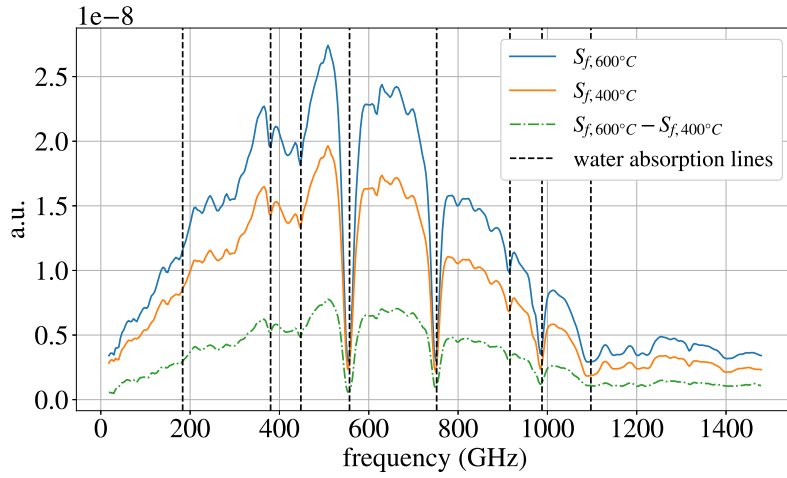
Here  $i$  is the mirror movement index. The difference spectra corresponding to the black-body emission at two temperatures are discussed in the next section.

### 4.2.2 Difference spectra

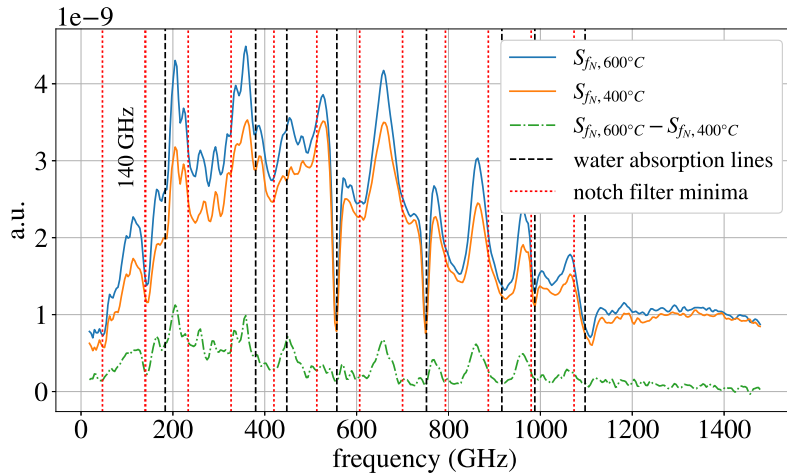
The FFT of the difference interferogram,  $dV_x$ , provides the difference spectra,  $dS_f$ , of a temperature difference of black-body emission.

$$dS_f = \text{FFT}(w_x dV_x) \quad (4.6)$$

The black-body source has low radiation power at low temperatures. Because of this, it was not possible to measure temperatures below 400°C with the transmis-



(a)



(b)

Figure 4.9: Spectra measured with the interferometer observing two temperatures,  $600^{\circ}\text{C}$  and  $400^{\circ}\text{C}$ , of a black-body. The water absorption lines [79] for a frequency range of 100-1100 GHz are present at 183.31, 380.19, 448, 556.93, 752.03, 916.16, 987.94 and 1097.37 GHz. (a) Difference spectra,  $dS_f$ , measured without the notch filter in the experimental setup and (b) difference spectra,  $dS_{f_N}$ , including the stray radiation notch filter. In addition to the water absorption lines, the notch filter resonance minima for the concerned frequency range (50-500 GHz) are present at 46.67, 140, 233.34, 326.67 and 420 GHz.

sion line losses included (see fig. 4.7). Hence, the black-body source was used at temperatures of  $600^{\circ}\text{C}$  and  $400^{\circ}\text{C}$  to derive the difference interferogram. The dia-

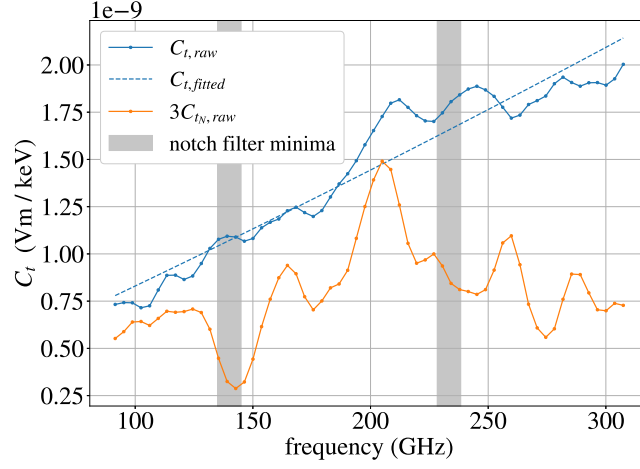


Figure 4.10: Calibration factors,  $C_t$ , without notch filter, and  $C_{t_N}$ , with notch filter are shown as a function of frequency. Also indicated are the expected 10 GHz wide notch filter minima at 140 and 233.34 GHz.

gnostic was calibrated with and without the stray radiation notch filter because the filter is only used for plasmas with ECRH and not with neutral-beam injection (NBI) heating. The corresponding difference spectra measured from the black-body emission are shown without notch filter in figure 4.9a and with notch filter in figure 4.9b. The common feature in both spectra is the water absorption lines, which are also used as a reference to validate the calibration. In the spectrum with the notch filter, there are the periodic notches as expected with one at 140 GHz and this assures that the stray radiation will not dominate the ECE. Two sets of calibration factors are determined to analyze the experimental results. These factors are shown in the next section.

### 4.2.3 Calibration factors

The calibration factors of the diagnostic is given by the following equation.

$$C_t = \frac{A_f dS_f}{G dT} \quad (4.7)$$

Here,  $A_f$  is the transmission loss given in figure 4.7. For the concerned plasma densities of the W7-X plasma, the ECE up to the 4<sup>th</sup> harmonic could be observed. Hence,

the calibration factors are only required for the frequencies below 300 GHz. This work is targeted at plasmas with higher densities where the 1<sup>st</sup> harmonic emission will be in the cutoff. Thus, the lower frequency limit for calibration is set at 100 GHz. Figure 4.10 shows the calibration factors which are used to get the radiation temperature of the ECE from the experimental measurements. The diagnostic sensitivity is of the order of  $10^{-9}$  V m/keV for the spectral range of 100 – 300 GHz without the stray radiation notch filter. After introducing the notch filter, the sensitivity of the diagnostic decreases by order of magnitude.

The experimental radiation temperatures of ECE for different plasma parameters of W7-X are discussed in the next chapter.

# Chapter 5

## Experimental results

The experimental results shown in this chapter are published to a significant extent [47]<sup>1</sup>. The electron cyclotron emission (ECE) measurements from high density plasmas are discussed with their dependence on plasma parameters. The radiation temperatures of the extraordinary mode (X-mode) emission are shown in this chapter. The ordinary mode (O-mode) emission can be accessed by this diagnostic as well, but it is not used for further analysis as the intensity of the emission from higher O-mode harmonics is extremely low. The optically thick first harmonic ordinary mode (O1-mode) emission is in cutoff for the concerned plasma density regime (beyond  $\approx 1 \times 10^{20} \text{ m}^{-3}$ ). Additionally, the polarization of ECE depends on the direction of magnetic field at the plasma boundary where the microwaves start to propagate in vacuum towards the Gaussian optics (see sec. 4.1.2). Hence, due to the slight variation of magnetic field direction along the line of sight there is always a mismatch present at all times with respect to pure separation of polarization from the wire-grid. This mismatch results in the leakage of strong X-mode into the O-mode measurement, polluting the O-mode spectra. On the other hand, X-mode is not affected much by the leakage of the weak O-mode, which is also seen by the radiometer measurements.

---

<sup>1</sup>Passages of this chapter are taken from this publication

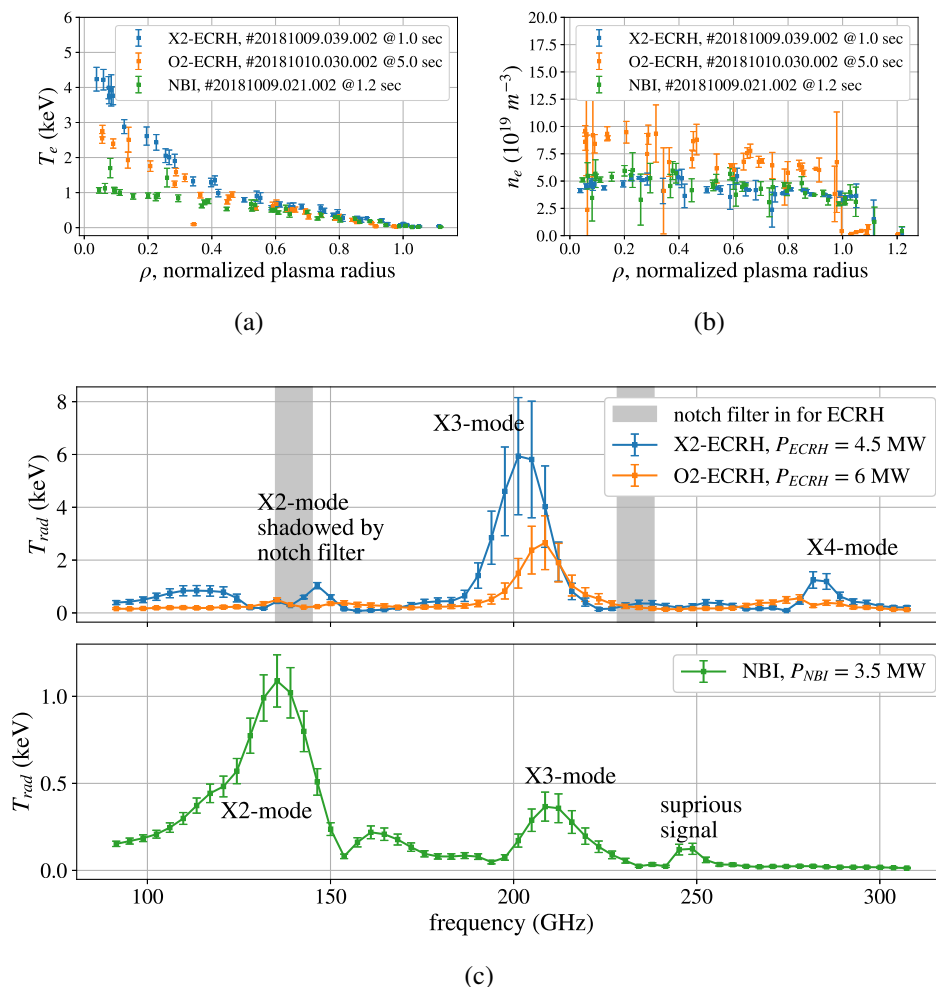


Figure 5.1: (a)  $T_e$  and (b)  $n_e$  profiles for three plasma heating scenarios using X2-, O2-electron cyclotron resonance heating (ECRH) and neutral-beam injection (NBI) heating. (c) Broadband X-mode ECE measured with the Fourier transform spectrometer (FTS) for the three different plasma heating scenarios.

## 5.1 Broadband X-mode

The X-mode measurements are discussed for three different plasma heating scenarios, X2-, O2-ECRH and NBI heating, which were available at Wendelstein 7-X (W7-X) in previous operational phases. However, as only the O2-ECRH and NBI heating are capable of achieving high plasma densities, mostly ECE from these

plasmas are discussed in the later sections. The intensities or radiation temperatures of ECE harmonics for different heating scenarios depend on the heating power and fueling. Hence, it was not possible to have identical profiles for the three heating schemes for the investigations of ECE spectra. The plasma profiles chosen from experiments for the comparison of the three heating scenarios are shown in figure 5.1. The corresponding heating power are as follows:  $P_{X2-ECRH} = 4.5$  MW,  $P_{O2-ECRH} = 6$  MW and  $P_{NBI} = 3.5$  MW. The  $T_e$  profiles (see fig. 5.1a) and  $n_e$  profiles (see fig. 5.1b) were measured with Thomson scattering diagnostic [80, 81]. This diagnostic uses the scattering of laser light on plasma electrons. The Doppler broadening of the scattered light is used to provide the electron temperature profile and the intensity of the scattered light provides the information on the plasma density profile. The error bars on the measurements from the Thomson scattering diagnostic are only statistical and do not take into account all systematic errors.

The measured X-mode spectra from the FTS for these three heating scenarios are shown in figure 5.1c. The error bars on the measurement are from the fitting of the calibration factors using Gaussian processes. During the ECRH plasma the multi-mode stray radiation notch filter (see sec. 4.1.3) was used to attenuate the non-absorbed power. Hence, the second harmonic extraordinary mode (X2-mode) emission around 130 – 150 GHz is blocked in these cases. In contrast, the third harmonic extraordinary mode (X3-mode) and fourth harmonic extraordinary mode (X4-mode) emission are seen in the X2-ECRH. For O2-ECRH case only X3-mode emission is seen, because of the high plasma density and lower  $T_e$ . For NBI heated plasma, as there is no stray radiation the notch filter could be omitted, and both X2-mode and X3-mode emission are visible simultaneously. Additionally, there is an unknown spectral feature present near 160 GHz. The possible reason behind this feature could be wall reflections. The feature around 244 GHz is not from the plasma. It originates from the radiometer mixer signal, as both the FTS and the radiometer share the same transmission line. The X4-mode is not visible as the heating power is too low with NBI. Hence, as only purely NBI heated plasmas show both X2-mode and X3-mode emission, they are used here to study their relative optical depth.

As this work is focused on the high density application of ECE, an example, of experimentally measured broadband X-mode ECE spectra from purely NBI heated

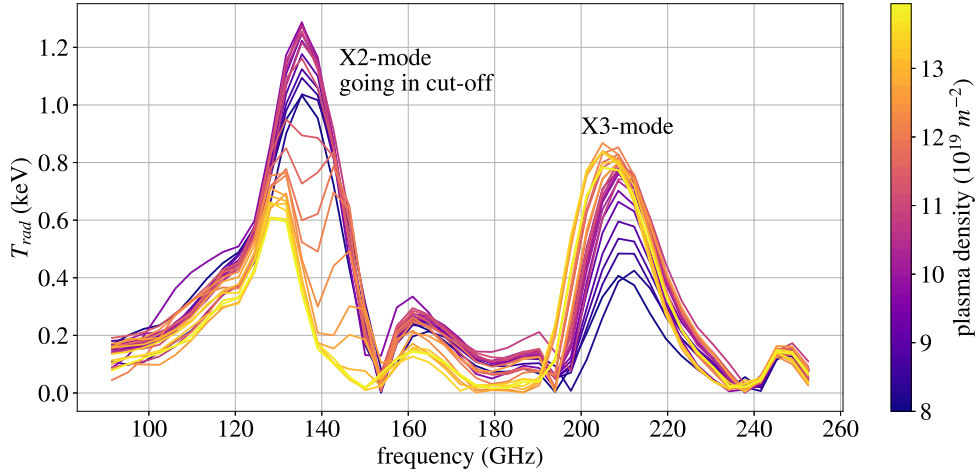


Figure 5.2: X-mode radiation temperature spectra are shown from purely NBI heated plasma. The plasma density is increasing in a linear ramp from  $8 - 14 \times 10^{19} \text{ m}^{-3}$  (as shown with color bar) and the electron temperature is almost constant at a value of 1.2 keV.

plasma, is discussed. This example is chosen as the electron temperature during the plasma discharge, as measured with Thomson scattering, stays almost constant with a value of 1.2 keV and the plasma density is increasing in a linear ramp from  $8 - 14 \times 10^{19} \text{ m}^{-3}$ . This allows to display mainly the effect of the density increase on different ECE harmonics. The measured X-mode spectra are shown in figure 5.2. The X2-mode emission (130 – 150 GHz) is optically thick and the radiation temperature is equal to the electron temperature. This emission goes gradually into cutoff starting from the low field side (LFS) for plasma densities above  $12 \times 10^{19} \text{ m}^{-3}$  as expected. It is evident from this experimental observation that X2 emission  $T_{rad}$  is not available for high densities and hence, access to  $T_e$  from the X2 emission is not possible. Despite the constant  $T_e$ , the X3-mode emission (190 – 230 GHz) is increasing with the increasing plasma density. This observation is a signature of the increased re-absorption of the X3 emission in the plasma. However, the X3 emission remains optically grey as the  $T_{rad} \approx 0.8 \text{ keV}$  is lower than  $T_e \approx 1.2 \text{ keV}$  for these plasma parameters with low  $T_e$  and high  $n_e$ . This observation is consistent with the radiation transport calculation results discussed in the chapter 3. However, the X3 emission  $T_{rad}$  still can be used for a continuous local  $T_e$  measurement if a correction

factor is used as derived from TRAcing VISualized (TRAVIS) calculations (see sec. 3.2.3) for  $n_e$  beyond the X2 emission cutoff and for low  $T_e \approx 1$  keV. Additionally, there are other features present in the spectrum between the frequency range of X2 and X3 emission. These features around 160 GHz are not well understood and they are evidently arising from the plasma as the emission is decreasing with increasing  $n_e$ . The possible reasons behind this emission could be the wall reflections or the downshifted emission from the high field side (HFS). These unknown features are addressed using Bayesian analysis via a forward model of the diagnostic (in chapter 6).

## 5.2 X2-mode emission

At W7-X, there are two ECE diagnostics, the FTS and the radiometer, measuring the 2<sup>nd</sup> harmonic ECE from the same line of light. The radiometer is absolutely calibrated by the same calibration optics as the FTS. The main difference between the two diagnostics are the spectral and temporal resolution. The radiometer has better spectral (1.2 GHz) and temporal resolutions ( $\mu$ s) than the FTS. The comparison of measurements from the two diagnostics makes it easier to understand the instrument function of the FTS. Hence, a direct comparison of the X2-mode spectra is a good test of both diagnostics. As both diagnostics share the same transmission line with a polarizing beam splitter, each diagnostic selects either X-mode or O-mode. Hence, the X-mode measurements from both diagnostics are available only for similar plasma conditions and not for the same plasma. For the comparison, two similar NBI heated plasmas were chosen with  $T_e \approx 1.2$  keV and  $n_e \approx 9 \times 10^{19} \text{ m}^{-3}$ . Figure 5.3 shows the X2-mode spectra measured with the FTS and radiometer in a spectral range of 120 – 160 GHz. For the FTS, the notch filter is not used, but for radiometer a Bragg's notch filter [27] is used which attenuates the emission around 140 GHz with a notch width of few MHz. Hence, the emission is not available at a small band around 140 GHz. The peak radiation temperatures from the two diagnostics are in agreement which validates the calibration of the FTS. The HFS of the spectra are in relatively good agreement as well. The spectral features are more smooth with the FTS because of its relatively poor spectral resolution in comparison to radiometer. However, at LFS the two diagnostics don not agree. A possible reason is the high

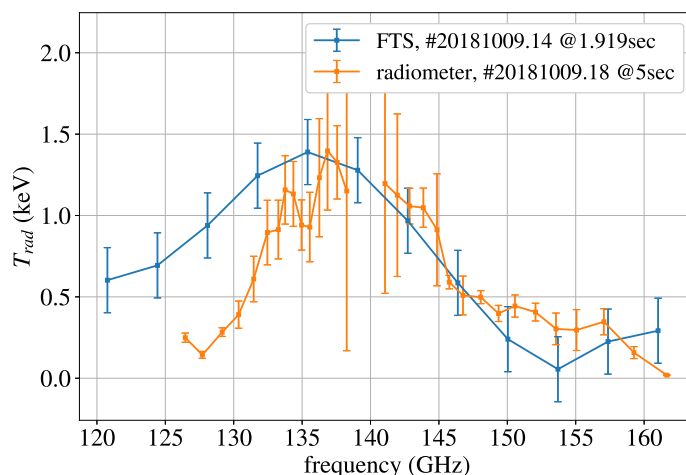


Figure 5.3: A direct comparison of the X2-mode emission spectra measured with the FTS and heterodyne radiometer are shown.

uncertainty of the FTS calibration at lower frequencies because of the less intense emission from the black-body source at these frequencies (see fig. 4.8 and 4.10).

As the focus of the work is the X3 emission,  $T_{rad}$  from the X3-mode is directly compared to  $T_e$  measurements from Thomson scattering in the next section.

### 5.3 X3-mode emission

In this section two examples of X3-mode emission measurements from high density plasmas are discussed and compared with  $T_e$  measurement from Thomson scattering diagnostic. The first measurement is from a NBI heated plasma with increasing plasma density and low  $T_e$ . The continuous evolution of the X3-mode emission and  $T_e$  from Thomson scattering are shown in figure 5.4. Additionally, as the X2-mode emission measured with the FTS is available for a NBI heated plasma, it is also shown in figure. The frequencies chosen to show X2-mode and X3-mode correspond to the magnetic field at the center of the plasma axis. It can be observed that until 2.3 s, the  $T_{rad}$  of the X2-mode emission is equal to  $T_e$  from Thomson scattering as expected from its high re-absorption in the plasma, leading to black-body conditions. However, beyond this time-point, the plasma density increases

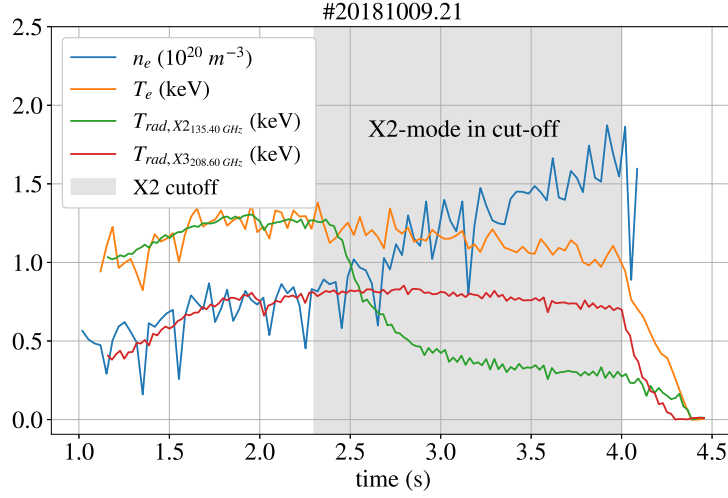


Figure 5.4: The radiation temperature of X2-mode (at 135.4 GHz) and X3-mode (208.6 GHz) emission measured with the FTS and electron temperature measurement from the Thomson scattering diagnostic is shown for a purely NBI heated plasma discharge with increasing high plasma density.

enough so that the X2-mode emission goes into cutoff for the rest of the plasma discharge. At the end (around at 4.3 s) of the plasma discharge during the plasma decay, the X2-mode emission recovers from the cutoff, because the plasma density decreases. The  $T_{rad}$  of the X3-mode emission is increasing during the start of plasma discharge and saturates at the end. As this  $T_{rad}$  for the NBI heated plasma conditions is still lower than the  $T_e$  value measured with Thomson scattering, the re-absorption of the X3 emission is not sufficient to represent black-body conditions. Hence, it is optically grey. However, its general behavior is similar to the  $T_e$  trace from Thomson scattering, indicating that with a reasonable correction factor (see sec. 3.2.3) the X3 emission can be used as a proxy for the central temperature.

The second measurement chosen here for the X3-mode emission is from a high density plasma with O2-ECRH, which is shown in figure 5.5. This specific measurement is chosen because  $T_e$  is around 2.5 keV. Higher electron temperatures at densities beyond the X2-mode cutoff are not yet available at W7-X, because of the limited plasma heating power. The figure compares the X3-mode emission with  $T_e$  from Thomson scattering for a plasma heated with O2-ECRH for plasma densities around  $1 \times 10^{20} \text{ m}^{-3}$ . The X2-mode emission is not available, because of the

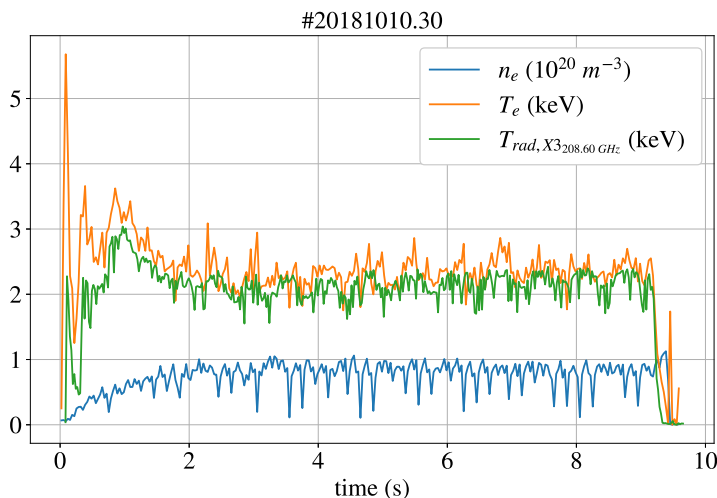


Figure 5.5: The radiation temperature of X3-mode emission (at 208.6 GHz) is shown alongside electron temperature measurement from Thomson scattering diagnostic for a continuous O2-ECRH plasma discharge with high density.

use of the stray radiation notch filter. At the start of the plasma discharge until 2 s, the  $T_{rad}$  of X3-mode emission is slightly lower than  $T_e$  from Thomson scattering, as the plasma densities are low leading to insufficient optical thickness. After this time point,  $T_{rad}$  becomes equal to  $T_e$ . This is an indication that the re-absorption of X3-mode emission at the central frequency is sufficient for these specific plasma parameters ( $T_e = 2.5$  keV,  $n_e = 1 \times 10^{20} \text{ m}^{-3}$ ) to represent black-body conditions. This experimental result is also supported by radiation transport calculations discussed in the chapter 3. In order to answer the question, whether the X3 emission also allows to determine a  $T_e$  profile besides the core  $T_e$  information, a forward model is constructed for the prediction of the X3 measurements covering the full spectral range (190 – 230 GHz). Such a forward model can also quantify the optical thickness in the frequency range from which one can access the information on the origin of the emitting electrons in the plasma. The forward modeling alongside the Bayesian analysis of these experimental results are discussed in the following chapters.

# Chapter 6

## Bayesian data analysis

The possibility to infer the  $T_e$  profile from the electron cyclotron emission (ECE) depends on the re-absorption of the emission in the plasma. For an optically thick ECE, the origin of the emission is spatially localized in the plasma arising from a narrow layer of typical width  $\approx 1$  cm behind the cold resonance. An increasing magnetic field along the line of sight of the diagnostic means that different magnetic field surfaces are mapped to a different spatial location along the plasma radius (see fig. 4.2). Hence, the emission frequency is mapped to the magnetic field surfaces and eventually the plasma radius  $\rho$ . This would result in a direct mapping of the  $T_{rad}(f)$  spectrum to the plasma radius  $\rho$ . However, this is not the case if the origin of the emission is not known. The quantification of the optical depth and the spatial origin of the third harmonic extraordinary mode (X3-mode) emission in the plasma is necessary to extract  $T_e$  profile through direct inversion of the experimental results of  $T_{rad}$ . For the scenarios of low optical depth, the emission originates from a wider range of the plasma and includes electrons with different kinetic energies. Hence, a straight forward inversion from  $T_{rad}(f)$  to  $T_e(\rho)$  is not possible anymore. Therefore, the scheme of Bayesian data analysis is adopted for this work using the forward modeling of the experimental results to extract  $T_e(\rho)$  from optically thin plasmas, which is elaborated in detail in the following section.

## 6.1 Principles of Bayesian data analysis

The Bayesian data analysis approach is based on the Bayesian probability theory, which is statistical inference. The classical statistical analysis is based on repeating the same experiment under identical conditions to extract the uncertainty of the observation. The drawback of this analysis is that the probability and uncertainty of the experimental observation vary with different numbers of repetitions of the experiment. However, the Bayesian probability is different from the classical probability, as it additionally includes the *prior* probability knowledge in the random variables or unknown parameters affecting the experiment. This *prior* probability gets updated with a new data set of measurements or by including additional observations, eventually increasing the knowledge of the experiment and factors affecting it. This increased knowledge is represented by a *posterior* probability. This interpretation of Bayesian probability for this work is to infer the underlying physics parameters from the observations. The Bayesian inference is characterized by models and parameters. The model is the formulation of how the experimental observation has been obtained from a certain diagnostic, and the parameters are the unknown factors or variables affecting this observation. The *prior* and *posterior* probabilities are linked by the quantity known as *likelihood*, which is the forward calculated probability of a certain observation given that the *prior* knowledge on the parameters is true. The *likelihood* is determined from the associated model of the diagnostic and its measurement process.

In the following, the Bayesian analysis is explained through the Bayes theorem in the context of the experimental observation of the radiation temperature spectrum,  $T_{rad}(f)$ . The main parameter affecting this observation is the electron temperature profile,  $T_e(\rho)$ . Bayes theorem [66] provides the conditional probability of  $T_e(\rho)$  given that the observation of  $T_{rad}(f)$  is true. It is given by the following equation.

$$P(T_e(\rho)|T_{rad}(f)) = \frac{P(T_{rad}(f)|T_e(\rho))P(T_e(\rho))}{P(T_{rad}(f))} \quad (6.1)$$

The term  $P(T_e(\rho))$  is the *prior* probability representing the knowledge of  $T_e(\rho)$  irrespective of the experiment. The term  $P(T_e(\rho)|T_{rad}(f))$  is the *posterior* probability, which represents the updated state of knowledge on the profile with new

measurement. The term  $P(T_{rad}(f)|T_e(\rho))$  is the *likelihood*, which links the *prior* and *posterior* knowledge on the diagnostic. From the Bayes theorem, the *Posterior* probability is the *prior* probability times the *likelihood*. The normalization quantity is known as the evidence,  $P(T_{rad}(f))$ , which is given by the following equation.

$$P(T_{rad}(f)) = \int P(T_{rad}(f)|T_e(\rho))P(T_e(\rho))dT_e \quad (6.2)$$

The Bayesian analysis approach assumes that the observation of  $T_{rad}(f)$  is true and there is some *prior* knowledge available on  $T_e(\rho)$ , which affects this observation. The combined *prior* knowledge of  $T_e(\rho)$  and the observation of  $T_{rad}(f)$  provide the probability of  $T_e(\rho)$ . This is the Bayesian inference of  $T_e(\rho)$ , using the observation of  $T_{rad}(f)$ . The estimation of the *posterior* is required for the Bayesian inference of  $T_e(\rho)$ . This is done by allocating a *prior* probability distribution to  $T_e(\rho)$ . The *likelihood* is the conditional probability, which is given by of the prediction of  $T_{rad}(f)$  given that *prior* knowledge on  $T_e(\rho)$  is true. The calculation of *likelihood* requires the prediction of  $T_{rad}(f)$ . Hence, a forward modeling of the Fourier transform spectrometer (FTS) diagnostic is needed to provide the prediction of  $T_{rad}(f)$  and eventually the *likelihood*.

The workflow of the Bayesian inference is shown in a schematic in figure 6.1. The specific example of the inference of  $T_e(\rho)$  is shown from the observation of  $T_{rad}$ . The first step is to assign the *prior* probability distribution to  $T_e(\rho)$  and to select a value from this distribution to initialize the forward calculations. Then, the next step is to determine the *likelihood*. In this case, a forward modeling of the FTS diagnostic is done to predict  $T_{rad}$  via radiation transport calculations using TRAcing VISualized (TRAVIS). The details of the forward model are explained in the next sections. Afterwards, using the *prior* information and the *likelihood*, the maximum a *posteriori* probability (MAP) is determined, which is maximum value of the *posterior* probability. The value of  $T_e(\rho)$  giving MAP is where the  $T_{rad}$  prediction from the forward model fits the observation from the diagnostic. This  $T_e(\rho)$  profile is used as an input to the radiation transport calculation via TRAVIS, which provides the information about the re-absorption, the origin of the emission, and the velocity of electrons responsible for the emission.

The estimation of error bars of these quantities is done by estimating the *posterior*

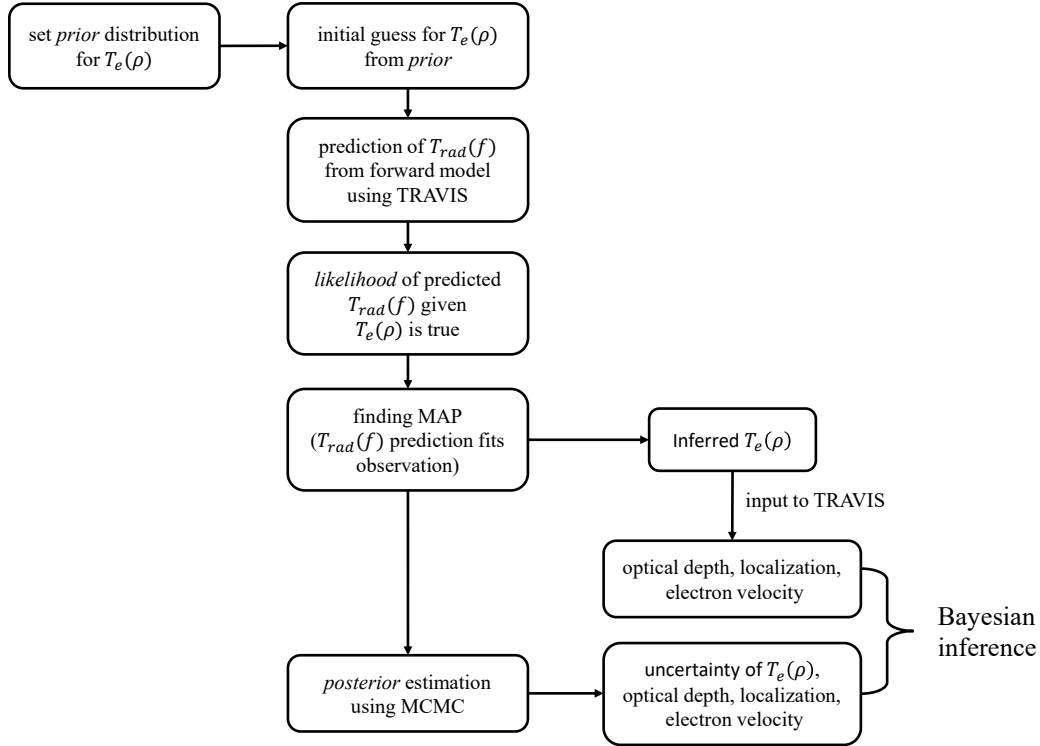


Figure 6.1: Workflow of the Bayesian inference of  $T_e$  using the observation of  $T_{rad}$ .

probability distribution corresponding to a chosen *prior* probability distribution. The main computational effort in determining the *posterior* probability is to analyze the evidence integral (see eq. (6.2)). However, it is possible to extract the shape of the *posterior* probability distribution without evaluating the integral using numerical approximations of the integral. The method used for this work is the Markov chain Monte Carlo (MCMC) which is a class of algorithms used for sampling the probability distribution. Here, MCMC algorithms are used to sample  $T_e(\rho)$  from the multidimensional space of the *prior* probability distributions. These samples are fed to the forward model to calculate the *likelihood*, which provides the corresponding *posterior* probability. The *posterior* probability distribution is not normalized to the evidence probability as the absolute values of *posterior* probabilities are not of interest for this work. The standard deviation of samples from the MCMC algorithms provides the uncertainty on the prediction corresponding to MAP. Finally, the combined information of the MAP and the uncertainty from the *posterior* probability

distribution shape are the Bayesian inference results from the forward modeling of the diagnostic.

The workflow is discussed here only with one free parameter ( $T_e(\rho)$ ) and one experimental observation ( $T_{rad}(f)$ ) for the Bayesian inference. However, for this work, additional free parameters such as  $n_e$ , central magnetic field scaling, variance scaling are used for the forward prediction of  $T_{rad}$ , eventually finding the prediction corresponding to MAP (a prediction that agrees with observation) and uncertainties from the shape of the *posterior* probability distribution. Additionally, the line integrated  $n_e$  observation from the laser interferometer [82] was added as additional observation in the forward model. This has the advantage of restricting the integral of the Bayesian inferred  $n_e(\rho)$  profile. The details of these multiple free parameters and observations are elaborated in the next sections.

## 6.2 Tools for forward modeling

The forward modeling tools, which were used for Bayesian inference during this work, are elaborated in this section. The tools consist of the Bayesian modeling framework Minerva, diagnostic data-source, which provides all diagnostic information such as the geometry and the experimental observations of  $T_{rad}(f)$ , the physics which is used for the prediction of  $T_{rad}(f)$ , and the *prior* probability distribution selection for the free parameters of the model. The forward model predicts  $T_{rad}(f)$  of the ECE by radiation transport calculations done with the TRAVIS code. These radiation transport calculations were already discussed in chapter 3.

### 6.2.1 Bayesian Minerva modeling framework

Forward modeling of the FTS diagnostic is done in the Bayesian Minerva modeling framework [63]. The Minerva framework builds on directed acyclic graphical models. The necessary building blocks for the Bayesian data analysis are described below. These are *prior* probability distribution functions which are required to start the forward calculations, algorithms which can find the position of the MAP and the functionality of MCMC simulations to sample the *posterior* distribution. Different diagnostic data sources are treated as nodes in the graphical models of this frame-

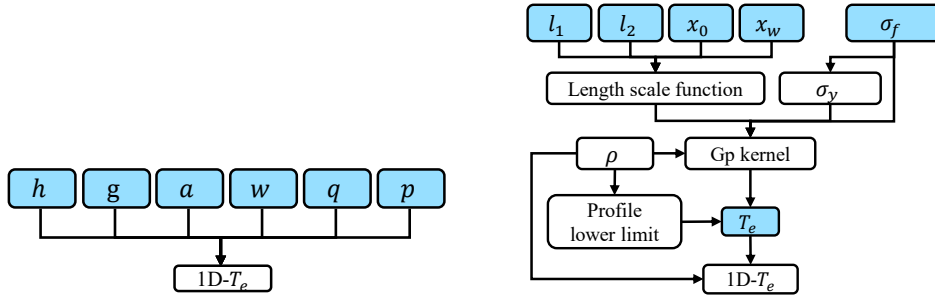
work. This makes it easier to use multiple observations from different diagnostics in the forward model. The modularity and expandability are fundamental advantages of building a forward model in the Bayesian Minerva modeling framework.

### 6.2.2 Diagnostic data-source

The diagnostic data source is an essential part of the forward model because it provides the experimental observations (for example,  $T_{rad}(f)$  from the FTS), which are compared with the predictions for the Bayesian inference of the free parameters. The main reason to use data sources is to keep the model as generic as possible. The FTS data-source provides the raw and analyzed data [47]. The raw data consists of a phase signal between the two arms of the interferometer and a marker signal, which keeps track of the optical path difference created by the moving mirror and the detected interferograms. The analyzed data consists of absolutely calibrated  $T_{rad}(f)$  covering the spectral range of the 2<sup>nd</sup> and 3<sup>rd</sup> harmonic of the ECE and the measurement uncertainties. The  $T_{rad}(f)$  is predicted through radiation transport calculations using TRAVIS in the forward model. The TRAVIS simulations require the information of the ECE diagnostic geometry such as line of sight, wave mode setting, and antenna position. These parameters are also stored in the FTS diagnostic data source. The data source is a node for all the observations and can be directly used in the forward model calculations.

### 6.2.3 Prior for free parameters

The free parameters used for Bayesian inference in this work are as follows:  $T_e$  profile,  $n_e$  profile, extraordinary mode (X-mode) contribution in detected signal, a scaling parameter for central magnetic field strength and the variance scaling of the observational uncertainties. The predicted radiation temperature from the forward model is set to be a combination of X-mode and O-mode emission. This is to take care of any mode mixing effects. However, more weightage is assigned to X-mode, and this weightage is a free parameter in the model and is named as X-mode contribution. A scaling parameter for central magnetic field strength is a free parameter of the model as well, and it is simply the scaling of the central magnetic field given by the magnetic field equilibrium. This scaling of the central magnetic field allows the



(a) Graphical nodes for profiles from parametric prior (b) Graphical nodes for profiles from non-parametric prior

Figure 6.2: (a) Graphical model of the  $T_e(\rho)$  profile from the parametric prior with six free parameters,  $h$ ,  $g$ ,  $a$ ,  $w$ ,  $q$ , and  $p$  having uniform distribution functions (see sec. 6.2.3.1 for definitions of the parameters). (b) Graphical model of the  $T_e(\rho)$  profile from the non-parametric Gaussian process prior with five hyper-parameters  $l_1$ ,  $l_2$ ,  $x_0$ ,  $x_w$ , and  $\sigma_f$  having uniform distribution functions and a number of free parameters equal to the data points chosen in  $\rho$  vector forming the multivariate normal distribution function for  $T_e(\rho)$  profile (see sec. 6.2.3.2).

variation of frequencies of corresponding ECE. If necessary, an observation from a different diagnostic other than the FTS can be included for the Bayesian inference. The forward model of that other diagnostic can easily be incorporated for the combined analysis with the forward model of the FTS. Moreover, additional free parameters have to be considered. For this work, the *prior* distribution function chosen is different for the different free parameters. It is a uniform distribution function for the X-mode contribution factor in the detected signal, for the central magnetic field scaling factor, and for the variance scaling factor. For the  $T_e(\rho)$  and  $n_e(\rho)$  profiles, there are two different kinds of *prior* distribution functions which can be selected. The first is a *prior* based on parameterization of the profile shape, and the second is a *prior* of non-parametric Gaussian processes. These priors are elaborated in the next sections.

### 6.2.3.1 Parametric prior

This *prior* probability distribution is using the  $T_e(\rho)$  and  $n_e(\rho)$  profiles using a certain parameterization. The parameters are as follows:  $a$ , height at the center,  $g$ ,

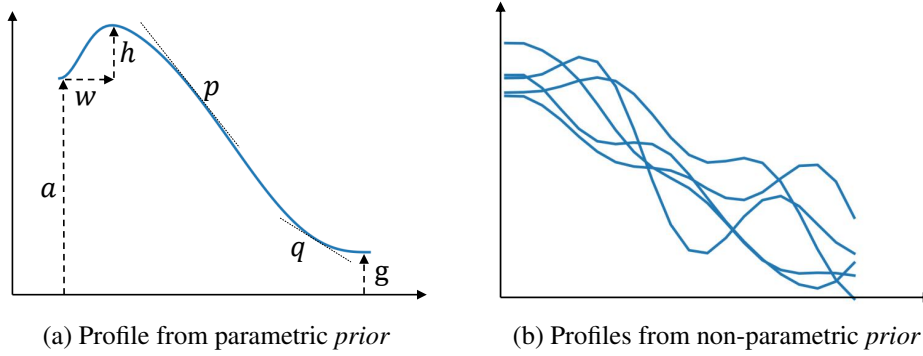


Figure 6.3: (a) Example of profile shape from parameterization (see eq. (6.3)) showing the parameters height at the center,  $a$ , height at the edge,  $g$ , height,  $h$  and width,  $w$ , of the hollowness in profile and two slope parameters,  $p$  and  $q$ . (b) Examples of profile shapes from the non-parametric Gaussian process *prior* distribution.

height at the edge,  $h$ , depth and  $w$ , the width of hollowness at the center of the profile, and two slope parameters,  $p$  and  $q$ . A  $T_e(\rho)$  profile using this parameterization is given by the following equation [30].

$$T_e(\rho) = a(g - h + (1 + h - g)(1 - \rho^p)^q + h(1 - e^{-\rho^2/w^2})) \quad (6.3)$$

This parameterization covers profile gradients and the hollowness of the profile. An example of a profile produced using the parameterization is shown in figure 6.3a. A uniform distribution function is assigned to each of these parameters to construct the *prior* distribution function for the Bayesian inference. A value for each of these parameters from their uniform distribution is used to generate an initial guess for the free parameters ( $T_e(\rho)$  and  $n_e(\rho)$ ) of the model and to start the forward calculation. A graphical representation of  $T_e(\rho)$  profile with these parameters as nodes is shown in figure 6.2a. The only drawback of this *prior* is that the specific parameterization equation cannot generate profile shapes with multiple peaks. Hence, this *prior* limits the available profile shapes for the forward prediction of  $T_{rad}$  and eventually the inference of  $T_e$ . This restriction can be overcome by the use of the non-parametric *priors* which are explained in the next section.

### 6.2.3.2 Non-parametric Gaussian process prior

A Gaussian process *prior* is a multivariate normal distribution of the functions. For a set of arbitrary  $N$  points in the  $\rho$  vector, the Gaussian process is characterized by a mean  $\mu(\rho)$  and a covariance matrix,  $\Sigma_{ij} = k(\rho_i, \rho_j)$ , with  $k$  the kernel function [69]. The multivariate normal distribution,  $\mathcal{N}$ , as a *prior* for the profile is given by the following equation.

$$T_e(\rho) = \mathcal{N}(\mu(\rho), k(\rho, \rho_*)) \quad (6.4)$$

The kernel provides the covariance of different data points in the  $T_e(\rho)$  profile, which controls the smoothness of the functions. For this work, a non-stationary kernel by Paciorek [83] is used to decrease the covariance in the edge of the profile, including sharp edge gradients. The length-scale function of this kernel determines how close the two points,  $\rho$  and  $\rho_*$ , should be to influence each other significantly.

$$l(x) = \frac{l_1 + l_2}{2} - \frac{l_1 - l_2}{2} \tanh\left(\frac{x + x_0}{x_w}\right) \quad (6.5)$$

This length-scale function,  $l(x)$ , is given by the hyper parameters,  $l_1$ , the core saturation value of the correlation length,  $l_2$ , the edge saturation value of the correlation length,  $x_0$ , the point at which the two length scales coalesce,  $x_w$ , the characteristic width of the coalescent region [84].

A uniform distribution function is assigned to each of these parameters to generate the kernel and eventually the profiles for the forward calculations. The graphical representation of the  $T_e(\rho)$  profile with these hyperparameter nodes is shown in figure 6.2b. This *prior* has an advantage to allow profile shapes with multiple peaks as it is a distribution over functions (see fig. 6.3b).

The forward models of the FTS diagnostic constructed with the parametric and non-parametric *priors* are discussed in the next section.

## 6.3 Forward model

The standard approach to construct a forward model structure for Bayesian inference is through the graphical model. A graphical model in the Minerva framework represents the Bayesian network of probabilistic nodes and their connections. A forward model combining the FTS and the line integrated measurement of  $n_e$  is shown in figure 6.4 with the parametric *prior* for the  $T_e(\rho)$  and  $n_e(\rho)$  profiles. Each box in the graphical model represents a node constructed in Minerva modeling framework. These nodes can be the free parameters (blue boxes), the observations (grey ovals), or the model's physics hypothesis (white boxes). The end of an arrow at a node represents the conditional dependence of that node on other nodes. Nodes that are not connected are conditionally independent of each other. The forward models with two plasma profiles *priors* are described in detail in the next sections. The forward prediction results and the Bayesian inference on the free parameters are discussed in the chapter 7.

### 6.3.1 Model with parametric prior

The combined graphical representation of forward model of the FTS and the laser interferometer is shown in figure 6.4 with the parametric *priors* for the plasma profiles. The forward model of the FTS diagnostic for the Bayesian inference of free parameters is constituted of the following nodes. The free parameter nodes in the forward model are the following:  $T_e(\rho)$  and  $n_e(\rho)$  profiles, X-mode contribution,  $M_{xo}$ , central magnetic field scaling factor,  $S_{B_0}$ , and the variance scaling of the observations,  $S_{\sigma^2}$ . The observation node is the  $T_{rad}(f)$  of the ECE measured with the FTS. Additionally, the  $n_e(\rho)$  and  $T_e(\rho)$  profile gradients at the plasma center,  $\nabla T_{e0}$ ,  $\nabla n_{e0}$ , are enforced to be null. The selected parameterization (see eq. 6.3) results in zero profile gradient at the core anyhow. The physics hypothesis of the forward model is contained in the probabilistic nodes of TRAVIS to predict  $T_{rad}(f)$ . For the combined data analysis, the observation of line integrated density  $\int n_e dl$  measured with the laser interferometer can be added for the Bayesian inference of the free parameters. The forward model of the laser interferometer consists of the following nodes. The free parameter nodes are the  $n_e(\rho)$  profile and the variance scaling,  $S'_{\sigma^2}$ . The ob-

Parametric model

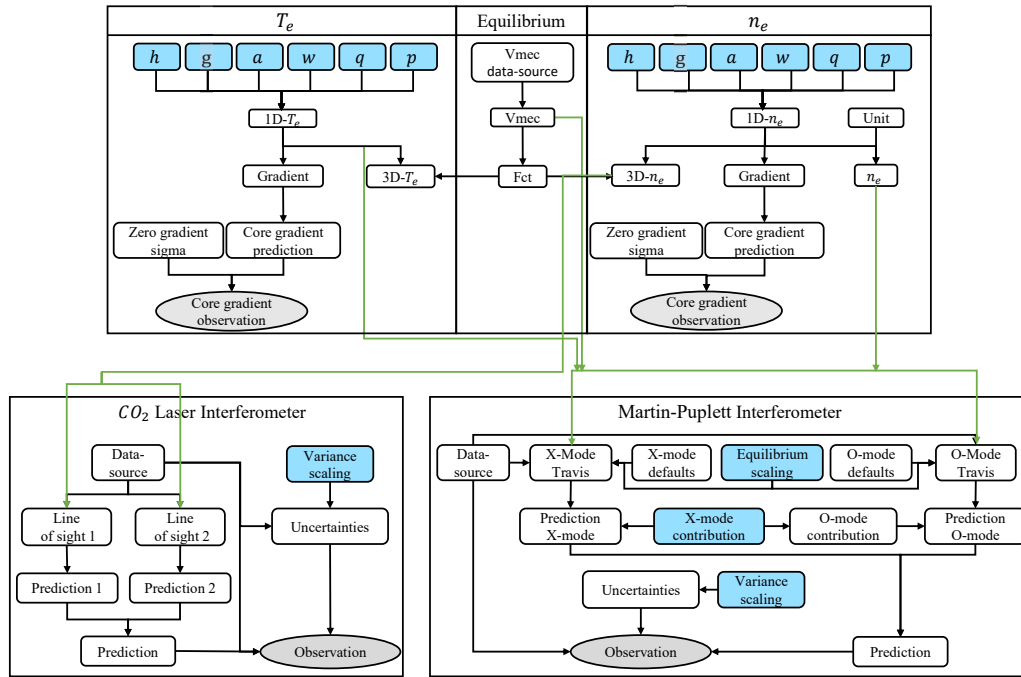


Figure 6.4: A directed acyclic graph of a combined forward model of the FTS and the laser interferometer diagnostic constructed in the Minerva framework with parametric  $priors$  for  $T_e(\rho)$  and  $n_e(\rho)$  profiles. Free parameters of the model are shown in blue and the observations in grey color.

servation node is the line integrated measurement of  $\int n_e dl$ . The physics hypothesis is contained in the line of sight information of the laser interferometer. The addition of this observation to the Bayesian inference from the ECE measurements has the advantage that it restricts the line integral of  $n_e(\rho)$  profile to a level measured by an experiment.

For the Bayesian inference (see the workflow in fig. 6.1), the quantity of interest is the information of the *posterior* probability distribution. The joint *posterior* probability of  $T_e(\rho)$  and  $n_e(\rho)$ ,  $M_{x0}$ ,  $S_{B0}$ , and  $S_{\sigma^2}$  is assumed by the following equation given that the observations of  $T_{rad}(f)$ , the line integrated  $\int n_e dl$  and zero core

plasma gradients are true.

$$\begin{aligned}
 &P(T_e, n_e, M_{x0}, S_{B0}, S_{\sigma^2}, S'_{\sigma^2} | T_{rad}, \int n_e dl, \nabla T_{e0}, \nabla n_{e0}) \propto \\
 &P(T_e, n_e, M_{x0}, S_{B0}, S_{\sigma^2}, S'_{\sigma^2}) \prod_{i=0}^n P(T_{rad_i} | T_e, n_e, M_{x0}, S_{B0}, S_{\sigma^2}, S'_{\sigma^2}, \int n_e dl, \nabla T_{e0}, \nabla n_{e0})
 \end{aligned}
 \tag{6.6}$$

Here,  $n$  is the number of ECE frequencies to be analyzed. For the start of the forward calculations, the initial guess for  $T_e(\rho)$  and  $n_e(\rho)$  are given from the parametric *prior* probability distribution function (see sec. 6.2.3.1). The rest of the free parameters are initialized by a value from their uniform distribution *prior*. The value of free parameters is varied from their *prior* distribution using algorithms in Minerva framework to maximize this *posterior* probability (for finding prediction corresponding to MAP). The resulting observation nodes are multivariate normal distributions,  $X \sim \mathcal{N}(\mu, \sigma^2)$  with the mean,  $\mu$ , of the distribution being equal to the prediction from the forward calculations. The variance contains the scaled uncertainties coming from the experimental observations. The forward prediction results from this model are discussed in the chapter 7.

### 6.3.2 Model with non-parametric prior

The combined graphical representation of the forward model of the FTS and the laser interferometer is shown in figure 6.5 with the non-parametric Gaussian process *priors* for the plasma profiles. The observational nodes for both forward models are the same as discussed in the previous section. However, the free parameter nodes for  $T_e(\rho)$  and  $n_e(\rho)$  profiles are different for the FTS forward model with this *prior*. Here, the Gaussian process *prior* knowledge in the  $T_e(\rho)$  and  $n_e(\rho)$  profiles is used to accommodate profile shapes which are not accessible with the parameterization. The Gaussian processes are governed by the covariance between the data points in the profile, which only restricts the smoothness of the profile shape. Hence, the advantage of this *prior* is that it can generate profile shapes with multiple peaks. The initial guess for the  $T_e(\rho)$  and  $n_e(\rho)$  profiles is a value from the multivariate normal distribution generated from the Gaussian processes.

The number of points chosen for the  $\rho$  vector decides the dimension of the mul-

Non-parametric model

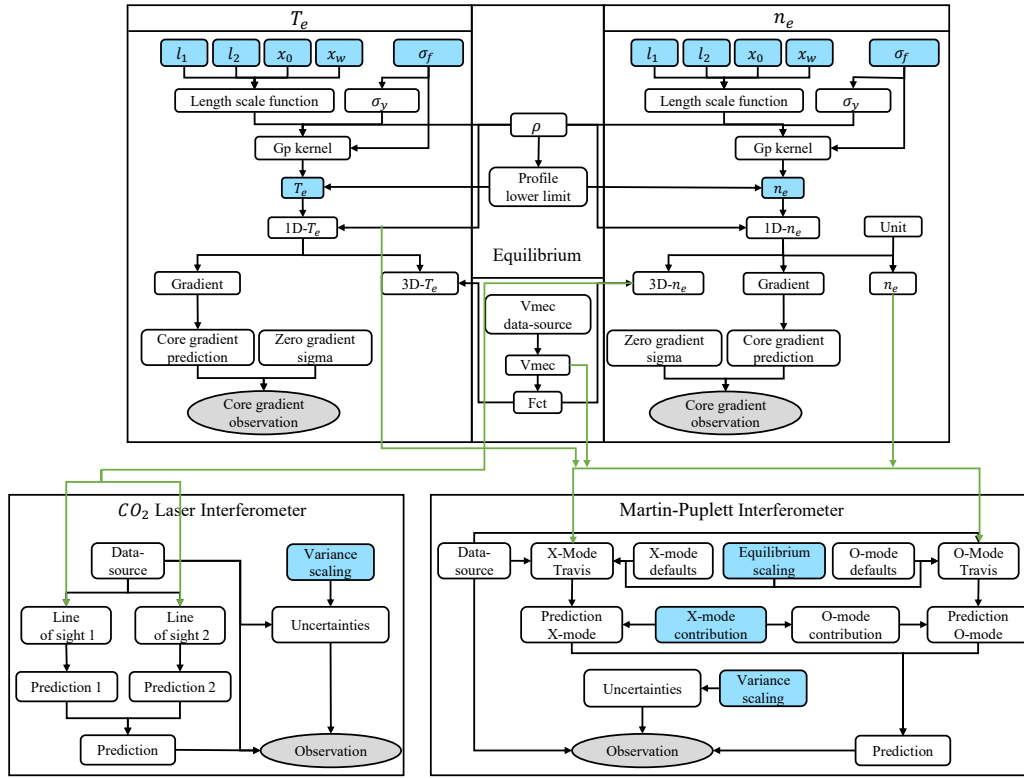


Figure 6.5: A directed acyclic graph of the combined forward model of the FTS and the laser interferometer diagnostic constructed in the Minerva framework with non-parametric Gaussian process *priors* for  $T_e(\rho)$  and  $n_e(\rho)$  profiles. Free parameters of the model are shown in blue and the observations in grey color.

tivariate normal distribution for the  $T_e(\rho)$  and  $n_e(\rho)$  profiles. For this work, a total of 20  $\rho$  points were chosen. The number of total free parameters (23) is higher in this non-parametric Gaussian *prior* forward model compared to the one with the parametric prior (total free parameters 15), which make this model computationally more expensive. The typical duration of the forward model run until the MAP result with parametric *prior* is  $\approx 30$  min and its more than a day for non-parametric Gaussian prior. The joint *posterior* probability for this forward model is also given by the equation (6.6).

The MAP results and the Bayesian inference on the free parameters of these forward models are discussed in detail in the next chapter.



# Chapter 7

## Bayesian inference results

The results discussed in this chapter are from the forward calculations of  $T_{rad}(f)$  using the models discussed in the chapter 6. The workflow shown in figure 6.1 was used to make the Bayesian inference on the free parameters of the models. The free parameters were the  $T_e$  and  $n_e$  profiles, the central magnetic field scaling factor, the extraordinary mode (X-mode) contribution in  $T_{rad}(f)$ , and the variance scaling factor. The  $T_{rad}(f)$  prediction was kept as a combination of X-mode and ordinary mode (O-mode), to take into account the polarization mixing. The uniform distribution *prior* for the X-mode contribution factor had an upper and a lower boundary from 0.8 to 1. The uniform distribution *prior* for the central magnetic field scaling factor had an upper and a lower boundary from 0.97 to 1.03. Both, parametric and non-parametric, *priors* were used for the  $T_e$  and  $n_e$  profiles (see sec. 6.2.3). The free parameters, constituting the parametric and non-parametric *priors*, were also assigned a uniform distribution. For each free parameter, a value from the *prior* distribution was chosen to start the forward calculation. The prediction of  $T_{rad}(f)$ , which agrees with experimental observation, infers these free parameters. Additionally, these inferred  $T_e$  and  $n_e$  profiles were used as an input to the radiation transport calculations, which provided the optical depth, the origin of emission, and the velocities of the electrons responsible for the emission. For the results shown in this chapter, the reflection effects are taken into account by using multiple electron cyclotron emission (ECE) beam passes through the plasma for the radiation transport calculations with TRAcing VISualized (TRAVIS). In addition, the angle

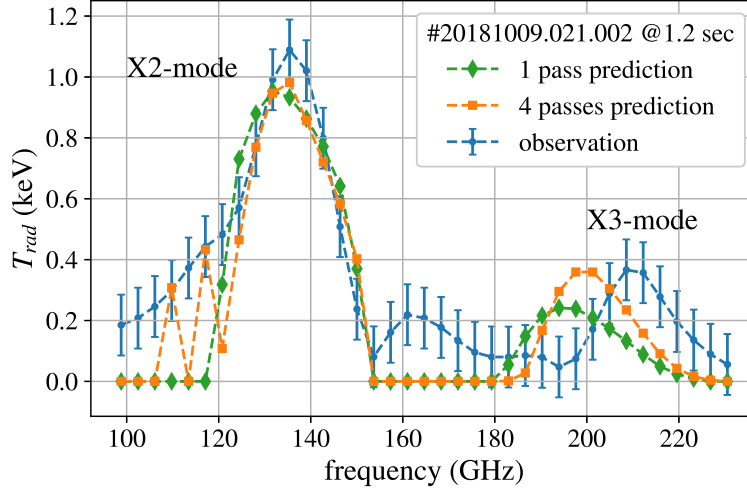


Figure 7.1: The predicted radiation temperature of ECE is shown from the forward calculations using parametric *priors* for the  $T_e$  and  $n_e$  profiles, for different beam passes through plasma.

of the plasma vessel back-wall tile, at the end of ECE sight-line, was varied in the TRAVIS calculation. These reflection effects, in terms of the number of beam passes and back-wall tile angle, cannot be included as a free parameter of the forward model directly. As they are discrete values and the Minerva framework did not allow to have *priors* with discrete distribution functions, and only continuous distribution functions were allowed. Hence, the beam passes through plasma and tile angle were varied manually, and for each combination of these parameters, the forward calculations were repeated to find the best prediction.

In the next sections, the Bayesian inference results are discussed for the ECE measurements from the plasmas with neutral-beam injection (NBI) heating and O2-electron cyclotron resonance heating (ECRH).

## 7.1 Prediction of electron cyclotron emission

This work focuses on the investigation of plasmas with densities beyond second harmonic extraordinary mode (X2-mode) cutoff, and hence the example selected to study the entire broadband ECE spectrum was corresponding to a special scenario

of pure NBI heating avoiding the stray radiation problem. NBI heating startups are not possible at Wendelstein 7-X (W7-X), the plasma was generated with ECRH, and later in discharge, the heating was switched to NBI.

Figure 7.1 shows the prediction of  $T_{rad}$  from the forward calculations using the parametric *priors* for the  $T_e$  and  $n_e$  profiles. As a first approach, the forward calculations were done for a single pass of the ECE beam through the plasma. It can be seen that the prediction of the high field side (HFS) (around 135 – 150 GHz) of the X2 emission agrees well with the experimental observation. However, the low field side (LFS) of the X2 emission, the emission around 155 – 180 GHz and moreover, the X3 emission do not agree with the observed data. Hence, as a next step to understand the spectrum better, the reflection effects inside the plasma vessel were taken into account. The reflection parameters of the beam pass, and plasma vessel back-wall tile angles, in the forward calculations had to be changed manually. The best prediction, including reflections, is shown in the figure.

For 4 passes of ECE beam through plasma, the predicted spectrum showed some features near the LFS of X2 emission (around 110 – 120 GHz), and the X3 emission increased and shifted to HFS frequencies. For multiple reflections, the emission is also collected from the neighboring magnetic field surfaces, and hence only the optically grey X3 emission shifted to other frequencies and not X2. The maximum  $T_{rad}$  of both the X2 and X3 emissions agree well with the experimentally observed data. However, the frequencies of the X2 and X3 emission simultaneously do not agree with the observational frequencies. In the stellarator, the plasma vessel tiles are tilted, and the magnetic field varies toroidally and poloidally. The vessel wall reflections of ECE beam from these tilted vessel tiles result in multiple passes of the radiation through plasma in a zigzag path along with the changing directions. Even though multiple-beam passes were taken into account and the tile angle was varied for radiation transport calculations, the collected emission could be from sight-lines that pass the plasma at different toroidal or poloidal locations, which were not recovered with these calculations. This could be a possible reason behind the non-optimal prediction of full ECE spectrum from the plasma with rather low  $T_e$ .

Additionally, the forward calculations were not able to predict the spectral features around 155 – 180 GHz. This suggests that the physics hypothesis in the for-

ward model was not sufficient for these features. However, the possible explanation of these features could be the relativistically downshifted emission from the hot electrons towards the HFS wall, which was reflected and not sufficiently reabsorbed while passing the plasma. It was observed that no additional information was gained from predictions with non-parametric Gaussian priors.

However, the X2 and X3 emission spectra can also be predicted separately to infer the  $T_e(\rho)$  and  $n_e(\rho)$  profiles. The next section focuses on the quantitative comparison of the inferred profiles from the separate X3 emission predictions for different plasma parameters.

## 7.2 Electron temperature inference

In this section, the Bayesian inferences on  $T_e(\rho)$  are discussed from predictions of three measurements of ECE. The first two measurements are the X2-mode and third harmonic extraordinary mode (X3-mode) emission from the same plasma heated with NBI (same plasma as discussed in figure 7.1). The X2-mode and X3-mode emission were predicted separately. The third measurement is the X3-mode from a plasma heated with O2-ECRH, having different  $T_e$  and  $n_e$  profiles than NBI heated plasma. The Bayesian inference of  $T_e$  profile from the prediction of the X3 emission is the focus of the work. The X2-mode predictions can support this by allowing the comparison of the inferred  $T_e$  profiles from the X2-mode and X3-mode. The results discussed in this section are using the parametric *priors* for the  $T_e$  and  $n_e$  profiles, as the inferred profiles from the parametric and non-parametric *priors* were nearly equal.

Figure 7.2 shows the predictions of  $T_{rad}(f)$  for three measurements (X2 and X3 from NBI and X3 from O2-ECRH), and the corresponding inferred  $T_e$  profiles. Each spectrum (left column of fig.) has three curves: the observation from the Fourier transform spectrometer (FTS), the prediction from the forward calculations (or the maximum a *posteriori* probability (MAP) position), and the spectra corresponding to the MCMC sampling of the *posterior* probability distribution. These samples are referred to as MCMC samples in further discussion. The error bars on the observation of the  $T_{rad}$  spectrum are from the fitting of the calibration factors. The error bars on the prediction of the  $T_{rad}$  spectrum are the standard deviation from the MCMC

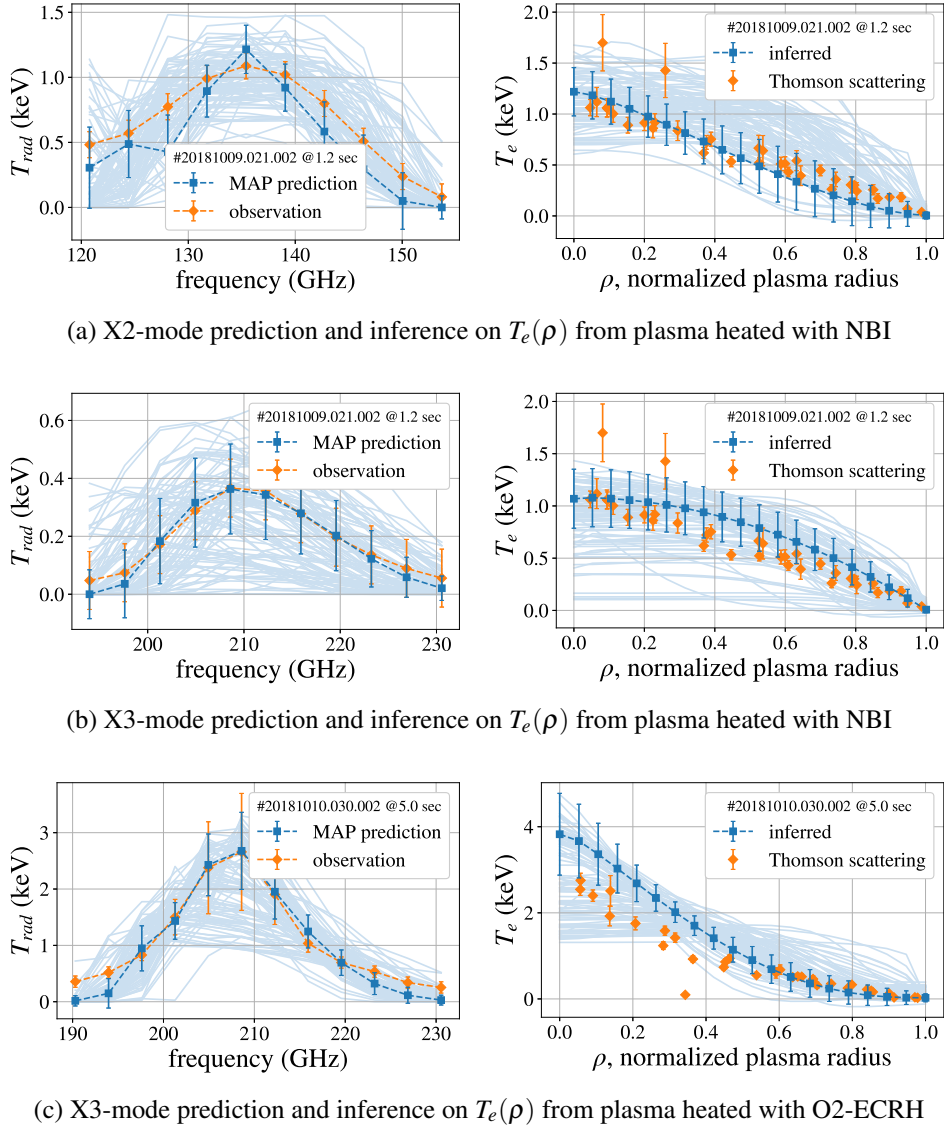


Figure 7.2: The X2-mode and X3-mode predictions from the forward calculations and the corresponding inferred  $T_e(\rho)$  profiles are shown. The multiple lines (light blue) are corresponding to the Markov chain Monte Carlo (MCMC) samples.

samples. The  $T_e$  profiles shown in figure (right column of fig.) have the inferred profile, these are the  $T_e$  values resulting in the shown predicted  $T_{rad}$  spectrum, and  $T_e$  profiles from the MCMC sampling of *posterior*. The Thomson scattering measurement of the  $T_e$  profile is also shown just for reference and was not used in this Bayesian analysis. The error bars on the Thomson scattering measurement are only

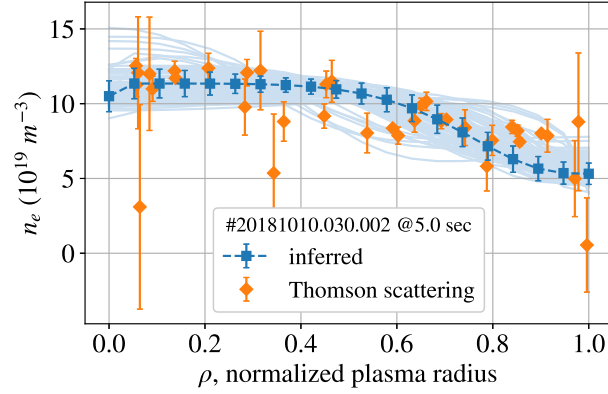


Figure 7.3: The inferred  $n_e(\rho)$  profile is shown from the X3 emission predictions which are discussed in the figure 7.2c. The multiple lines (light blue) are corresponding to the MCMC samples.

statistical. Systematic effects were not taken into account, which means that realistic error bars are maybe higher than shown.

The inferred  $T_e$  profile from the prediction of the X2 emission (see fig. 7.2a) agrees well with the Thomson scattering data. For the same plasma, the inferred  $T_e$  profile (see fig. 7.2b) from the separate prediction of the X3 emission also agrees well with the Thomson scattering data, except few data points near the mid plasma radius,  $\rho = 0.5$ . For O2-ECRH measurements, the inferred  $T_e$  profile (see fig. 7.2c) from predictions of X3 emission also agrees well with the Thomson scattering data near the edge of the plasma at  $\rho \geq 0.5$ . However, near the core of the plasma at  $\rho \leq 0.5$ , the inferred  $T_e$  does not agree and is slightly higher than Thomson scattering data. The plotted error bars on the Thomson scattering data are quite low, but in reality, they are probably higher.

For all three cases, the inferred  $T_e$  profile agrees with the Thomson scattering data up to a certain degree. Additionally, these predictions also infer the  $n_e$  profile, as it was a free parameter in the model, and this is discussed in the next section.

### 7.3 Plasma density inference

In a semitransparent or optically grey plasma, the intensity of the ECE depends on the optical depth, thus, also on the plasma density. Hence, the optically grey

X3 emission measurements also contain information about  $n_e$  profile. The forward calculation of X3 emission, therefore also capable of inferring the information on the  $n_e(\rho)$  hidden in the ECE measurement.

Figure 7.3 shows the inferred  $n_e(\rho)$  profile from the X3-mode predictions shown in figure 7.2c. For these forward calculations, the line integrated plasma density observation always available from the laser interferometer diagnostic was connected to the model. Hence, the line integration of the Bayesian inferred  $n_e(\rho)$  profile stays within the experimentally observed values. At W7-X, the Thomson scattering measurement of the plasma density was almost 10% lower than laser interferometer measurement for reasons which are presently being studied. This was taken care of by using a scaling factor to match the Thomson scattering measurement with the laser Interferometer measurement. The Thomson scattering measurement shown in the figure for  $n_e(\rho)$  profile are these scaled values.

It can be seen in the figure that the inferred  $n_e$  profile from the X3 prediction agrees with the Thomson scattering data. Hence, from the Bayesian analysis of the X3 emission measurements, both inferred  $T_e$  and  $n_e$  profiles agree with the Thomson scattering data up to a certain degree.

The inferred  $T_e$  and  $n_e$  profiles were used as an input to the radiation transport calculations, and that provided the optical depth, the origin of emission, and the velocity of electrons responsible for the emission. These quantities are discussed in the next section.

## 7.4 Optical depth and origin of emission

The inferred  $T_e$  and  $n_e$  profiles from the predictions discussed in the figure 7.2 were used as an input to radiation transport calculations. These calculations provided the following quantities for a better understanding of the measurements. The first quantity is the optical depth of the emission in plasma, which quantifies the re-absorption of the emission, and the second is the velocity of the electrons responsible for the emission. This electron velocity is normalized to the thermal velocity, and the electron velocity closer to the thermal velocity represents the black-body condition at that emission frequency. The numerical upper limit of this normalized velocity is set to 7; similarly, the upper limit of optical depth is  $\approx 10$ . The effective plasma ra-

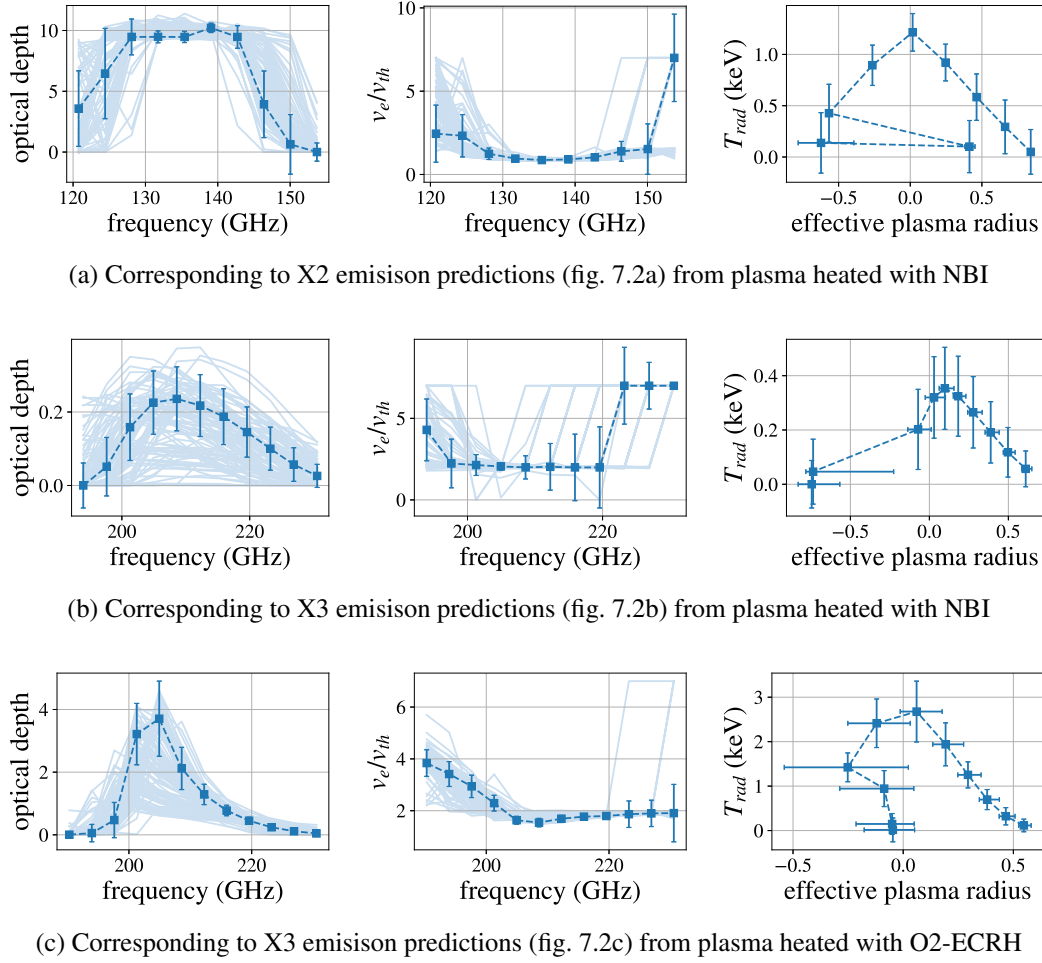


Figure 7.4: The optical depth (note the vertical scale for three cases) of the emission, the velocities of electrons, contributing to the emission, normalized to the thermal velocity ( $v_e/v_{th}$ ) and the radiation temperature mapped to the effective plasma radius, where the center of mass of the finally emitting electrons is located, are calculated with the radiation transport calculations of inferred  $T_e$  profile discussed in figure 7.2. The multiple lines (light blue) are corresponding to the MCMC samples.

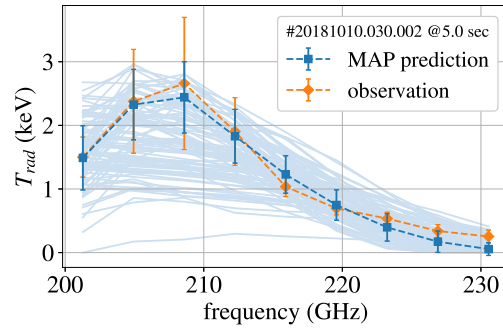
dius was also calculated, and the radiation temperature was mapped to the effective plasma radius, which gave the spatial location or origin of emission in the plasma. The effective plasma radius was calculated for the center of mass of the emission and the location where the emission at a frequency goes to zero on either side of the center of mass location.

The optical depth (left fig. 7.4a) of the X2 emission is high,  $\tau \geq 10$ , in most part of

the spectrum. This is the spectral range that is also used by the radiometer diagnostic to provide  $T_e$  from the optically thick X2 emission (see fig. 5.3). The velocities of the electrons (center fig. 7.4a) are close to the thermal velocities (normalized electron velocity is  $\leq 2$ ). Despite the moderate  $T_e(\rho) \leq 1$  keV in these NBI heated plasmas with high density, the X2 emission remains optically thick. This extends up to the plasma edge at the LFS, and the optical depth decreases only moderately towards the HFS edge. The latter is the effect of the HFS plasma boundary, which cuts the integral of the optical thickness as further out only a purely absorbing edge plasma exists [85]. The effective radius (right fig. 7.4a) is plotted for the center of mass of the emission, and the horizontal error bars on the effective plasma radius represent the width of the emission, while the vertical error bars are from the MCMC samples. The mapping of emission to the effective plasma radius shows that the LFS emission is the downshifted emission from the core electrons, and it is less localized. The HFS emission is localized over the plasma radius.

The X3 emission from the purely NBI heated plasma has an optical depth of  $\leq 0.2$  (left fig. 7.4b), which means that the plasma is transparent for this emission. This is also reflected in the electron velocities (center fig. 7.4b) as they are higher compared to the X2 emission electron velocities and also have higher uncertainties. The mapping of the emission to the effective plasma radius (right fig. 7.4b) shows that the LFS emission is coming from a wider layer of the plasma, while the HFS emission is somewhat localized. This is again because of the plasma boundary, which cuts the integral of the optical thickness.

The X3 emission from the plasma heated with O2-ECRH has slightly higher optical depth  $\approx 3.5$  (left fig. 7.4c) for part of the spectrum. However, most of the frequencies have a low optical depth leading to optically grey plasma. Only for few frequencies (also where the optical depth is higher  $\approx 3.5$ ) the electron velocity is closer to the thermal velocity (normalized electron velocity is  $\leq 2$ ) (center fig. 7.4c). For the X3 emission at these frequencies, the plasma is optically thick. But for the rest of the frequencies, the plasma is optically grey. From the mapping of the emission to effective plasma radius (right fig. 7.4c), the LFS emission is the downshifted emission from core plasma electrons. The horizontal error bars show that the emission is coming from wider plasma layers. The HFS is originating from a narrower plasma layer than LFS, but it is still less localized than X2 emission. The emitting



(a) Prediction of HFS X3 emission

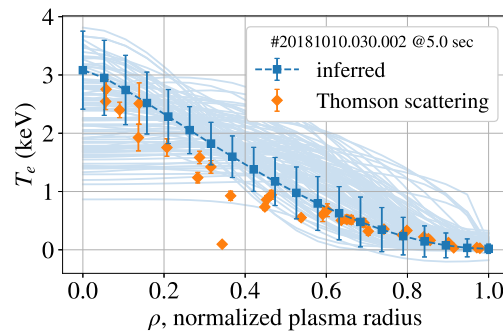
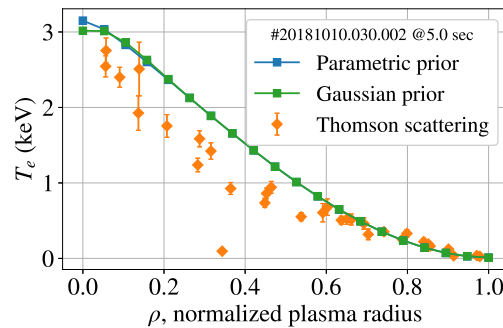

 (b) The inferred  $T_e$  profile

 (c) Comparison of the inferred  $T_e$  profiles from both *priors*

Figure 7.5: (a) The prediction of the HFS X3 emission. (b) Bayesian inferred  $T_e(\rho)$  profile with parametric *priors*. The multiple lines (light blue) are corresponding to the MCMC samples. (c) A comparison of the inferred  $T_e$  profiles, from the prediction of the HFS X3 emission, for parametric and non-parametric Gaussian *priors*.

layer is limited by the cold resonance on the LFS and by the plasma boundary on

the HFS.

The X3 emission, from two different plasmas heated with NBI and O2-ECRH, found to have different optical depth and spatial origin in the plasma. Additionally, as a consequence of plasma boundary, the HFS of the X3 emission was found to be more localized than LFS. These results led to the exploration of the inference on  $T_e$  profile only from the prediction of the HFS X3 emission. These HFS results are discussed in the next section.

## 7.5 Optimized X3 emission frequencies for inference

Figure 7.5 shows the prediction of the HFS X3 emission for measurements from plasma with O2-ECRH. In the previous section, for the full X3 emission prediction, the inferred  $T_e$  profile (see right fig. 7.2c) near the plasma core did not agree well with Thomson scattering data. However, for the prediction of the same X3 emission with only HFS (see fig. 7.5a) already improves the inferred  $T_e$  profile (see fig. 7.5b) with respect to the Thomson scattering data. Additionally, the same HFS X3 emission was also predicted using the non-parametric Gaussian *prior* for the comparison of the inferred  $T_e$  profiles from both *priors*. Figure 7.5c shows the inferred  $T_e$  profile with both *priors* and it can be seen that they are nearly identical. Hence, for the prediction of radiation temperature with the spectral resolution of the FTS, the less computationally expensive parametric *priors* are sufficient.

The Bayesian data analysis results discussed in this chapter showed that the origin of the LFS of optically grey X3 emission is from all over the plasma radius for an electron temperature of  $\leq 2.5$  keV and at higher plasma densities. The HFS of X3 emission is also optically grey, but the emission is more localized as there is no more emission coming from the plasma layer behind HFS, as the plasma boundary ends there. Hence, with HFS the inferred  $T_e$  profile agrees well with Thomson scattering measurement. The optically grey X3 emission, using Bayesian inference, is capable of providing both  $T_e$  and  $n_e$  profiles within model uncertainties. Thus, it makes the X3 emission a suitable candidate for providing the  $T_e$  profiles for higher density plasma beyond X2 emission cutoff.



# Chapter 8

## Conclusions

The third harmonic extraordinary mode (X3-mode) of the electron cyclotron emission (ECE) has been studied theoretically and experimentally for the line of sight and the geometry of the Wendelstein 7-X (W7-X). These studies are first done for a trivial scenario using the radiation transport calculations with the TRAcing VISualized (TRAVIS) code with the flat  $T_e$  and  $n_e$  profile shapes with varying values. This work focuses on higher density applications of ECE beyond the X2 emission cutoff, which for W7-X conditions is at  $\approx 1.2 \times 10^{20} \text{ m}^{-3}$ . Hence, for these radiation transport calculations,  $n_e$  was varied from  $1.1 \times 10^{20} \text{ m}^{-3}$  to  $1.5 \times 10^{20} \text{ m}^{-3}$ , and  $T_e$  was varied from 3 keV to 5 keV. For these higher plasma densities and  $T_e \geq 3 \text{ keV}$ , the X3 emission becomes optically thick with  $\tau \geq 4$ . As a result, the radiation temperature reaches  $T_e$  values.

As a next step, the X3 emission was calculated for different profile shapes of  $T_e$  and  $n_e$ , but with constant value at the core of the plasma. For these high plasma densities, the  $T_e$  values and profile shapes influence the optical depth of the X3 emission more strongly than the  $n_e$  profile shapes and values. It was seen that a peaked  $T_e$  profile leads to a significant decrease of the optical depth of the X3 emission so that the radiation temperature does not reach the core  $T_e(0)$  value. However at W7-X, higher plasma densities are achieved at W7-X with O2-electron cyclotron resonance heating (ECRH) and neutral-beam injection (NBI) heating. For these heating schemes, a broader power deposition is expected, which results in broader  $T_e$  profiles near the core of the plasma. Except for a really peaked  $T_e$  profile, the central

part of the X3 emission has an optical depth of  $\tau \geq 4$ , and the maximum radiation temperature becomes nearly equal to the core  $T_e(0)$  value.

A really peaked  $n_e$  profile also decreases the optical depth of the X3 emission. However, this decrease is insignificant for the studied parameter space because the radiation temperature matches the core  $T_e(0)$  value. Hence in general, the variation of the  $n_e$  profile does not influence the radiation temperature a lot at the central X3 emission frequencies.

The first focus of this work was to investigate the X3 emission with respect to the continuous tracking of the core  $T_e(0)$  value for higher density plasmas. From radiation transport calculations of these plasmas, it is seen that for peaked  $T_e$  profile with low core  $T_e(0) \leq 3$  keV, the radiation temperature of the X3 emission is lower than the core  $T_e(0)$  value. Hence, for the direct application of this optically grey X3 emission as a  $T_e$  diagnostic, a correction factor for the radiation temperature is needed to infer core  $T_e(0)$  values. This correction factor is provided for the relevant plasma densities and electron temperatures of W7-X operation with O2-ECRH and NBI heating. The correction factor is a function of the  $T_e$  and  $n_e$  profiles. For  $n_e(0) \geq 1.2 \times 10^{20} \text{ m}^{-3}$  and for  $T_e(0) \geq 3$  keV, the correction factor remains less than 5% for all  $T_e$  profile shapes except for very peaked profile, for which it is less than 10%. For  $n_e(0) \geq 1.2 \times 10^{20} \text{ m}^{-3}$  and for  $T_e(0) \leq 3$  keV, this correction factor varies between 10 – 40%, depending on the  $T_e$  profile.

To measure the broadband ECE spectrum in the range 100-300 GHz from W7-X plasmas for different heating scenarios, a Martin-Puplett interferometer was used as a Fourier transform spectrometer (FTS). The strong stray radiation from non-absorbed ECRH lies in the middle of  $2^{nd}$  harmonic emission at 140 GHz, and, if not attenuated, it dominates the ECE in the measured spectrum. Generally, at other magnetic confinement devices, because of this stray radiation problem, the interferometer is not used for ECRH plasmas. However, for this work, a multi-mode notch filter was developed, based on a multiple dielectric disk structure with transmission minima at 140 and 234 GHz in the measurement range of the interferometer. The insertion loss of filter is  $\approx 6$  dB, the attenuation depth is  $\approx 20$  dB, and the notch width is  $\approx 10$  GHz. The plasmas with ECRH were successfully scanned by attenuating the stray radiation with this multi-mode notch filter. However, the central X2 emission was also attenuated by the filter, because of the wider notch width ( $\approx 10$  GHz)

centered at 140 GHz. Hence, with the filter inserted, only the X3 emission is available for ECRH plasmas. This drawback of the filter remains a motivation to develop a multi-mode notch filter with a narrower notch width in the future, which would allow measuring both the X2 and X3 emissions in ECRH plasmas.

The interferometer diagnostic, including the notch filter, was absolutely calibrated with a ceramic black-body source using the hot-cold calibration technique. As with the accessible calibration temperatures ( $\leq 600^\circ\text{C}$ ), the intensity of the black-body source did not overcome the high transmission line losses ( $\approx 20$  dB) with an acceptable signal to noise ratio and the interferometer had to be individually calibrated without the transmission line. The calibration of the interferometer combined with frequency-dependent transmission line losses provides the overall diagnostic sensitivity to a temperature change. The assessment of the transmission line losses is a motivation for the next experimental campaign to reduce the losses to improve the calibration of the interferometer.

Plasmas with densities beyond the second harmonic extraordinary mode (X2-mode) cutoff can only be obtained with NBI or O2-ECRH. With these two heating schemes and with the available heating power, the electron temperatures at densities beyond the X2 cutoff were limited to 2.5 keV. Hence, the experimentally available X3 mission is limited with respect to the  $T_e$  values for the plasma densities of interest. With NBI heating, as there is no stray radiation, both X2-mode and X3-mode are observed with the FTS. The maximum electron temperature available with NBI heating is however as low as 1.2 keV. It was observed that for densities above  $1.2 \times 10^{20} \text{ m}^{-3}$ , the X2-mode emission goes into cutoff as expected and the X3-mode emission continues to increase with density even if  $T_e$  remains constant. This suggests that the re-absorption of the X3 emission is still increasing. The radiation temperature remains lower than the electron temperature (1.2 keV), which means that the X3 emission is optically grey for these plasma parameters. This was also expected from the radiation transport calculations of the X3 emission.

As the X2 emission is observed by both ECE diagnostics, the FTS and the radiometer, observations from both were compared for similar plasma parameters. The central and the high field side (HFS) emission from both diagnostics is in good agreement, which validates the calibration. However, the low field side (LFS) emission disagrees. A possible reason could be the poor calibration of the FTS at lower

frequencies.

At a higher electron temperature of 2 keV and a plasma density of  $1 \times 10^{20} \text{ m}^{-3}$ , the optically thick X3 emission could be reached in W7-X so far only with O2-ECRH. These experimental results support the radiation transport calculation results for the W7-X geometry.

At Most frequencies, the X3 emission is optically grey; hence, a classical direct inversion of the experimentally measured radiation temperature to electron temperature is a nontrivial exercise. Hence, a more advanced Bayesian data analysis approach through the forward modeling of the FTS diagnostic is adopted to interpret the experimentally measured ECE spectra. The key input parameter to the forward model, which is of interest, is the  $T_e$  profile. The *prior* knowledge for the  $T_e$  profile in the model is given by profile parameterization or Gaussian processes. It turns out that the forward prediction of the full extraordinary mode (X-mode) spectrum (100 – 300 GHz) does not fit the experimental observation for both *priors* of  $T_e$ . After including the reflection effects at the vessel wall, by increasing the beam passes through the plasma in the forward calculation, the prediction of the full X-mode spectrum improves. However, the spectral features (around 155 – 180 GHz) between the X2 and X3 emission are not predicted even after including the multiple beams passes. This suggests that the physics hypothesis in the forward model lacks some aspects to predict these features. However, as the focus of this particular work is the X3 emission, and it is predicted separately for the better understanding of the emission, and the inference of the underlying  $T_e$  profile has been conducted with this frequency range only. The reflection effects for these predictions are included by a variety of beam passes through the plasma and the vessel's back-wall tile angle.

For this work, the two available X3 emission spectra observations from high-density plasmas were investigated with this forward modeling separately. Even, the prediction of the X3 emission spectrum for NBI heating with low  $T_e \approx 1.2 \text{ keV}$  generates a  $T_e$  profile, which fits the Thomson scattering measurements well. The radiation transport calculations at inferred  $T_e$  profile show that the optical depth is low  $\leq 0.2$  and the origin of the emission at LFS is from all over the plasma radius, while HFS is more localized. The reason for it is not the increased optical depth but rather the end of the plasma boundary, which adds a geometrical aspect of localization.

With O2-ECRH at somewhat higher  $T_e \approx 2.5$  keV, the prediction of the X3 emission spectrum produces a  $T_e$  profile, which is slightly higher than the Thomson scattering data near the core of plasma. At the edge, it fits well. A possible reason for this disagreement of two profiles could be unaccounted systematic errors of the Thomson scattering measurement. Another reason could be that the  $T_e$  profile is peaked near the core of the plasma. Radiation transports studies show that for these peaked profiles, the radiation temperature is lower than the electron temperature. This means that the inferred  $T_e$  values are overestimated to keep the radiation temperature lower than the electron temperature. The radiation transport calculations at the inferred  $T_e$  profile show that only a few central frequencies the optical depth is above 3. Hence, the emission is optically thick for these frequencies, while the majority of emission is optically grey. The origin of the emission at the LFS is the downshifted emission from the hot core electrons, and the HFS emission is again more localized because of the end of plasma boundary.

An optically grey emission depends on both electron temperature and plasma density. The prediction of optically grey X3 emission also generates a  $n_e$  profile, which agrees well with the Thomson scattering data. Hence, with Bayesian analysis, both  $T_e$  and  $n_e$  profiles were generated from predictions of the X3 emission measurements.

For direct diagnostic applicability as a  $T_e$  measurement for plasma control purposes with  $T_e \geq 2.5$  keV, as seen from the experiments, the radiation temperature of the central X3 emission can be taken as electron temperature. For lower  $T_e \leq 2.5$  keV, a correction factor for radiation temperature of the X3 emission is provided to derive  $T_e$ . Moreover, this work has shown that the X3 emission observations, irrespective of the optical depth, can provide information on the  $T_e$  profiles using Bayesian data analysis.



# Acknowledgments

This work has been carried out within the framework of the EUROfusion consortium and has received funding from the Euratom research and training programme 2014-2018 and 2019-2020 under grant agreement No 633053. The views and opinions expressed herein do not necessarily reflect those of the European Commission.

I would like to thank Prof. Dr. Robert C. Wolf for the opportunity to pursue my Ph.D. at Max-Planck-Institute for Plasma Physics, Greifswald. During this Ph.D. project, his fruitful physics discussions and constructive feedback, enhanced my knowledge on the topic and the methodology of research in general. His supervision was key to execute the experimental part of the project within the narrow time frame of the W7-X operations. Moreover, his quick approach, towards discussions of technical difficulties and analysis, led to timely progress of the project.

I would like to express my gratitude to Dr. Matthias Hirsch for discussing, even the tiny details of the project for both experiments and analysis, which were extremely insightful. Under his supervision, I enhanced the knowledge on how to tackle a research problem. Additionally, I would also like to thank him for offering chocolate croissants now and then, that kept me motivated during the Ph.D. project.

I would also like to thank Dr. Johan W. Oosterbeek for all his help during the commissioning of the diagnostic, and his insights in dealing with microwave components. His supervision enhanced my knowledge on the experimental techniques, and specially on how to approach the technical difficulties during the experiments.

I am grateful to Dr. Nikolai B. Marushchenko for his physics discussions, and the help with the TRAVIS simulations. I would like to mention Dr. Udo hoefel for his help with TRAVIS and Minerva framework. Also, I am grateful to Mathias Stern and Karsten Ewert, for their help in setting up the diagnostic.

Last but not least, I would like to thank my family for their understanding towards

my scientific aspirations far away from home. I appreciate their patience specially during the pandemic, and I would like to acknowledge their enormous motivation and support.

# Statutory declaration

I hereby declare in accordance with the examination regulations that I myself have written this document, that no other sources as those indicated were used and all direct and indirect citations are properly designated, that the document handed in was neither fully nor partly subject to another examination procedure or published and that the content of the electronic exemplar is identical to the printing copy.

Greifswald, 31 May 2021

\_\_\_\_\_  
Neha Chaudhary



# List of Figures

1.1	Wendelstein 7-X stellarator . . . . .	3
1.2	Schematic of increasing magnetic field and corresponding ECE . . .	5
1.3	Frequencies of ECE harmonics for different aspect ratio of devices .	7
2.1	Ray passing through plasma to show optical depth integral . . . . .	15
3.1	Theoretical broadband ECE spectra from X-and O-mode . . . . .	19
3.2	Theoretical ECE spectra showing X2-mode cutoff . . . . .	20
3.3	Radiation temperature of X3 emission for flat plasma profiles . . . .	22
3.4	Optical depth of X3 emission for flat plasma profiles . . . . .	23
3.5	X3 emission for varying $T_e$ profiles . . . . .	25
3.6	X3 emission for varying $n_e$ profiles . . . . .	27
3.7	Correction factor for X3 emission $T_{rad}$ to reach $T_e$ . . . . .	29
4.1	Schematic of entire FTS diagnostic setup at W7-X . . . . .	32
4.2	Magnetic field along ECE line of sight . . . . .	33
4.3	Notch filter transmission . . . . .	37
4.4	Schematic of the Martin-Puplett interferometer . . . . .	38
4.5	Workflow of the interferogram signal processing . . . . .	39
4.6	Moving mirror signals from interferometer . . . . .	40
4.7	Transmission line losses . . . . .	43
4.8	Interferogram from black-body emission . . . . .	44
4.9	Black-body spectra at two temperatures for calibration . . . . .	46
4.10	Calibration factors for interferometer . . . . .	47
5.1	Experimental broadband ECE spectra . . . . .	50

5.2	Experimental spectra showing X2-mode cutoff . . . . .	52
5.3	Comparison of radiometer and interferometer observations . . . . .	54
5.4	X2 and X3 emission evolution with increasing plasma density . . . . .	55
5.5	X3 emission $T_{rad}$ comparison with $T_e$ . . . . .	56
6.1	Workflow of the Bayesian data analysis . . . . .	60
6.2	Graphical nodes for parametric and non-parametric priors . . . . .	63
6.3	Example profiles from parametric and non-parametric priors . . . . .	64
6.4	Forward model using parametric prior . . . . .	67
6.5	Forward model using non-parametric prior . . . . .	69
7.1	Prediction of broadband ECE spectrum . . . . .	72
7.2	Predicted ECE and the inferred $T_e$ . . . . .	75
7.3	The inferred $n_e$ from X3 emission . . . . .	76
7.4	Optical depth and spatial origin of the X3 emission . . . . .	78
7.5	The inferred $T_e$ profile from prediction of HFS X3 emission . . . . .	80

# Publications as first author

This chapter contains the peer-reviewed publication in a bibliography format, which are published during my Ph.D as a first author.

## Peer-reviewed articles

- [1] Neha Chaudhary et al. “Investigation of optically grey electron cyclotron harmonics in Wendelstein 7-X”. In: *EPJ Web of Conferences*. Vol. 203. EDP Sciences. 2019, p. 03005. This publication introduces the Michelson interferometer as an electron cyclotron emission (ECE) diagnostic, and it shows the theoretical studies and results of the multi-mode stray radiation notch filter design based on the dielectric disk structure. It also describes the experimental setup which was used to test the multi-mode stray radiation filter, and the experimental results were then compared to the theoretical calculations. The notch-filter described in the publication was finally used in the plasma experiments to scan broadband ECE for this Ph.D. work. I have written the entire text of the publication, and performed the theoretical studies of the multi-mode notch filter for optimization of the design of the filter for its application as stray radiation filter. I am also responsible for the experimental setup and results which are shown in this publication. J. Oosterbeek contributed with selection of the final filter design, and the understanding of the experimental and theoretical results. All the coauthors have contributed with their constructive feedback and insightful discussion for the better understanding of the stray radiation notch filter results shown in this publication.
- [2] N Chaudhary et al. “Investigation of higher harmonics of electron cyclo-

tron emission using Fourier transform spectroscopy in Wendelstein 7-X". In: *Journal of Instrumentation* 15.09 (2020), P09024. This publication describes the measurement process of broadband ECE with Martin-Puplett interferometer at Wendelstein 7-X (W7-X) in details. This publication provides the interferometer diagnostic description, and the absolute calibration results of the diagnostic. Analysis of measured data in details to extract the ECE spectrum from the measured interferograms was also discussed in the publication. It also shows the first experimental results from interferometer for the broadband ECE spectrum. In the publication, the X3 emission from experiments was shown, and it agrees with electron temperature from Thomson scattering data at higher plasma densities beyond X2 emission cutoff. I have written the full text of the publication, and responsible for the diagnostic setup, calibration of the diagnostic, experiments to measure ECE, and the analysis of the measured data and the shown experimental results. J. Oosterbeek contributed with the experimental setup and conducting calibration of the diagnostic. M. Hirsch contributed with the experiments and the understanding of the experimental results. All the coauthors have contributed with their constructive feedback and insightful discussion for the better understanding of the experimental technique and results shown in this publication.

# Publications as coauthor

In this chapter, the peer reviewed articles are listed in the bibliography format, which are published during my Ph.D. work as a coauthor.

## Peer-reviewed articles

- [1] JW Oosterbeek et al. “Michelson Interferometer design in ECW heated plasmas and initial results”. In: *Fusion Engineering and Design* 146 (2019), pp. 959–962. This publication describes the Michelson interferometer design and initial results from the experiments. The publication describes the stray radiation at the interferometer location, and the notch filter to attenuate this stray radiation. The publication also shows the experimental electron cyclotron emission (ECE) spectra for the neutral-beam injection (NBI) without filter, and O2-electron cyclotron resonance heating (ECRH) with filter, showing successful attenuation of the stray radiation. I contributed by development of the stray radiation notch filter, setup of the Michelson interferometer, experiments and analysis of the spectrum shown in this publication.
- [2] Johan W Oosterbeek et al. “Assessment of ECH stray radiation levels at the W7-X Michelson Interferometer and Profile Reflectometer”. In: *EPJ Web of Conferences*. Vol. 203. EDP Sciences. 2019, p. 03010. This publication estimates the stray radiation levels at the location of Michelson interferometer and the profile reflectometer at Wendelstein 7-X (W7-X). I have contributed with experimental setup and the commissioning of experiments for stray radiation levels at Michelson interferometer location.

- [3] Matthias Hirsch et al. “ECE Diagnostic for the initial Operation of Wendelstein 7-X”. In: *EPJ Web of Conferences*. Vol. 203. EDP Sciences. 2019, p. 03007. This publication describes the ECE results from the initial operation of the W7-X. One part of this publication outlines the ECE diagnostic for high density steady state operation at W7-X. This publication also describes the solution of stray radiation problem for broadband measurement of ECE using Michelson interferometer for ECRH, by a developed multi-mode notch filter. I contributed with the development of the multi-mode notch filter, and with the setup of the ECE diagnostic for high density operation as discussed in this publication.

# Acronyms

**AOI** angle of incidence.

**ASDEX** Axially Symmetric Divertor Experiment.

**D-T** Deuterium-Tritium.

**ECE** electron cyclotron emission.

**ECRH** electron cyclotron resonance heating.

**FFT** fast Fourier transform.

**FTS** Fourier transform spectrometer.

**HFS** high field side.

**InSb** Indium antimonide.

**ITER** International Thermonuclear Experimental Reactor.

**JET** Joint European Torus.

**LFS** low field side.

**MAP** maximum a *posteriori* probability.

**MCMC** Markov chain Monte Carlo.

**MHD** magnetohydrodynamic.

**NBI** neutral-beam injection.

**O-mode** ordinary mode.

**O-X-B** Ordinary-eXtraordinary-Bernstein.

**O1-mode** first harmonic ordinary mode.

**O2-mode** second harmonic ordinary mode.

**PTFE** polytetrafluoroethylene.

**TRAVIS** TRAcing VISualized.

**VMEC** Variational Moments Equilibrium Code.

**W7-X** Wendelstein 7-X.

**X-mode** extraordinary mode.

**X2-mode** second harmonic extraordinary mode.

**X3-mode** third harmonic extraordinary mode.

**X4-mode** fourth harmonic extraordinary mode.

# Bibliography

- [1] LM Kovrizhnykh. “The energy confinement time in stellarators”. In: *Nuclear fusion* 24.4 (1984), p. 435.
- [2] JD Lawson. “Some criteria for a useful thermonuclear reactor”. In: *Atomic Energy Research Establishment* (1955).
- [3] AE Costley. “On the fusion triple product and fusion power gain of tokamak pilot plants and reactors”. In: *Nuclear Fusion* 56.6 (2016), p. 066003.
- [4] John Wesson and David J Campbell. *Tokamaks*. Vol. 149. Oxford university press, 2011.
- [5] S Sudo et al. “Scalings of energy confinement and density limit in stellarator/heliotron devices”. In: *Nuclear Fusion* 30.1 (1990), p. 11.
- [6] Francis F Chen et al. *Introduction to plasma physics and controlled fusion*. Vol. 1. Springer, 1984.
- [7] Lyman Spitzer Jr. “The stellarator concept”. In: *The Physics of Fluids* 1.4 (1958), pp. 253–264.
- [8] LA Artsimovich. “Tokamak devices”. In: *Nuclear Fusion* 12.2 (1972), p. 215.
- [9] Per Helander. “Theory of plasma confinement in non-axisymmetric magnetic fields”. In: *Reports on Progress in Physics* 77.8 (2014), p. 087001.
- [10] T Klinger et al. “Overview of first Wendelstein 7-X high-performance operation”. In: *Nuclear Fusion* 59.11 (2019), p. 112004.
- [11] RC Wolf et al. “Major results from the first plasma campaign of the Wendelstein 7-X stellarator”. In: *Nuclear Fusion* 57.10 (2017), p. 102020.

- 
- [12] J Nührenberg et al. “Overview on Wendelstein 7-X theory”. In: *Fusion Technology* 27.3T (1995), pp. 71–78.
- [13] Andreas Dinklage et al. “Magnetic configuration effects on the Wendelstein 7-X stellarator”. In: *Nature Physics* 14.8 (2018), pp. 855–860.
- [14] H-S Bosch et al. “Technical challenges in the construction of the steady-state stellarator Wendelstein 7-X”. In: *Nuclear Fusion* 53.12 (2013), p. 126001.
- [15] Thomas Sunn Pedersen et al. “First results from divertor operation in Wendelstein 7-X”. In: *Plasma Physics and Controlled Fusion* 61.1 (2018), p. 014035.
- [16] RC Wolf et al. “Electron-cyclotron-resonance heating in Wendelstein 7-X: A versatile heating and current-drive method and a tool for in-depth physics studies”. In: *Plasma Physics and Controlled Fusion* 61.1 (2018), p. 014037.
- [17] J Geiger et al. “Aspects of steady-state operation of the Wendelstein 7-X stellarator”. In: *Plasma Physics and Controlled Fusion* 55.1 (2012), p. 014006.
- [18] P McNeely et al. “Commissioning and initial operation of the W7-X neutral beam injection heating system”. In: *Fusion Engineering and Design* 161 (2020), p. 111997.
- [19] Samuel A Lazerson et al. “Validation of the BEAMS3D neutral beam deposition model on Wendelstein 7-X”. In: *Nuclear Fusion* 60.7 (2020), p. 076020.
- [20] Ian H Hutchinson. “Principles of plasma diagnostics”. In: *Plasma Physics and Controlled Fusion* 44.12 (2002), p. 2603.
- [21] Hans-Jürgen Hartfuß and Thomas Geist. *Fusion Plasma Diagnostics with Mm Waves*. Wiley Online Library, 2013.
- [22] AE Costley. “50 Years of Electron Cyclotron Emission Research”. In: *Fusion Science and Technology* 55.1 (2009), pp. 1–15.
- [23] PC De Vries et al. “Electron cyclotron emission measurements by means of a grating polychromator on the large helical device”. In: *Fusion engineering and design* 53.1-4 (2001), pp. 185–191.
- [24] AE Costley et al. “Electron cyclotron emission from a tokamak plasma: experiment and theory”. In: *Physical Review Letters* 33.13 (1974), p. 758.

- [25] HJ Hartfuss et al. “Diagnostic strategy of the W7-X stellarator”. In: *Review of scientific instruments* 68.2 (1997), pp. 1244–1249.
- [26] HJ Hartfuss, T Geist and M Hirsch. “Heterodyne methods in millimetre wave plasma diagnostics with applications to ECE, interferometry and reflectometry”. In: *Plasma Physics and Controlled Fusion* 39.11 (1997), p. 1693.
- [27] Matthias Hirsch et al. “ECE Diagnostic for the initial Operation of Wendelstein 7-X”. In: *EPJ Web of Conferences*. Vol. 203. EDP Sciences. 2019, p. 03007.
- [28] M Hirsch et al. “ECE diagnostic and-measurements during the first W7-X divertor campaign”. In: *46th EPS Conference on Plasma Physics*. European Physical Society. 2019.
- [29] Udo Hoefel et al. “Bayesian modeling of microwave radiometer calibration on the example of the Wendelstein 7-X electron cyclotron emission diagnostic”. In: *Review of Scientific Instruments* 90.4 (2019), p. 043502.
- [30] NB Marushchenko, Yu Turkin and H Maassberg. “Ray-tracing code TRAVIS for ECR heating, EC current drive and ECE diagnostic”. In: *Computer Physics Communications* 185.1 (2014), pp. 165–176.
- [31] S Schmuck et al. “Design of the ECE diagnostic at Wendelstein 7-X”. In: *Fusion engineering and design* 84.7-11 (2009), pp. 1739–1743.
- [32] S Schmuck et al. “Electron cyclotron emission spectra in X-and O-mode polarisation at JET: Martin-Puplett interferometer, absolute calibration, revised uncertainties, inboard/outboard temperature profile, and wall properties”. In: *Review of Scientific Instruments* 87.9 (2016), p. 093506.
- [33] H Yamada et al. “Characterization of energy confinement in net-current free plasmas using the extended International Stellarator Database”. In: *Nuclear Fusion* 45.12 (2005), p. 1684.
- [34] Andreas Dinklage et al. “Physical model assessment of the energy confinement time scaling in stellarators”. In: *Nuclear fusion* 47.9 (2007), p. 1265.

- 
- [35] AB Kukushkin, PV Minashin and AR Polevoi. “Limit of electron cyclotron radiation in ITER long pulse operation”. In: *Proc. 38th EPS Conference on Plasma Physics, Strasbourg, France G*. Vol. 35. 2011, P4.
- [36] D Zhang et al. “First Observation of a Stable Highly Dissipative Divertor Plasma Regime on the Wendelstein 7-X Stellarator”. In: *Physical review letters* 123.2 (2019), p. 025002.
- [37] RC Wolf et al. “Performance of Wendelstein 7-X stellarator plasmas during the first divertor operation phase”. In: *Physics of Plasmas* 26.8 (2019), p. 082504.
- [38] RC Wolf et al. “Wendelstein 7-X program—Demonstration of a stellarator option for fusion energy”. In: *IEEE Transactions on plasma science* 44.9 (2016), pp. 1466–1471.
- [39] Martin Greenwald et al. “A new look at density limits in tokamaks”. In: *Nuclear Fusion* 28.12 (1988), p. 2199.
- [40] PC De Vries et al. “Survey of disruption causes at JET”. In: *Nuclear fusion* 51.5 (2011), p. 053018.
- [41] Per Helander et al. “Stellarator and tokamak plasmas: a comparison”. In: *Plasma Physics and Controlled Fusion* 54.12 (2012), p. 124009.
- [42] Torsten Stange et al. “Advanced electron cyclotron heating and current drive experiments on the stellarator Wendelstein 7-X”. In: *EPJ Web of Conferences*. Vol. 157. EDP Sciences. 2017, p. 02008.
- [43] HP Laqua, ECRH Group et al. “Electron Bernstein wave heating and emission via the OXB process at W7-AS”. In: *Plasma physics and controlled fusion* 41.3A (1999), A273.
- [44] Nikolai B Marushchenko et al. “Reduced field Scenario with X3 heating in W7-X”. In: *EPJ Web of Conferences*. Vol. 203. EDP Sciences. 2019, p. 01006.
- [45] C Nührenberg. “Free-boundary ideal MHD stability of W7-X divertor equilibria”. In: *Nuclear Fusion* 56.7 (2016), p. 076010.

- [46] JW Oosterbeek et al. “Michelson Interferometer design in ECW heated plasmas and initial results”. In: *Fusion Engineering and Design* 146 (2019), pp. 959–962.
- [47] N Chaudhary et al. “Investigation of higher harmonics of electron cyclotron emission using Fourier transform spectroscopy in Wendelstein 7-X”. In: *Journal of Instrumentation* 15.09 (2020), P09024.
- [48] N Chaudhary et al. “Investigation of higher harmonics of Electron Cyclotron Emission in the W7-X stellarator”. In: *46th EPS Conference on Plasma Physics*. 2019.
- [49] NA Salmon and A Eberhagen. “First electron cyclotron emission and electron temperature profile measurements on ASDEX Upgrade”. In: *Europhysics Conference Abstracts*. Vol. 16. Part II. 1992, pp. II–1107.
- [50] M Keilhacker, ASDEX Team et al. “The ASDEX divertor tokamak”. In: *Nuclear fusion* 25.9 (1985), p. 1045.
- [51] ME Austin et al. “Improved operation of the Michelson interferometer electron cyclotron emission diagnostic on DIII-D”. In: *Review of scientific instruments* 68.1 (1997), pp. 480–483.
- [52] A Simonetto et al. “A fast multichannel Martin-Puplett interferometer for electron cyclotron emission measurements on JET”. In: *Review of Scientific Instruments* 82.11 (2011), p. 113506.
- [53] FJ Stauffer et al. “TFTR Michelson interferometer electron cyclotron emission diagnostic”. In: *Review of Scientific Instruments* 56.5 (1985), pp. 925–927.
- [54] Stefan Schmuck et al. “Electron cyclotron emission measurements on JET: Michelson interferometer, new absolute calibration, and determination of electron temperature”. In: *Review of Scientific Instruments* 83.12 (2012), p. 125101.
- [55] G Taylor et al. “Status of the design of the ITER ECE diagnostic”. In: *EPJ Web of Conferences*. Vol. 87. EDP Sciences. 2015, p. 03002.
- [56] G Taylor et al. “Update on the status of the ITER ECE diagnostic design”. In: *EPJ Web of Conferences*. Vol. 147. EDP Sciences. 2017, p. 02003.

- 
- [57] Johan W Oosterbeek et al. “Assessment of ECH stray radiation levels at the W7-X Michelson Interferometer and Profile Reflectometer”. In: *EPJ Web of Conferences*. Vol. 203. EDP Sciences. 2019, p. 03010.
- [58] Neha Chaudhary et al. “Investigation of optically grey electron cyclotron harmonics in Wendelstein 7-X”. In: *EPJ Web of Conferences*. Vol. 203. EDP Sciences. 2019, p. 03005.
- [59] S Schmuck et al. “Electron temperature and density inferred from JET ECE diagnostics”. In: *Proceeding of the 41st EPS conference on plasma physics, Berlin. P*. Vol. 1. 2014, p. 025.
- [60] SK Rathgeber et al. “Estimation of edge electron temperature profiles via forward modelling of the electron cyclotron radiation transport at ASDEX Upgrade”. In: *Plasma Physics and Controlled Fusion* 55.2 (2012), p. 025004.
- [61] Udo Höfel. “Bayesian analysis of electron cyclotron emission measurements at Wendelstein 7-X”. Doctoral Thesis. Berlin: Technische Universität Berlin, 2020. DOI: 10.14279/depositonce-9621. URL: <http://dx.doi.org/10.14279/depositonce-9621>.
- [62] Severin S Denk et al. “Radiation transport modelling for the interpretation of oblique ECE measurements”. In: *EPJ web of conferences*. Vol. 147. EDP Sciences. 2017, p. 02002.
- [63] J Svensson and A Werner. “Large scale Bayesian data analysis for nuclear fusion experiments”. In: *2007 IEEE International Symposium on Intelligent Signal Processing*. IEEE. 2007, pp. 1–6.
- [64] Michael I Jordan et al. “Graphical models”. In: *Statistical science* 19.1 (2004), pp. 140–155.
- [65] Zoubin Ghahramani. “Probabilistic machine learning and artificial intelligence”. In: *Nature* 521.7553 (2015), pp. 452–459.
- [66] Thomas Bayes. “LII. An essay towards solving a problem in the doctrine of chances. By the late Rev. Mr. Bayes, FRS communicated by Mr. Price, in a letter to John Canton, AMFR S”. In: *Philosophical transactions of the Royal Society of London* 53 (1763), pp. 370–418.

- [67] Andrew Gelman et al. *Bayesian data analysis*. CRC press, 2013.
- [68] Charles J Geyer. “Practical markov chain monte carlo”. In: *Statistical science* (1992), pp. 473–483.
- [69] David JC MacKay. “Introduction to Gaussian processes”. In: *NATO ASI Series F Computer and Systems Sciences* 168 (1998), pp. 133–166.
- [70] George Befki. “Radiation processes in plasmas”. In: *rpp* (1966).
- [71] E Mazzucato. “Propagation of a Gaussian beam in a nonhomogeneous plasma”. In: *Physics of Fluids B: Plasma Physics* 1.9 (1989), pp. 1855–1859.
- [72] Steven P Hirshman and JC Whitson. “Steepest-descent moment method for three-dimensional magnetohydrodynamic equilibria”. In: *The Physics of fluids* 26.12 (1983), pp. 3553–3568.
- [73] L Young and EG Cristal. “Low-pass and high-pass filters consisting of multilayer dielectric stacks”. In: *IEEE Transactions on Microwave Theory and Techniques* 14.2 (1966), pp. 75–80.
- [74] S Orfanidis. *Electromagnetic waves and antennas; sophocles j*. 2004.
- [75] Augustin Fresnel. *Extrait d'un" Mémoire sur la loi des modifications imprimées à la lumière polarisée par sa réflexion totale dans l'intérieur des corps transparents", par MA Fresnel*. 1823.
- [76] James W Lamb. “Miscellaneous data on materials for millimetre and submillimetre optics”. In: *International Journal of Infrared and Millimeter Waves* 17.12 (1996), pp. 1997–2034.
- [77] Kenneth J Button. *Infrared and Millimeter Waves V3: Submillimeter Techniques*. Elsevier, 1980.
- [78] DH Martin, E Puplett and DH Martin. *Infrared Phys.* 1969.
- [79] Hans J Liebe. “An updated model for millimeter wave propagation in moist air”. In: *Radio Science* 20.5 (1985), pp. 1069–1089.
- [80] SA Bozhenkov et al. “The Thomson scattering diagnostic at Wendelstein 7-X and its performance in the first operation phase”. In: *Journal of Instrumentation* 12.10 (2017), P10004.

- [81] E Pasch et al. “The Thomson scattering system at Wendelstein 7-X”. In: *Review of Scientific Instruments* 87.11 (2016), 11E729.
- [82] KJ Brunner et al. “Real-time dispersion interferometry for density feedback in fusion devices”. In: *Journal of Instrumentation* 13.09 (2018), P09002.
- [83] Christopher J Paciorek and Mark J Schervish. “Nonstationary covariance functions for Gaussian process regression”. In: *Advances in neural information processing systems*. 2004, pp. 273–280.
- [84] MA Chilenski et al. “Improved profile fitting and quantification of uncertainty in experimental measurements of impurity transport coefficients using Gaussian process regression”. In: *Nuclear Fusion* 55.2 (2015), p. 023012.
- [85] NB Marushchenko et al. “Optimization of ECE Diagnostics for the W7-X Stellarator”. In: *Fusion science and technology* 50.3 (2006), pp. 395–402.